Physics implications of shape on biological function
Pomp, W.

Citation
Pomp, W. (2017, December 5). *Physics implications of shape on biological function*. *Casimir PhD Series*. Retrieved from https://hdl.handle.net/1887/57789

Cover Page

Universiteit Leiden

Physics Implications of Shape on Biological Function

PROEFSCHRIFT

ter verkrijging van
de graad van Doctor aan de Universiteit Leiden,
op gezag van Rector Magnificus prof. mr. C. J. J. M. Stolker,
volgens besluit van het College voor Promoties
te verdedigen op dinsdag 5 december 2017
klokke 12:30 uur

door

Wim Pomp

geboren te Rotterdam
in 1988

Promotor: Prof. dr. T. Schmidt
Co-promotor: Dr. L. Giomi

Promotiecommissie: Prof. dr. G. J. Schütz (TU Wien, Wenen, Oostenrijk)
                   Prof. dr. C. Storm (TU Eindhoven)
                   Prof. dr. A. M. Dogterom
                   Prof. dr. E. R. Eliel
                   Prof. dr. H. Schiessel

"If a man never contradicts himself, the reason must be that he virtually never says anything at all."
Erwin Schrödinger

Contents

CONTENTS

Chapter 1

Introduction

This thesis looks at the shape of biological systems. By using a physics description and exploiting mathematics, I was able to make qualitative and quantitative deductions about the studied systems. The thesis includes research into dendritic spines, membrane properties under phase separation, and the influence of an anisotropic cytoskeleton on the shape of cells. All these topics deal in some way or another with a description of the shape of the biological system in question.

1.1 About shape and biology

Shape is a property of almost everything. In our urbanized western world it is often the rectangle, or its three-dimensional counterpart, the cuboid, which is most prevalent. However, already long before the advent of modern technology, biological systems are using all kinds of shapes to their advantage. The diversity in biological function is enormous, and since function and shape are linked inseparably, the variety in shapes in biology is overwhelming. In biology, shapes might not be as regular or recurring as the common usage of the word 'shape' reflects. Instead, biological structures often could be considered 'formless' or 'unshapely'. However, almost universally, shape and function are tightly bound together. Examples are everywhere around us; with the human body itself providing a multitude of different shapes, from very small to body-sized scales. DNA, for example, is a long string of information [1], that, because of its shape, is accessible to proteins [2]. Microvilli in the colon boost their surface area for maximal contact with nutrients by forming folds [3]. And on a bigger scale, we find a beautiful example in the eye. It is crucial for perfect vision for the lens in the eye to be lens-shaped [4]. Moreover, muscles in the eye can deform the lens to change its focal length, a feat that engineers have only been able to replicate in the form of liquid lenses in recent years. Change of shape is a very common thing in biology, not only the eye lens can do this, but also other parts. For example, certain cells can squeeze their nucleus to be able to navigate through very narrow passages [5]. On the other end, the change of shape in the hands of primates is pivotal for the ability to grab things. In this thesis, we will look at a few examples in biology where shape and function meet. We start in chapter 2, where we will look at the shape of parts of neurons, and how a two-dimensional manifold in three-dimensional space influences diffusion of receptors in a dendritic spine.

1.2 Biology

1.2.1 Synapse

The dendritic spine, mentioned above, is part of the neuronal synapse, the connection between two neuronal cells [6, 7]. Of those neuronal cells, there are almost one hundred billion in a human brain [8]. If we look at the shape of neurons (figure 1.1) we see that they are unlike any other cell type [9]. Neurons consist of a cell body called soma, in which normal cellular processes like in many other cells happen. The soma contains, for example, the nucleus, the

location of the genetic information, and the mitochondria, the power plants of the cell. Extending from the soma is a tubular shaped part which can be up to one meter in length, which is millions of times larger than the size of the soma. The end of the axon is branched and ends in axon terminals [10]. Also extending from the soma are a multitude of dendrites [6]. The soma, axon, and dendrites all have different functions, which is reflected in their respective shapes, but also in their internal organization [11]. For instance, inside the axon, and inside the dendrites, different cargos are transported by various molecular motors [12]. Some motors only operate in the axon, others only in the dendrites.
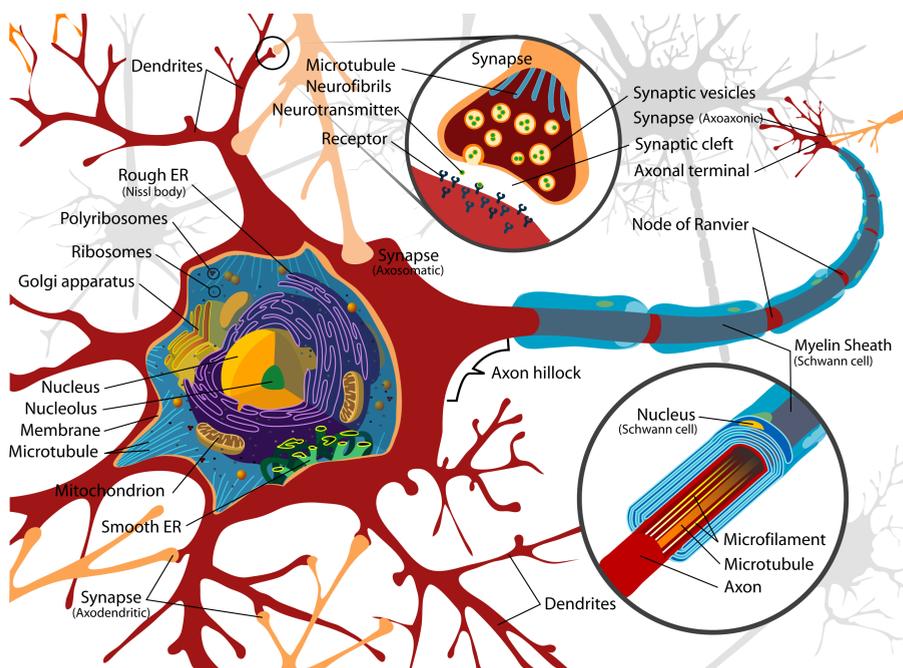
Figure 1.1: **Neuron cell** (red), showing the inside of the soma with the nucleurs, endoplasmatic reticulum (purple) and mitochondria (yellow). Dendrites branch out to meet with other neurons' axons. One axon, up to about a meter long and convered with a myelin sheath, connects to other neurons' dendrites. By LadyofHats - Own work. Public Domain, `https://commons.wikimedia.org/w/index.php?curid=3970826`

Actually, the axon and dendrites are both involved in a neuron's main task: transporting signals. The main difference between the axon and the dendrites is that the former sends signals to other neurons, whereas the latter receives signals from other neuron cells. The ends of the axon, the axon terminals, may connect anywhere on a dendrite of another cell. Rarely, they even connect to the soma of a neuron [13]. At the site of connection, the receiving neuron forms a protrusion, called 'dendritic spine' [7]. It is these dendritic spines, whose shape I discuss in chapter 2.

It is these connections from one neuron to another (or sometimes to the same neuron) via axons and dendrites, that are called synapses. The human brain has about $1.5 \cdot 10^{14}$ of them [14]. In neurons, a signal travels as a voltage difference across the membrane [15], generated by the timely opening of ion channels and aided by special cells making up a myelin sheath around the axon [16]. This configuration allows the development of a traveling wave of electrical potential that reaches an axon terminal. On arrival of the electric pulse, the axon terminal releases neurotransmitters in the space between the axon terminal and the connecting dendritic spine, the synaptic cleft [17]. This space is usually enclosed by glial cells, which prevent the escape of and recycle neurotransmitters. Neurotransmitters released in the synaptic cleft are subsequently sensed by specialized receptors in the membrane of the receiving dendritic spine [18]. When sufficient receptors are activated, ion channels open and a new electric wave is generated traveling down the dendrite of the receiving neuron.

1.2.2 Membrane

While looking at the shape of cells, what we are actually looking at is the membrane and how it is folded in space. But the membrane is not just a sheet of material. In order to perform its function, it is deformable, filled with proteins and can have local chemical, mechanical, and electrical properties. The main material constituting the membrane are lipids. The distinct hydrophobic and hydrophilic parts of lipids make them organize in such a way that their hydrophobic tails are shielded from water [19]. This results in structures like micelles, vesicles and cell membrane. It is hard for a lipid to escape from micelles and the membranes of vesicles and cells. However, it can freely move within them [20]. Therefore, a cell membrane is often regarded as a two-dimensional fluid [21]. In most cells about half of the membrane surface area is covered with proteins protruding half or fully through the membrane. Proteins interact with each other and with other molecules on both sides of the membrane.

Proteins also interact with the membrane itself, some bend the membrane [22, 23], others sense curvature [24]. Some proteins have a preference for a specific type of lipid. It is because of this structuring ability that the term 'lipid rafts' was coined [25, 26], the existence of which however is still a heavily discussed topic [27].

Lipids in lipid bilayers, because of their molecular shape, can be in any of the different phases assumed by a lipid membrane. Naturally, there is a liquid-like and a solid-like phase, usually called the liquid-disordered and gel phase, respectively. When cholesterol is present in the membrane, a third phase is possible in which the lipids are ordered like in the gel phase, but are mobile like in the liquid-disordered phase. Therefore, this phase is called liquid-ordered [28]. These different phases can coexist in the same membrane, where patches of different phases exist within an ocean of another phase. These patches may contain specific proteins, and as a whole, patches are mobile in the membrane, like a raft, which is why they are called lipid rafts. I looked at the behavior of membranes that undergo unmixing and start formation of patches, and report on my results in chapter 3.

1.2.3 Cytoskeleton

An important class of proteins that regulates the shape of a cell are the proteins of the cytoskeleton. The main players are actin and tubulin [29]. Tubulin forms long, stiff strands called microtubules [30, 31]. Actin, besides forming long, rather flexible strands, forms a fine network [32]. Besides their function as a structural skeleton, actin and microtubules are also used as tracks for motors to transport cargo within the cell [33]. For instance, they sort the chromosomes during cell division [34–36]. Some motors from the myosin family (mainly myosin II) are also used to align actin fibers, sliding them with respect to each other. This is the primary action of muscles in which actin fibers are pulled along long myosin fibers [37, 38].

Some cells have a number of thick bundles of actin fibers containing myosin. These contractile fibers can provide the force needed to move a cell or to change its shape [39]. In chapter 4 we will see how stress fibers make the cytoskeleton anisotropic and how this influences the shape of the cell. Formation of stress fibers is regulated by the Ras-homolog gene, family member A (RhoA). It activates Rho-associated coiled-coil forming kinase (ROCK). ROCK subsequently activates myosin and deactivates cofilin, which normally breaks down actin filaments [40]. In chapter 5 we will see how inhibition of ROCK changes the shape of cells.

1.3   Microscopy

1.3.1   Super resolution

Ever since Antoni van Leeuwenhoek started using the first microscopes in the 17th century [41], we have been able to see smaller and smaller objects. Van Leeuwenhoek himself made a number of novel observations, among which is the discovery of gametes. However, it became clear that there is a fundamental limit to the resolving power of microscopes. In the 19th century this was formalized by Ernst Abbe who derived an equation describing the minimal distance d between two objects that still can be distinguished from each other [42]:

$$d = \frac{\lambda}{2n\sin\theta} \tag{1.1}$$

The minimum distance, d, depends on the wavelength of light λ, which is between 400 and 780 nm for visible light. Furthermore, it depends on the index of refraction n of the lens and the opening angle θ from which light is collected by the lens. The latter is usually summarized in the numerical aperture (NA) [43]:

$$NA = n\sin\theta \tag{1.2}$$

Modern objectives can reach an NA of almost 1.5, making it possible to identify structures at a length scale d less than 200 nm when using visible light. Still, most proteins and other biological structures' sizes are on the order of a few nanometers. Since about half a century ago we can resolve these structures anyhow, by using electrons [44] instead of light. However, using electron microscopy, it is impossible to use fluorescent molecules to label specific parts of the cell. Furthermore, due to the destructive nature of the high-energy electrons, the observed cell dies very quickly when put in an electron microscope [45].

Fluorescent molecules, fluorophores, are used since half a century to label and visualize large structures in cells [46–48]. Co-expression of a fluorescent molecule, together with a protein of interest, ensures that we are able to see relatively large structures like microtubules, or the actin cytoskeleton [49]. However, because of the diffraction limit described above, smaller structures are invisible. In the 1990's, a new methodology was developed to break the optical diffraction limit. By making the concentration of fluorophores so small that individual molecules could be observed, the center positions of all visible molecules was determined with a precision much better than the Abbe limit [50–53]. In terms of distance d (equation (1.1)), the resolution of a microscope

becomes σ which is approximately [54]:

$$\sigma \propto \frac{d}{\sqrt{N}} \tag{1.3}$$

Here N is the number of detected photons. Since most fluorophores emit a few thousand photons before bleaching, the accuracy was improved to less than 10 nm in this way [55]. It was the work of Moerner, Betzig, Hell (awarded with the Nobel prize in chemistry in 2014) and others which made it possible to resolve large structures using a high concentration of fluorophores, while still being able to determine the center position of the fluorophore with high precision [50, 52, 53]. Nowadays, a common method to do this involves fluorophores which are stochastically turned on for only a short time [56]. In this way a small number of fluorophores is visible at any time, making it possible to determine the location of each one at high accuracy.

Another application of single-molecule fluorescence microscopy, used since longer ago, is to accurately track the position of single molecules. In this way, it is possible to distinguish single-molecule properties from the bulk behaviour [20, 57]. We used this method in chapter 2 to track individual quantum dots. Furthermore, in chapter 3 we used a similar method to track the position of an artificial membrane.

1.3.2 Confocal microscopy

To image a sample with a microscope, an area of interest in a sample needs to be placed in the focus of the microscope. In the resulting image, the molecules in focus appear sharp. However, in traditional microscopy, the light of molecules which are not in focus still travels through the microscope and onto the sensor that is used to make the image. This light appears in the image as a blur and lowers the signal-to-noise ratio of the molecules in focus.

The confocal microscope has a pinhole that filters out any out-of-focus light, thereby increasing the sharpness and signal-to-noise ratio in the microscope image [58]. Unfortunately, also some in-focus light is filtered out and therefore confocal microscopes require more light than traditional microscopes. Additionally, because of the position of the pinhole, not all of the sample can be imaged at the same time. One solution to this problem is to image the sample point-by-point and reconstruct an image afterwards. Naturally, this sequential

method is slow. Another method uses a large number (≈ 1000) of pinholes on a spinning disk, which scans the whole sample in very short time [59]. This allows for a normal camera to be used and decreases the needed time significantly. It is this method which is used to obtain the high-speed images of mobile samples in chapters 4 and 5.

1.4   Outline of this thesis

In **chapter 2** I look at the shape of dendritic spines, the 'receiving' end of synapses which is the connection between two neuronal cells in our brain. As described earlier, when a signal arrives at the axon terminal, neurotransmitters are released into the synaptic cleft, the space between the axon terminal and the dendritic spine. These neurotransmitters are sensed by receptors which are located in the membrane of the dendritic spine. The number of receptors determines the strength of signal transduction in the synapse. Thus it regulates memory and learning.

I made an artificial system mimicking the mushroom-shape of a dendritic spine, and added lipid-anchored quantum dots as a mimetic to the receptors. By changing the shape of this artificial system, and tracking the quantum dots, I was able to underline the importance of the shape of the dendritic spine on receptor escape and ultimately memory. I show that the escape rate scales faster than quadratic with the radius of the head of the system. Furthermore, I recovered the predicted quadratic dependence on the length of the tube which connects the dendritic spine head with the dendrite. My experiments showed that a large dendritic spine head contributes to long-term memory. On the other hand, both a small dendritic spine head and a short connection from head to dendrite contribute to learning.

In **chapter 3**, I show the influence of local differences in membrane constituents on membrane mechanics. The plasma membrane of a cell consists of a vast mixture of different lipids. Lipids can be in a number of different states of matter. Lipids in the same state tend to aggregate. This process, called phase separation, causes the membrane not to be a homogeneous mix of lipids. Instead, it has different properties at different locations. I induced phase separation in vesicles using light. This process involves a carefully prepared sample of giant unilamellar vesicles (GUVs). The composition of these GUVs is chosen such that only a small number of lipids needs to be converted to cross a composition threshold into a region where the lipids will unmix. I used a mixture of phosphocholine, sphingomyelin, and cholesterol. A small number of the phosphocholines had a rhodamine fluorescent molecule attached to their

headgroup. When this fluorophore was excited, highly reactive singlet-oxygen was created. In turn, singlet-oxygen reacted with nearby lipids in such a way that the lipid was transformed into a species characterized by an increased melting temperature. In this way, the composition changed on illumination such that the lipids unmixed by light control.

During these experiments, I discovered that the membrane changed significantly during this process. The membrane tension dropped, and more surface area became available. This affects the shape of the membrane at small scale and therefore had an effect on, for example, the binding affinity of curvature sensing proteins.

Chapter 4 deals with the shape of cells that exhibit an anisotropic cytoskeleton. Usually, the actin microfilaments are distributed more or less isotropically. However, in a number of cells, such as fibroblasts and epithelial cells, strongly aligned stress fibers span big parts of the cell. This alignment results in a highly anisotropic actin cytoskeleton.

Cells on a flat substrate usually adhere in a finite number of discrete locations near the edge of the cell. The actin cytoskeleton pulling on the membrane, the pressure inside and outside the cell, and the traction forces between cell and substrate are in a force balance. This balance dictates that the shape of the cell edge which could be faithfully described as a part of an ellipse. By expanding a Young-Laplace like description, I showed that not only are the cell edges parts of ellipses but also that they are all part of the same ellipse. Furthermore, I investigated how the aspect ratio of this ellipse results directly from the anisotropy of the actin cytoskeleton of the cell. The size of the ellipse, together with the size of the traction forces between cell and substrate, was an excellent predictor for the contractility of the actin cytoskeleton. I showed that in fibroblastoid and epithelioid cells, the anisotropic contractility is about twice as large as the isotropic contractility.

I continued this study in **chapter 5**. In the experiments described, I actively influenced the shape of the cells by adding different amounts of ROCK inhibitor. ROCK Influences the activity of myosin motors and the generation of stress fibers, so the contractility of the cytoskeleton was changed. Because the effect was strongest in anisotropic stress fibers, the anisotropy of the shape of the cell decreased gradually with increased concentration of ROCK inhibitor. This was reflected in the shape factor describing the shape of the edges of the cell, which increases; edges became circular. It is also visible in the ratio between anisotropic and isotropic stresses, which decreased, indicating a decrease in contractility originating from the aligned stress fibers.

In this thesis, I investigated various biological systems. I applied general physics laws to describe my observations and to extract the essentials of what I observed. All the protein pathways, which undisputedly are essential for the regulation of cellular function, were completely neglected. Rather, the systems I studied, I tried to simplify as much as possible, always keeping in mind that a real biological system is always more complicated. But, by sufficiently simplifying these systems, I could find simple descriptions, which describe the general behavior of the systems in which I was interested. In this way, by utilizing mathematical descriptions, I was able to make qualitative and quantitative conclusions about these biological systems.

References

[1] J. D. Watson and F. H. C. Crick. "Molecular structure of nucleic acids: A structure for Deoxyribose Nucleic Acid". In: *Nature* 171.4356 (1953), pp. 737–738. DOI: `10.1038/171737a0`.

[2] C. A. Bewley, A. M. Gronenborn, and G. M. Clore. "Minor groove-binding architectural proteins: Structure, function, and DNA recognition". In: *Annu. Rev. Biophys. Biomol. Struct.* 27.1 (1998), pp. 105–131. DOI: `10.1146/annurev.biophys.27.1.105`.

[3] T. M. Mukherjee and A. W. Williams. "A comparative study of the ultrastructure of microvilli in the epithelium of small and large intestine of mice". In: *J. Cell Biol.* 34.2 (1967), pp. 447–461. DOI: `10.1083/jcb.34.2.447`.

[4] H. Bloemendal et al. "Ageing and vision: structure, stability and function of lens crystallins". In: *Prog. Biophys. Mol. Biol.* 86.3 (2004), pp. 407–485. DOI: `10.1016/j.pbiomolbio.2003.11.012`.

[5] A. Jayo et al. "Fascin regulates nuclear movement and deformation in migrating cells". In: *Dev. Cell* 38.4 (2016), pp. 371–383. DOI: `10.1016/j.devcel.2016.07.021`.

[6] S. Ramon y Cajal. "Estructura de los centros nerviosos de las aves". In: *Rev. Trim. Histol. Norm. Pat.* 1 (1888), pp. 1–10.

[7] J. N. Bourne and K. M. Harris. "Balancing structure and function at hippocampal dendritic spines". In: *Annu. Rev. Neurosci.* 31.1 (2008), pp. 47–67. DOI: `10.1146/annurev.neuro.31.060407.125646`.

[8] F. A. Azevedo et al. "Equal numbers of neuronal and nonneuronal cells make the human brain an isometrically scaled-up primate brain". In: *J. Comp. Neurol.* 513.5 (2009), pp. 532–541. DOI: 10.1002/cne.21974.

[9] K. M. Harris and S. B. Kater. "Dendritic spines: Cellular specializations imparting both stability and flexibility to synaptic function". In: *Annu. Rev. Neurosci.* 17.1 (1994), pp. 341–371. DOI: 10.1146/annurev.ne.17.030194.002013.

[10] D. Debanne et al. "Axon physiology". In: *Physiol. Rev.* 91.2 (2011), pp. 555–602. DOI: 10.1152/physrev.00048.2009.

[11] H. Hering and M. Sheng. "Dendritic spine: structure, dynamics and regulation". In: *Nat. Rev. Neurosci.* 2.12 (2001), pp. 880–888. DOI: 10.1038/35104061.

[12] N. Hirokawa and R. Takemura. "Molecular motors and mechanisms of directional transport in neurons". In: *Nat. Rev. Neurosci.* 6.3 (2005), pp. 201–214. DOI: 10.1038/nrn1624.

[13] R. G. Santander et al. "Communicating synapses: Types and functional interpretation". In: *Cells Tissues Organs* 142.3 (1991), pp. 249–260. DOI: 10.1159/000147198.

[14] B. Pakkenberg et al. "Aging and the human neocortex". In: *Exp. Gerontol.* 38.1-2 (2003), pp. 95–99. DOI: 10.1016/S0531-5565(02)00151-1.

[15] A. L. Hodgkin and A. F. Huxley. "A quantitative description of membrane current and its application to conduction and excitation in nerve". In: *Bull. Math. Biol.* 52.1-2 (1990), pp. 25–71. DOI: 10.1007/BF02459568.

[16] R. Virchow. "Über das ausgebreitete Vorkommen einer dem Nervenmark analogen Substanz in den thierischen Geweben". In: *Arch. für Pathol. Anat. und Physiol. und für Klin. Med.* 6.4 (1854), pp. 562–572. DOI: 10.1007/BF02116709.

[17] E. R. Kandel. "The molecular biology of memory storage: A dialogue between genes and synapses". In: *Science* 294.5544 (2001), pp. 1030–1038. DOI: 10.1126/science.1067020.

[18] H. Wolosker et al. "D-amino acids in the brain: D-serine in neurotransmission and neurodegeneration". In: *FEBS J.* 275.14 (2008), pp. 3514–3526. DOI: 10.1111/j.1742-4658.2008.06515.x.

[19] Ü. Coskun and K. Simons. "Cell membranes: The lipid perspective". In: *Structure* 19.11 (2011), pp. 1543–1548. DOI: 10.1016/j.str.2011.10.010.

[20] T. Schmidt et al. "Imaging of single molecule diffusion". In: *Proc. Natl. Acad. Sci. USA* 93.7 (1996), pp. 2926–2929. DOI: `10.1073/pnas.93.7.2926`.

[21] S. J. Singer and G. L. Nicolson. "The fluid mosaic model of the structure of cell membranes". In: *Science* 175.4023 (1972), pp. 720–731. DOI: `10.1126/science.175.4023.720`.

[22] B. Habermann. "The BAR-domain family of proteins: a case of bending and binding?" In: *EMBO Rep.* 5.3 (2004), pp. 250–5. DOI: `10.1038/sj.embor.7400105`.

[23] M. Simunovic et al. "When physics takes over: BAR proteins and membrane curvature". In: *Trends Cell Biol.* 25.12 (2015), pp. 780–792. DOI: `10.1016/j.tcb.2015.09.005`.

[24] C. Prévost et al. "IRSp53 senses negative membrane curvature and phase separates along membrane tubules". In: *Nat. Commun.* 6 (2015), p. 8529. DOI: `10.1038/ncomms9529`.

[25] K. Simons and G. Van Meer. "Lipid sorting in epithelial cells". In: *Biochemistry* 27.17 (1988), pp. 6197–6202. DOI: `10.1021/bi00417a001`.

[26] S. Thomas et al. "Analysis of lipid rafts in T cells". In: *Mol. Immunol.* 41.4 (2004), pp. 399–409. DOI: `10.1016/j.molimm.2004.03.022`.

[27] S. Munro. "Lipid rafts: elusive or illusive?" In: *Cell* 115.4 (2003), pp. 377–388. DOI: `10.1016/S0092-8674(03)00882-1`.

[28] G. van Meer, D. R. Voelker, and G. W. Feigenson. "Membrane lipids: where they are and how they behave". In: *Nat. Rev. Mol. Cell Biol.* 9.2 (2008), pp. 112–124. DOI: `10.1038/nrm2330`.

[29] D. A. Fletcher and R. D. Mullins. "Cell mechanics and the cytoskeleton". In: *Nature* 463.7280 (2010), pp. 485–92. DOI: `10.1038/nature08908`.

[30] R. C. Weisenberg. "Microtubule formation in vitro in solutions containing low calcium concentrations". In: *Science* 177.4054 (1972), pp. 1104–1105. DOI: `10.1126/science.177.4054.1104`.

[31] M. E. Janson, M. E. de Dood, and M. Dogterom. "Dynamic instability of microtubules is regulated by force". In: *J. Cell Biol.* 161.6 (2003), pp. 1029–1034. DOI: `10.1083/jcb.200301147`.

[32] F. Huber et al. "Emergent complexity of the cytoskeleton: From single filaments to tissue". In: *Adv. Phys.* 62.1 (2013), pp. 1–112. DOI: `10.1080/00018732.2013.771509`.

[33] A. G. Hendricks et al. "Motor coordination via a tug-of-war mechanism drives bidirectional vesicle transport". In: *Curr. Biol.* 20.8 (2010), pp. 697–702. DOI: 10.1016/j.cub.2010.02.058.

[34] F. Verde. "Taxol-induced microtubule asters in mitotic extracts of Xenopus eggs: requirement for phosphorylated factors and cytoplasmic dynein". In: *J. Cell Biol.* 112.6 (1991), pp. 1177–1187. DOI: 10.1083/jcb.112.6.1177.

[35] T. Gaglio, A. Saredi, and D. A. Compton. "NuMA is required for the organization of microtubules into aster-like mitotic arrays". In: *J. Cell Biol.* 131.3 (1995), pp. 693–708. DOI: 10.1083/jcb.131.3.693.

[36] V. Mountain et al. "The kinesin-related protein, HSET, opposes the activity of Eg5 and cross-links microtubules in the mammalian mitotic spindle". In: *J. Cell Biol.* 147.2 (1999), pp. 351–365. DOI: 10.1083/jcb.147.2.351.

[37] K. Clark et al. "Myosin II and mechanotransduction: a balancing act". In: *Trends Cell Biol.* 17.4 (2007), pp. 178–186. DOI: 10.1016/j.tcb.2007.02.002.

[38] M. Vicente-Manzanares et al. "Non-muscle myosin II takes centre stage in cell adhesion and migration". In: *Nat. Rev. Mol. Cell Biol.* 10.11 (2009), pp. 778–790. DOI: 10.1038/nrm2786.

[39] K. N. Dahl, E. A. Booth-Gauthier, and B. Ladoux. "In the middle of it all: Mutual mechanical regulation between the nucleus and the cytoskeleton". In: *J. Biomech.* 43.1 (2010), pp. 2–8. DOI: 10.1016/j.jbiomech.2009.09.002.

[40] K. Riento and A. J. Ridley. "ROCKs: multifunctional kinases in cell behaviour". In: *Nat. Rev. Mol. Cell Biol.* 4.6 (2003), pp. 446–456. DOI: 10.1038/nrm1128.

[41] N. Lane. "The unseen world: reflections on Leeuwenhoek (1677) 'Concerning little animals'". In: *Philos. Trans. R. Soc. B Biol. Sci.* 370.1666 (2015), pp. 1–10. DOI: 10.1098/rstb.2014.0344.

[42] E. Abbe. "Beiträge zur Theorie des Mikroskops und der mikroskopischen Wahrnehmung". In: *Arch. für Mikroskopische Anat.* 9.1 (1873), pp. 413–418. DOI: 10.1007/BF02956173.

[43] S. B. Ippolito, B. B. Goldberg, and M. S. Ünlü. "Theoretical analysis of numerical aperture increasing lens microscopy". In: *J. Appl. Phys.* 97.5 (2005). DOI: 10.1063/1.1858060.

[44] L. de Broglie. "Waves and Quanta". In: *Nature* 112.2815 (1923), p. 540. DOI: 10.1038/112540a0.

[45] J. B. Park et al. "Non-destructive electron microscopy imaging and analysis of biological samples with graphene coating". In: *2D Mater.* 3.4 (2016), p. 045004. DOI: 10.1088/2053-1583/3/4/045004.

[46] O. Shimomura, F. H. Johnson, and Y. Saiga. "Extraction, purification and properties of aequorin, a bioluminescent protein from the luminous Hydromedusan, Aequorea". In: *J. Cell. Comp. Physiol.* 59.3 (1962), pp. 223–239. DOI: 10.1002/jcp.1030590302.

[47] G. J. Kremers et al. "Fluorescent proteins at a glance". In: *J. Cell Sci.* 124.15 (2011), p. 2676. DOI: 10.1242/jcs.095059.

[48] T. Terai and T. Nagano. "Small-molecule fluorophores and fluorescent probes for bioimaging". In: *Pflugers Arch. Eur. J. Physiol.* 465.3 (2013), pp. 347–359. DOI: 10.1007/s00424-013-1234-z.

[49] G. J. Phillips. "Green fluorescent protein – a bright idea for the study of bacterial protein localization". In: *FEMS Microbiol. Lett.* 204.1 (2001), pp. 9–18. DOI: 10.1111/j.1574-6968.2001.tb10854.x.

[50] W. Moerner and L. Kador. "Optical detection and spectroscopy of single molecules in a solid". In: *Phys. Rev. Lett.* 62.21 (1989), pp. 2535–2538. DOI: 10.1103/PhysRevLett.62.2535.

[51] M. Orrit and J. Bernard. "Single pentacene molecules detected by fluorescence excitation in a p-terphenyl crystal". In: *Phys. Rev. Lett.* 65.21 (1990), pp. 2716–2719. DOI: 10.1103/PhysRevLett.65.2716.

[52] E. Betzig et al. "Imaging intracellular fluorescent proteins at nanometer resolution". In: *Science* 313.5793 (2006), pp. 1642–1645. DOI: 10.1126/science.1127344.

[53] K. I. Willig et al. "Nanoscale resolution in GFP-based microscopy". In: *Nat. Methods* 3.9 (2006), pp. 721–723. DOI: 10.1038/nmeth922.

[54] S. Weisenburger et al. "Cryogenic optical localization provides 3D protein structure data with Angstrom resolution". In: *Nat. Methods* 14.2 (2017), pp. 141–144. DOI: 10.1038/nmeth.4141.

[55] K. Xu, G. Zhong, and X. Zhuang. "Actin, spectrin, and associated proteins form a periodic cytoskeletal structure in axons". In: *Science* 339.6118 (2013), pp. 452–6. DOI: 10.1126/science.1232251.

[56] D. Baddeley et al. "Light-induced dark states of organic fluochromes enable 30 nm resolution imaging in standard media". In: *Biophys. J.* 96.2 (2009), pp. L22–L24. DOI: 10.1016/j.bpj.2008.11.002.

[57]   E. J. Peterman, H. Sosa, and W. Moerner. "Single-molecule fluorescence spectroscopy and microscopy of biomolecular motors". In: *Annu. Rev. Phys. Chem.* 55.1 (2004), pp. 79–96. DOI: `10.1146/annurev.physchem.55.091602.094340`.

[58]   J. Jonkman and C. M. Brown. "Any way you slice it—A comparison of confocal microscopy techniques". In: *J. Biomol. Tech.* 26.2 (2015), pp. 54–65. DOI: `10.7171/jbt.15-2602-003`.

[59]   M. Nelson et al. "Spinning disk confocal microscopy of calcium signaling in blood vessel walls". In: *Eur. J. Neurosci.* 34.4 (2011), pp. 561–568.

Chapter 2

Retention of neuronal receptors induced by spine-morphology†

Here we show that the morphology of the dendritic spine can be a significant determinant for regulating memory and learning. Using an artificial system that models the dendritic spine in a giant unilamellar vesicle, we experimentally confirmed the significance of spine-morphology on the escape of membrane-bound receptors from the spine, a process called 'the narrow escape problem'. Our results show that retention within the spine scales with spine-size beyond the predicted quadratic dependence reflecting the surface area. We show that the morphology of some dendritic spines can slow down the escape of receptors enough to give other biochemical processes a significant time-window to be set in motion. Furthermore, our analysis yields that the size of the spine-head determines receptor retention, rather than the length of the spine-neck.

2.1   Introduction

The brain is arguably the most complex organ in humans. It consists of almost 100 billion neurons which are interconnected by approximately 1000 connections each. Those connections, the synapses, are at the base of the brain's processing capabilities and its memory. Signals are transmitted between neurons by neurotransmitters which are released from the pre-synaptic neuron and detected by specialized transmembrane receptors on the post-synaptic neuron (figure 2.1). The processes of learning and memory are encoded by a change in the coupling strengths between synapses. This coupling strength is governed by the receptor density at the post-synaptic side. An increase in receptor density strengthens, while a decrease in receptor density weakens the coupling [1]. Hence, for memory, a constant receptor density in the synapse is required. One way to achieve a constant density would be to capture and immobilize all receptor molecules at the synapse. Yet, to a surprise, it was found, initially by fluorescence recovery after photobleaching experiments [2], and since firmly confirmed by single-molecule tracking [3–7] and superresolution microscopy [6], that receptors are mobile within the post-synaptic space, contradicting the earlier believe.

Simultaneously with the change in connection strength and receptor density, the postsynaptic neuron changes shape [8, 9]. Extensive studies using state-of-the-art electron microscopy [10] established a sequence of particular morphological changes at the location of the synaptic connection described by the formation of the so-called synaptic spine. With increasing coupling strength the spine changes morphology. From what is initially a small protrusion, it grows into a fully developed mushroom-shaped mature spine with a head typically a few tens of micrometers in diameter, being connected to the postsynaptic neuron through a very narrow membrane tube, or neck, of about ten to hundred nanometer diameter [11, 12]. Recently, the morphological change on learning has been followed directly in live cells [13] and in a live animal [14].

Those two observations have led to a unifying model for learning and memory that allows for the observed receptor mobility within the spine, which is required for short-term synaptic variability and likewise preventing swift loss of receptor density. The narrow neck slows down the escape of receptors from the dendritic spine, allowing other biochemical processes to kick in and ultimately keep the number of receptors in a dendritic spine at a constant level. One structure which is known to hinder the escape of receptors is the presence of a septin meshwork in the dendritic spine neck [15]. This model unites the seemingly mutually exclusive observations of receptor mobility and
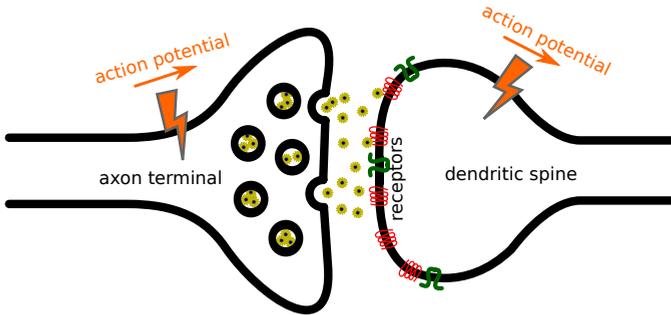
Figure 2.1: **The synapse.** Upon arrival of an action potential in the axon terminal, neurotransmitters are released into the synaptic cleft and are sensed by receptors in the membrane of the dendritic spine. In turn voltage channels are opened creating a new action potential in the dendrite.

receptor confinement. Theoretically, the geometric problem has been described in terms of the "narrow escape problem" [16]. Analytical studies [16], together with a recent simulation approach [17], have predicted that the change of morphology can, at least partially, explain how mobile receptors are restricted to the spine and thereby guarantee a stable strength of the synapse [18]. It is worth mentioning, that the narrow neck might also lead to a reduction in dimensionality for receptor diffusion, which can lead to unexpected behavior in biological processes [19]. Here, we set out for an experimental verification of the narrow-escape model.

2.2 Results

2.2.1 Mimetic system of the synaptic spine

We created an artificial system that mimics the mushroom-like morphology of the dendritic spine. This artificial system allowed us to set and vary the leading parameters defining the morphology in a large range, embracing those found in the brain. Our mimetic system consists of giant unilamellar vesicles (GUVs), from which membrane tubes were pulled. For the generation of GUVs, we used the process of electroswelling from pure phospholipids [20]. The size-range of GUVs was varied from 4 to 20 µm. Such size-span of almost one order of magnitude has been reported for the heads of dendritic spines *in vivo* [12].

The spine neck we realized by pulling a membrane patch from the GUV by a fine pipette. Slight suction with simultaneous retraction of the pipette from the GUV using a micromanipulator allowed us to form a membrane tube of variable length. The resulting shape is depicted in figure 2.2 as a cross-section. It has been shown that the radius r of the tube depends on the square root of the ratio of the bending modulus and the surface tension of the membrane [21]. Whereas the bending modulus is a characteristic of the phospholipids used, the tension is determined by the method by which the GUVs were produced. The latter varied for each of our preparations. Hence the tube radius was determined experimentally in each experiment. It varied in a narrow window centered at 200 nm (Supplementary figure 2.10).
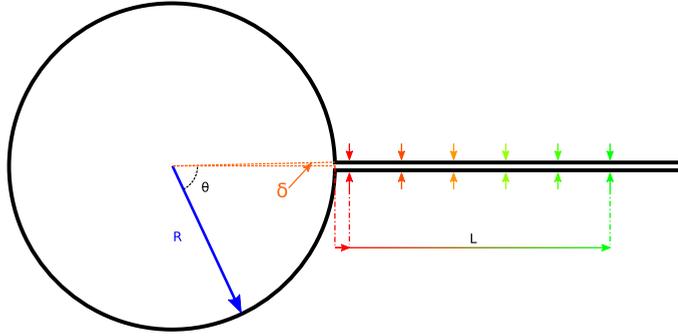
Figure 2.2: **Cross-section of the experimental system.** The dendritic spine head was mimicked by a giant unilamellar vesicle of radius R. The spine neck was simulated by a membrane nanotube of radius r. Lipid-anchored quantum dots served as surrogate of membrane receptors. Receptor escape was monitored by observation of quantum-dots that crossed a virtual finish-line at distance $L_0 = 2\,\mu m$ (red arrows) up to $L = 10\,\mu m$ (other arrows) into the tube.

Lastly, receptor proteins were imitated by lipids which were labeled by individual fluorescent quantum-dots. Trajectories of individual lipid-anchored quantum dots undergoing diffusion on the membrane were followed at high spatial (20 nm) and temporal (30 ms) resolution on a wide-field single-molecule microscope (figure 2.3). For comparison of results obtained in our biomimetic system with those *in vivo*, the higher mobility of lipids with respect to transmembrane receptors had to be considered. Given the about hundred-fold higher

values of the diffusion constants for the mimetic with respect to the *in vivo* situation ($0.5\,\mu m^2/s$ *vs.* $0.01\,\mu m^2/s$ [22]), in combination with the about ten times lager size R of the mimetic versus the *in vivo* systems (2 - 50 μm *vs.* 0.1 - 1 μm [23]), we predicted that the timescales we found are about similar in the *in vivo* systems given the scaling of diffusion processes R^2/D .
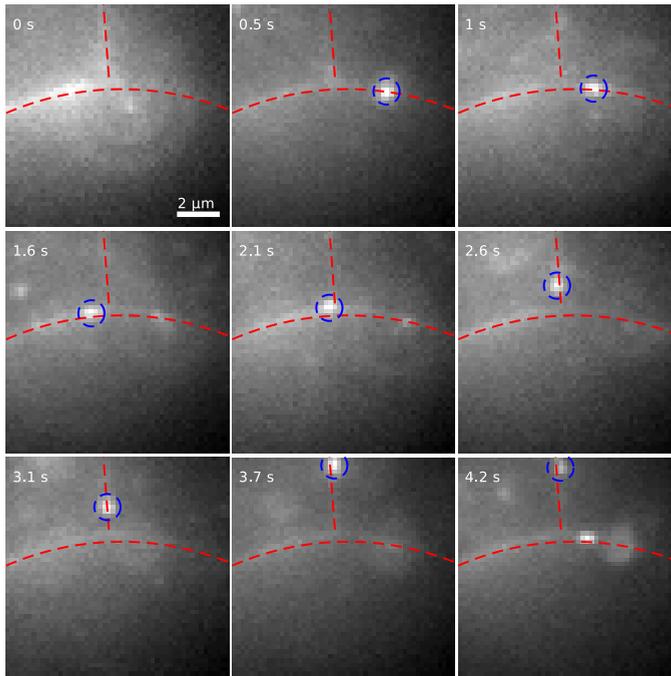
Figure 2.3: **Example of an escape event in an artificial dendritic spine.** A quantum dot mimicking a receptor in a GUV/tube system (marked by the red line) was followed in time. Initially, the quantum dot (bright signal) was outside the depth of focus. At $t = 0.5\,s$, it appeared in focus (marked by the blue circle) on the membrane of the GUV. After about 2.5 s it entered the tube in which it diffused further. After about 3.5 s it is passed the finish line at $L_0 = 2\,\mu m$ and was counted as escaped.

2.2.2   Diffusion constant

We were interested in the rate at which receptors, i.e. lipid-anchored quantum-dots, escaped the dendritic spine. Therefore we used single-molecule microscopy to follow individual lipid-anchored quantum dots on the membrane in the vesicle/tube mimetic. Individual quantum dots were followed at high spatial (20 nm) and temporal (30 ms) resolution for an extensive time-scale (up to 10 s) in an axial slice of $\sim 1\,\mu$m thickness through the GUV. The imaging plane contained the plane of the membrane tube (figure 2.3). A selection of typical trajectories is shown in figure 2.4. The observed trajectories were split into several modes which encompass all our observations: (i) quantum dots which diffused on the membrane of the GUV within our observation slice, (ii) quantum dots that diffused on the membrane of the GUV and left the observation slice in axial direction, (iii) quantum dots that diffused up and down the membrane tube, (iv) quantum dots that diffused out of the GUV into the tube or *vice versa*. The latter were the events that we further analyzed in terms of the escape problem.
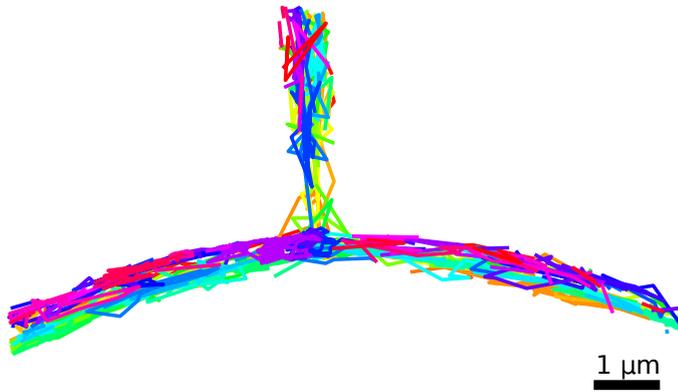
Figure 2.4: **Selection of trajectories of quantum dots on the surface of an artificial dendritic spine.** The selection includs the trajectory of the quantum dot tracked in figure 2.3. Colors denote different trajectories.

An example of a quantum dot (encircled in blue) that escaped the artificial spine (outlined in red) is shown in figure 2.3. The sequence was recorded at 9.5 Hz, such that the imaging kept up with the movement of the quantum dot. Initially, the quantum dot was not visible. At $t = 0.5$ s, the quantum dot appeared in the image plane of the GUV (bottom) that contained the long membrane tube (top). After 2.5 s the quantum dot entered the tube. 1 s later it passed the virtual finish line we defined at $L_0 = 2\,\mu\text{m}$ into the tube and was counted as having escaped the system. L_0 was chosen such that it's location on the tube was clearly separated from the membrane of the giant vesicle.

The sole parameter that controls the relation between displacement and time-scale in the problem is the diffusion constant, D. D was determined from the diffusional trajectories in modes (i) and (iii) by fitting the one-dimensional mean squared displacement along the membrane as a function of the time-lag between two observations for each vesicle. The diffusion constant had an average value of $D = (0.5 \pm 0.1)\,\mu\text{m}^2/\text{s}$, (figures 2.8 and 2.9). This value coincides with diffusion constants of bead- and quantum-dot labelled lipids [24], yet are smaller than that for fluorophore-labeled lipids reported to be 1 - 4 $\mu\text{m}^2/\text{s}$ [25]. Next to the diffusion constant, analysis of trajectories in mode (iii) permitted to experimentally determine the sub-diffraction sized radius of the tube, r [26]. Trajectories were first split into movements parallel and perpendicular to the tube-direction before the respective mean-squared displacements $\text{MSD}_\parallel$ and $\text{MSD}_\perp$ were determined. Subsequently the time-dependence of the MSDs was determined. Where $\text{MSD}_\parallel(t)$ increased linearly in time as $\text{MSD}_\parallel(t) = 2Dt$, the perpendicular component saturated for long timescales to $\text{MSD}_\perp(t \to \infty) = r^2$ [26]. From the latter value the tube radius was determined. The tube radii were in the range $r = 150\,\text{nm}$ to $300\,\text{nm}$ (figure 2.10).

2.2.3 Escape rate

The methodology described in the previous subsection permitted us to directly determine the time of escape from the GUV for each quantum dot directly. However, statistics in such an approach was low given that our imaging approach required that the quantum dots stayed within the depth of focus during the entire experiment. Yet most of the trajectories we observed fall into mode (ii), where quantum dots moved out of the observation volume in the axial direction. Therefore the escape rate was determined statistically. We counted the number of quantum dots n that passed a virtual finish-line at position L in the tube within the time-period of observation Δt. The latter was set to 100 s yielding sufficient events n in each experiment. Subsequently, the escape rate E was determined by normalization of n by the total number of particles N on each

GUV:

$$E = \frac{n}{N\Delta t} \tag{2.1}$$

N was determined experimentally for each GUV by counting the total number of particles visible in the plane of focus and taking into account the depth of focus of our microscope (see the M&M subsection).

The escape rate is a Kramers' rate, which is related to the mean first passage time τ (MFPT) by [27]

$$\frac{1}{E} = \tau \tag{2.2}$$

It is worth noting that the escape rate is only dependent on the geometry of the artificial dendritic spine and the diffusion constant, given that ER^2/D is a unitless quantity. Thus we expected that the escape rate would scale as R^{-2}, the inverse of the surface area of the GUV.

2.2.4   Dependence of escape rate on GUV radius

We analyzed the escape rate for a range of GUV-tube systems. In order to reduce broadening of the data due to differences in the diffusion constants for different vesicles (see figure 2.8), escape rates E were normalized by D. The results for the ratio E/D are shown in figure 2.5 where the radius R of the GUV was varied between 4 - 20 µm. Data are shown in blue and include standard errors represented by blue bars. The range of values of 10^{-5} - $10^{-3}/\mu m^2$ found for E/D translates into mean-first-passage times between 8 min and 1 day, taking into account the diffusion constant of $D = 0.5\,\mu m^2/s$ reported above. A fit to a power-law $E/D = \Gamma R^{-\alpha}$ (red line) revealed that the escape rate scaled with an exponent $\alpha = 2.6 \pm 0.3$ of the vesicle radius. Hence the dependence was stronger than the quadratic dependence predicted from scaling with the surface area of the GUV. The mobility factor was determined to $\Gamma = (0.27 \pm 0.18)\,\mu m^{\alpha - 2}$.

As noted earlier, the system under study is an example of the narrow-escape problem. An analytical solution for the MFPT of the narrow-escape problem has been derived for particles diffusing on a spherical shell attached to a cylindrical tube [28]. The solution for an arbitrary starting point on the GUV, as defined by the the polar angle θ with respect to the plane of the membrane tube is given by [28]:

$$E(\theta, R, L) = D \left[2R^2 \log\left(\frac{\sin \theta/2}{\sin \delta/2}\right) + \frac{L^2}{2} + \frac{2R^2L}{r} \right]^{-1} \tag{2.3}$$
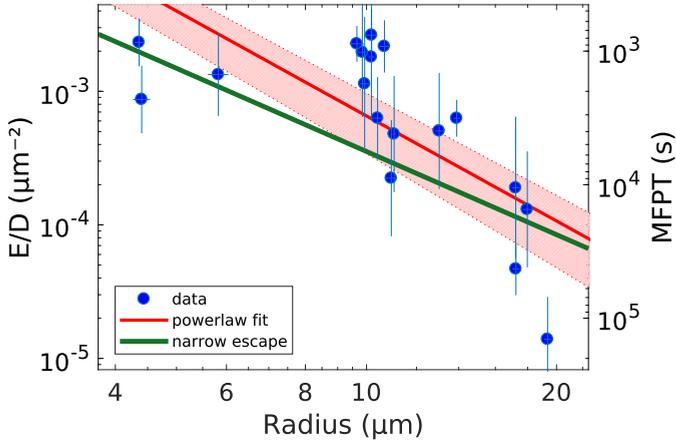
Figure 2.5: **Ratio of escape rate and diffusion constant (E/D) for
changing GUV-radius.** Data-points and standard errors are shown in blue.
The red line follows a power-law fit to the data yielding an exponent of
-2.6 ± 0.3. The prediction interval for this fit is shown as red-shaded re-
gion. The green line displays the full theoretical prediction for a vesicle/tube
geometry [28], with tube-radius $r = 200\,\text{nm}$, and tube-length $L_0 = 2\,\mu\text{m}$

The opening of the attached membrane tube $\delta = \arcsin\left(r/R\right)$ defines the
minimum possible angle in θ. Integration of equation (2.3) with respect to all
starting positions on the sphere leads to an expression for the total escape rate
as measured in our experiments (see supplementary section 2.6.1):

$$\frac{E(R,L)}{2Dr^{-2}} = \left[\frac{4R^2}{r^2} \left(\frac{\log\left(\frac{2}{1-\sqrt{1-r^2/R^2}}\right)}{1+\sqrt{1-r^2/R^2}} + \frac{L}{r} - 1 \right) + \frac{L^2}{r^2} \right]^{-1} \tag{2.4}$$

The result of equation (2.4) for a mean tube radius $r = 200\,\text{nm}$ and
$L = L_0 = 2\,\mu\text{m}$ was added to figure 2.5 (green line). The analytical curve
follows the experimental data within experimental uncertainty. It should be
stressed that the analytical curve does not contain any free parameter.

2.2.5   Dependence of the escape rate on tube length

Besides the size of the head R, a second shape parameter determining the escape rate is the length of the tube L. In contrast to the GUV radius, L was modified by repositioning the virtual finish-line on the tube. Whereas, in the experiments referred to in the last subsection we kept $L = L_0 = 2\,\mu\text{m}$ constant, here L was varied between 2 and 6 μm.

In order to retrieve the scaling behavior of the escape rate on L, we rescaled all results by the power-law dependence $R^{-\alpha}$, $\alpha = 2.6$, that we experimentally determined in the last subsection. After this rescaling, all data fall onto a single master curve (figure 2.5), which allowed us to analyze all experiments globally, and independent of R. It should be noted, that the rescaled data also includes the linear term L/r in equation (2.4) which accounts for molecules that returned into the GUV before crossing the finish line defined by L [28]. The inverse of the rescaled ratio of escape-rate to diffusion constant is well approximated by a second-order polynomial in L, reading

$$\left[\frac{E(R,L)}{D\,\Gamma R^{-\alpha}} \right]^{-1} = 1 + p\,(L - L_0)^2 \qquad (2.5)$$

As predicted for diffusion, the inverse escape-rate increases quadratically with the tube length. All data closely followed the behavior predicted from equation (2.5) (figure 2.6). Each data point (blue line) in figure 2.6 is the average scaled inverse escape-rate $D\Gamma R^{-\alpha}/E$ at a given position L on the tube. The red line represents a free fit of the data to equation (2.5), yielding values for the parameter $p = (1.84 \pm 0.03)/\mu\text{m}^2$.

2.3   Discussion & Conclusion

The system described here is a very simplified model for a real dendritic spine, yet it is complex enough to display some of the essential ingredients. Our data demonstrate the dependence of the escape rate on morphology. The escape-rate from the head of a dendritic spine into the tube decreases about a hundred-fold when the size of the head is increased five-fold. This shows that the dependence exceeds the scaling that would be predicted solely by the quadratic increase in surface area. In addition, increasing the length of the tube that connects the head of the dendritic spine to the axon, decreases the escape rate further. The quadratic dependence of the escape rate E on the length of the tube L is recovered from our data. Increasing the length of the tube L three-fold decreases the escape rate thirty-fold.
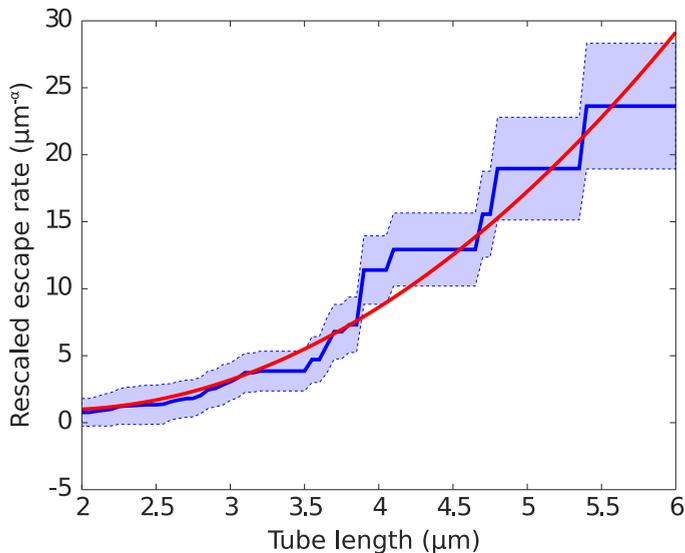
Figure 2.6: **Escape-rate versus tube length.** Inverse of the ratio of the rescaled escape-rate to the diffusion constant with increasing tube length.

A quantitative comparison between the influence of the neck- *vs.* the head-region is given in figure 2.7. From the figure it becomes apparent that the size of the head is dominant with respect to retention of receptors out of the spine. The dashed lines represent geometries for which the mean first-passage time is 1 s, 1 min, 1 h, and 12 h, respectively. The timescales we determined for lipid escape on the model system of 8 min - 1 day are about one order of magnitude longer than we would predict in the spine, since the model system is larger than typical structures observed *in vivo* by about two orders of magnitude, and the diffusion constant in the mimetic system ($D = 0.5\,\mu\mathrm{m}^2/\mathrm{s}$) is about one order of magnitude higher than the receptor diffusion constant reported in the spine ($D = 0.02\,\mu\mathrm{m}^2/\mathrm{s}$, [15]).
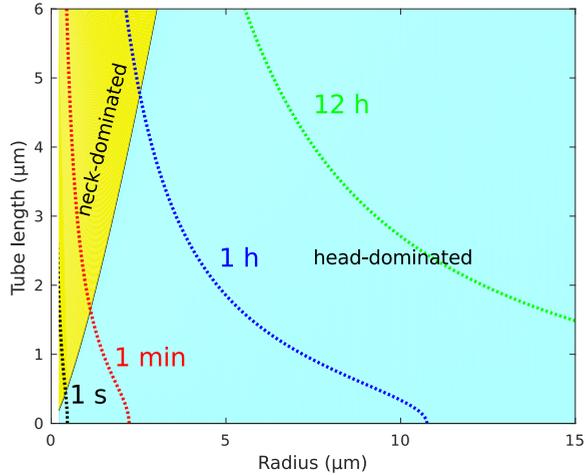
Figure 2.7: **A quantitative comparison between the influence of the neck- *vs.* the head-region.** is given in figure 2.7. The blue region indicates the morpholgy of the system where the radius of the head is the dominant determiner for the retention of receptors. The yellow region indicates the morpholgy of the system where the radius of the neck is the dominant determiner for the retention of receptors. The dashed lines represent geometries for which the mean first-passage time is 1 s (black), 1 min (red), 1 h (blue), and 12 h (green), respectively.

Although our analysis clearly shows the influence of spine morphology on the escape rate, the retention times up to a few hours in our mimetic system, which translates to minutes in a real dendritic spine, would be clearly insufficient for the long-term memory capability of our brain. It is obvious that our simple mimetic system lacks the large number of proteins which cells have, some of which are known to inhibit diffusion on the spine membrane and through the spine neck [7, 15, 29]. Hence, certainly for memory and learning these mechanisms together with active transport of receptors towards the synapse will be the main determinants.

Yet, the reduction of the escape rate due to morphology may play a role in the initial formation of neuronal connections, leaving sufficient time that other structural rearrangements like those mentioned above can be built up. It is known that developing dendritic spines start out as a protrusion, without a restricting neck region, reducing passage times to probably far under a second. In these young spines, therefore, it is very easy to adapt the number of receptors as is required for learning. Conversely, the restricting behavior of specialized proteins and active transport of new receptors into the dendritic spine, aided by the minutes-long passage times in dendritic spines with large heads and long necks, achieve a life-long memory or long-term potentiation (LTP).

2.4 Acknowledgements

2.5 Materials and Methods

2.5.1 GUV preparation

Giant unilamellar vesicles (GUVs) were prepared using electroswelling [20]. 20 µl lipids (1,2-dioleoyl-*sn*-glycero-3-phosphocholine (Avanti Polar Lipids 850375C, DOPC) and 1,2-dioleoyl-*sn*-glycero-3-phosphoethanolamine-N-(biotinyl) (Avanti Polar Lipids 870282C, bioDOPE)) dissolved in chloroform ($2\,g/L$) were deposited on top of two indium tin oxide (ITO) coated glasses (total covered area about $10\,cm^2$). The chloroform was evaporated for two hours using a desiccator. Subsequently the coated glasses were placed parallel, coated sides facing each other in a teflon enclosure with about $3\,mm$ separation between them. The space between the glasses was filled with $230\,mOsmol/kg$ sucrose. Swelling was done for two hours at $10\,Hz$, $4\,V_{pp}$ sinusoidal excitation. After that the sucrose solution containing the GUVs was extracted from the chamber.

2.5.2   Receptor mimicry

Quantum dots (Qdot705 Streptavidin Conjugate; Q10163MP, Life Technologies) were gently mixed with GUVs after electroswelling. Then GUVs were diluted $40\times$ in $300\,\mathrm{mOsmol/kg}$ phosphate buffered saline (PBS). The streptavidin-coated quantum dots bound to the biotinylated lipids of the GUV membranes (about 1% bioDOPE. The microscope coverglass was treated with $1\,\mathrm{mL}$, $1\,\mathrm{g/L}$ BSA-biotin (Sigma) and $1\,\mathrm{mL}$, $60\,\mathrm{\mu g/L}$ neutravidin (Sigma), for fifteen minutes each, and washed with PBS after and in between, to enable the GUVs to bind to the glass.
A membrane nanotube was pulled out of the GUV with a micromanipulator (Narishige MW3) equipped with a glass microneedle (Harvard glass) pulled into a tip with an opening less than $1\,\mathrm{\mu m}$ in diameter (Sutter Puller P90). GUVs were gently punched with the needle until the membrane was stuck to the needle. Subsequently, the needle was retracted and a membrane nanotube was formed.

2.5.3   Imaging

Imaging was performed on an epi-fluorescence microscope. Illumination was performed using a $488\,\mathrm{nm}$, $100\,\mathrm{mW}$ laser (Coherent Sapphire 488-100 CW CDRH). The laser beam was modulated by an acousto-optical tunable filter (AA-OptoElectronic, AOTFnC-VIS) to illuminate the sample only when the camera was in exposure mode. Via a tube-lens, the laser beam was coupled into a Zeiss Axiovert 100 microscope fitted with a Zeiss $100\times$ NA 1.4 oil immersion objective resulting in Köhler illumination of the sample. The excitation and emission paths were split using a dichroic mirror (Semrock Di01-R405/488/561/635) and an emission filter (Chroma ZET405/488/561/640m). Detection was done using a CCD camera (Roper Scientific/Princeton Instruments 1340B combined with an ST133 controller and WinView32 software), cooled to $-90\,\mathrm{^\circ C}$ using liquid nitrogen.

2.5.4   Particle tracking

Images were analyzed using home-made Matlab software as described before [30]. Briefly, because the size of a single quantum dot was in the range of $10\,\mathrm{nm}$, the photons emitted were spread on the pixels of the CCD sensor by the point spread function of the microscope. These signals were fit to two-dimensional Gaussians, resembling the point-spread function. In this way,

we were able to determine the center-of-mass position of the quantum dots with up to 20 nm-precision. Tracking the quantum dots was done as described earlier [31], by calculating the probability that a particle in frame n is the same particle in frame $n + 1$ and maximizing this probability with respect to other connectivities.

2.5.5 Escape rate

After obtaining the tracks, the number of particles that escaped the system per unit of time was counted. In most experiments a particle was counted when it crossed a virtual plane perpendicular to the tube at $L = L_0 = 2\,\mu m$ from the edge of the GUV (figure 2.2). In other experiments the distance L was varied. This number was subsequently normalized to the total number of particles N on the GUV. In this way the escape rate E was calculated:

$$E = f\frac{n}{N} = f\frac{n}{n_{\text{vis}}}\frac{lz}{4\pi R^2} \tag{2.6}$$

Here n is the total number of particles that escaped during the whole experiment. $f = 9.5\,\text{Hz}$ is the frame-rate of the camera. The total number of particles N on the GUV was estimated using the visible number of particles in all frames and the fraction of the GUV surface area that is visible in the field of view lz/A, with l the length of the contour in the field of view, z the depth of focus, and $4\pi R^2$ the surface area of the GUV. In this definition the escape rate E is a Kramers' rate. Therefore the escape rate E is related to the mean first passage time τ (MFPT) frequently referred to in literature [32]:

$$\tau = \frac{1}{E} \tag{2.7}$$

2.6 Supplementary information

2.6.1 Angular average of the escape rate

The equation for the escape rate equation (2.3) in general contains a term that describes escape from the head to the tube, and a term for escape from the tube. Here we will focus just on the first:

$$\begin{aligned}
\tau_{\text{head}}(\theta) &= \frac{2R^2}{D}\log\left(\frac{\sin{\theta/2}}{\sin{\delta/2}}\right) \\
&= \frac{2R^2}{D}\left(\log(\sin{\theta/2}) - \log(\sin{\delta/2})\right)
\end{aligned} \tag{2.8}$$

The earlier escape rate contains the starting position of the diffusing object in terms of its azimuthal angle θ with respect to the line defined by the membrane tube. To obtain an average escape rate equation (2.8) must be averaged for all angles:

$$
\begin{aligned}
\langle \tau_{\text{head}} \rangle_\theta &= \frac{\int_0^{2\pi} \int_\delta^\pi \tau_{\text{head}}(\theta) R^2 \sin\theta \, \mathrm{d}\theta \, \mathrm{d}\phi}{\int_0^{2\pi} \int_\delta^\pi R^2 \sin\theta \, \mathrm{d}\theta \, \mathrm{d}\phi} \\
&= \frac{\int_\delta^\pi \tau_{\text{head}}(\theta) \sin\theta \, \mathrm{d}\theta}{\int_\delta^\pi \sin\theta \, \mathrm{d}\theta}
\end{aligned}
\tag{2.9}
$$

Using the definitions

$$
\begin{aligned}
A &= \cos\delta = \sqrt{1 - r^2/R^2} \\
B &= \cos\theta \; ; \; \sin\theta \, \mathrm{d}\theta = -\mathrm{d}B
\end{aligned}
\tag{2.10}
$$

Equation (2.9) becomes

$$
\begin{aligned}
\langle \tau_{\text{head}} \rangle_\theta &= \frac{\int_{-1}^A \tau_{\text{head}}(\theta) \, \mathrm{d}B}{\int_{-1}^A \mathrm{d}B} \\
&= \frac{R^2}{D(1+A)} \int_{-1}^A \log\left(\frac{1-B}{2}\right) - \log\left(\frac{1-A}{2}\right) \mathrm{d}B \\
&= \frac{R^2}{D(1+A)} \left(\int_{-1}^A \log\left(\frac{1-B}{2}\right) \mathrm{d}B - \int_{-1}^A \mathrm{d}B \log\left(\frac{1-A}{2}\right) \right)
\end{aligned}
\tag{2.11}
$$

Integration yields,

$$
\begin{aligned}
\langle \tau_{\text{head}} \rangle_\theta &= \frac{R^2}{D(1+A)} \left(\left[(B-1) \log\left(\frac{1-B}{2}\right) - B \right]_{B=-1}^A - (1+A) \log\left(\frac{1-A}{2}\right) \right) \\
&= \frac{R^2}{D(1+A)} \left((A-1) \log\left(\frac{1-A}{2}\right) - A - 1 - (1+A) \log\left(\frac{1-A}{2}\right) \right) \\
&= \frac{R^2}{D} \left(\frac{2 \log\left(\frac{2}{1-A}\right)}{1+A} - 1 \right)
\end{aligned}
\tag{2.12}
$$

which finally leads to the expression used in equation (2.3) for the angle-averaged escape rate from a spherical object of Radius R into a tube of radius r

2.6.2 Diffusion constants
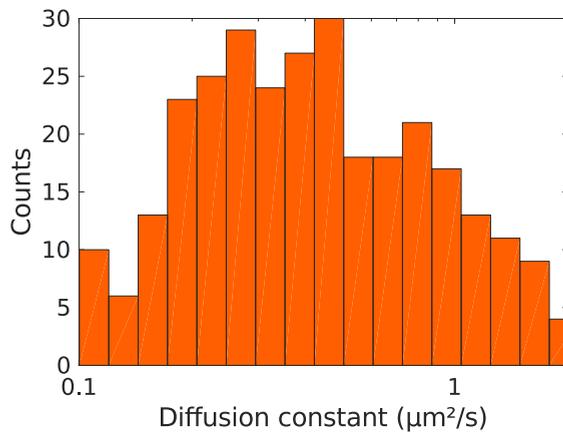
Figure 2.8: **Diffusion constant distribution on the GUV from 320 trajectories.** The average diffusion constant was $D_{GUV} = (0.5 \pm 0.4)\,\mu\text{m}^2/\text{s}$.
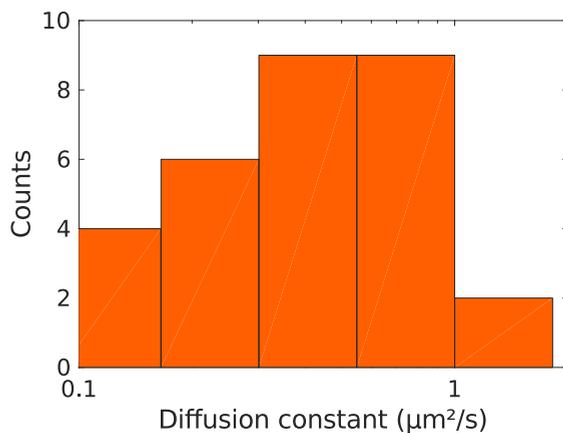

Figure 2.9: **Diffusion constant distribution on the tube from 34 trajectories.** The average diffusion constant was $D_{\text{tube}} = (0.4 \pm 0.3)\,\mu\text{m}^2/\text{s}$.

2.6.3 Tube Radius
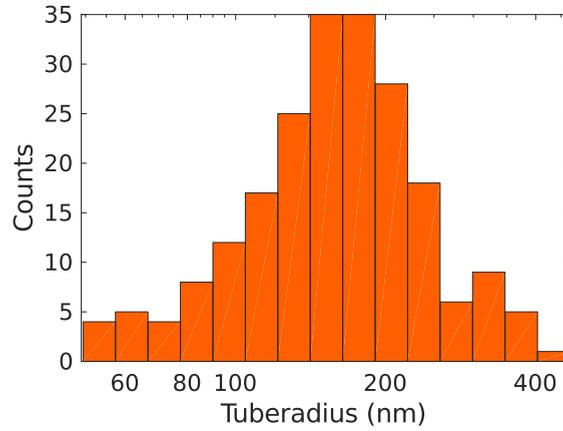
Figure 2.10: **Radii of 22 tubes estimated from the perpendicular diffusion of 212 quantum dots.** The average radius was $r = (200 \pm 50)$ nm.

References

[1] H. Hering and M. Sheng. "Dendritic spine: structure, dynamics and regulation". In: *Nat. Rev. Neurosci.* 2.12 (2001), pp. 880–888. DOI: 10.1038/35104061.

[2] D. Axelrod et al. "Lateral motion of fluorescently labeled acetylcholine receptors in membranes of developing muscle fibers". In: *Proc. Natl. Acad. Sci.* 73.12 (1976), pp. 4594–4598. DOI: 10.1073/pnas.73.12.4594.

[3] A. Sergé et al. "Receptor activation and homer differentially control the lateral mobility of metabotropic glutamate receptor 5 in the neuronal membrane". In: *J. Neurosci.* 22.10 (2002), pp. 3910–3920.

[4] J. Meier et al. "Formation of glycine receptor clusters and their accumulation at synapses". In: *J. Cell Sci.* 113 (2000), pp. 2783–2795.

[5] A. J. Borgdorff and D. Choquet. "Regulation of AMPA receptor lateral movements". In: *Nature* 417.6889 (2002), pp. 649–653. DOI: 10.1038/nature00780.

[6] J. Meier et al. "Fast and reversible trapping of surface glycine receptors by gephyrin". In: *Nat. Neurosci.* 4.3 (2001), pp. 253–260. DOI: 10.1038/85099.

[7] D. Choquet and A. Triller. "The role of receptor diffusion in the organization of the postsynaptic membrane". In: *Nat. Rev. Neurosci.* 4.4 (2003), pp. 251–265. DOI: 10.1038/nrn1077.

[8] T. Schikorski and C. F. Stevens. "Quantitative fine-structural analysis of olfactory cortical synapses". In: *Proc. Natl. Acad. Sci.* 96.7 (1999), pp. 4107–4112. DOI: 10.1073/pnas.96.7.4107.

[9] J. I. Arellano. "Ultrastructure of dendritic spines: correlation between synaptic and spine morphologies". In: *Front. Neurosci.* 1.1 (2007), pp. 131–143. DOI: 10.3389/neuro.01.1.1.010.2007.

[10] J. N. Bourne and K. M. Harris. "Balancing structure and function at hippocampal dendritic spines". In: *Annu. Rev. Neurosci.* 31.1 (2008), pp. 47–67. DOI: 10.1146/annurev.neuro.31.060407.125646.

[11] P. Hotulainen and C. C. Hoogenraad. "Actin in dendritic spines: connecting dynamics to function". In: *J. Cell Biol.* 189.4 (2010), pp. 619–629. DOI: 10.1083/jcb.201003008.

[12] M. Frotscher et al. "Fine structure of synapses on dendritic spines". In: *Front. Neuroanat.* 8.September (2014), pp. 1–9. DOI: 10.3389/fnana.2014.00094.

[13] M. Adrian et al. "Probing the interplay between dendritic spine morphology and membrane-bound diffusion". In: *Biophys. J.* 113 (2017), pp. 1–10. DOI: 10.1016/j.bpj.2017.06.048.

[14] A. Attardo, J. E. Fitzgerald, and M. J. Schnitzer. "Impermanence of dendritic spines in live adult CA1 hippocampus". In: *Nature* 523 (2015), pp. 592–596. DOI: 10.1038/nature14467.

[15] H. Ewers et al. "A septin-dependent diffusion barrier at dendritic spine necks". In: *PLoS One* 9.12 (2014), e113916. DOI: 10.1371/journal.pone.0113916.

[16] D. Holcman and Z. Schuss. "The narrow escape problem". In: *SIAM Rev.* 56.2 (2014), pp. 213–257. DOI: 10.1137/120898395.

[17] R. Kusters et al. "Shape-induced asymmetric diffusion in dendritic spines allows efficient synaptic AMPA receptor trapping". In: *Biophys. J.* 105.12 (2013), pp. 2743–2750. DOI: 10.1016/j.bpj.2013.11.016.

[18] M. Adrian et al. "Barriers in the brain: resolving dendritic spine morphology and compartmentalization". In: *Front. Neuroanat.* 8.12 (2014), pp. 1–12. DOI: 10.3389/fnana.2014.00142.

[19] G. Adam and M. Delbrück. "Reduction of dimensionality in biological diffusive processes". In: *Struct. Chem. Mol. Biol.* 1968, pp. 198–215.

[20] M. I. Angelova and D. S. Dimitrov. "Liposome electroformation". In: *Faraday Discuss. Chem. Soc.* 81 (1986), pp. 303–311. DOI: 10.1039/dc9868100303.

[21] I. Derényi, F. Jülicher, and J. Prost. "Formation and interaction of membrane tubes". In: *Phys. Rev. Lett.* 88.23 (2002), pp. 1–4. DOI: 10.1103/PhysRevLett.88.238101. arXiv: 0205630 [cond-mat].

[22] M. Dahan. "Diffusion dynamics of glycine receptors revealed by single-quantum dot tracking". In: *Science* 302.5644 (2003), pp. 442–445. DOI: 10.1126/science.1088525.

[23] J. N. Bourne and K. M. Harris. "Nanoscale analysis of structural synaptic plasticity". In: *Curr. Opin. Neurobiol.* 22.3 (2012), pp. 372–382. DOI: 10.1016/j.conb.2011.10.019.

[24] M. J. Murcia et al. "Design of quantum dot-conjugated lipids for long-term, high-speed tracking experiments on cell surfaces". In: *J. Am. Chem. Soc.* 130.45 (2008), pp. 15054–15062. DOI: 10.1021/ja803325b.

[25]   A. Sonnleitner, G. J. Schütz, and T. Schmidt. "Free Brownian motion of individual lipid molecules in biomembranes". In: *Biophys. J.* 77.November (1999), pp. 2638–2642. DOI: 10.1016/S0006-3495(99)77097-9.

[26]   S. Wieser et al. "Single molecule diffusion analysis on cellular nanotubules: Implications on plasma membrane structure below the diffraction limit". In: *Appl. Phys. Lett.* 91.23 (2007), p. 233901. DOI: 10.1063/1.2822890.

[27]   D. Boilley, B. Jurado, and C. Schmitt. "Simple relations between mean passage times and Kramers' stationary rate". In: *Phys. Rev. E - Stat. Nonlinear, Soft Matter Phys.* 70.5 2 (2004), pp. 1–4. DOI: 10.1103/PhysRevE.70.056129.

[28]   D. Holcman and Z. Schuss. "Diffusion laws in dendritic spines". In: *J. Math. Neurosci.* 1.10 (2011), pp. 1–14. DOI: 10.1186/2190-8567-1-10.

[29]   B. Winckler et al. "A diffusion barrier maintains distribution of membrane proteins in polarized neurons". In: *Nature* 397.2 (1999), pp. 698–701. DOI: 10.1038/17806.

[30]   T. Schmidt et al. "Imaging of single molecule diffusion". In: *Proc. Natl. Acad. Sci. USA* 93.7 (1996), pp. 2926–2929. DOI: 10.1073/pnas.93.7.2926.

[31]   G. J. Schütz, H. Schindler, and T. Schmidt. "Single-molecule microscopy on model membranes reveals anomalous diffusion". In: *Biophys. J.* 73.2 (1997), pp. 1073–1080. DOI: 10.1016/S0006-3495(97)78139-6.

[32]   P. Reimann, G. J. Schmid, and P. Hänggi. "Universal equivalence of mean first-passage time and Kramers rate". In: *Phys. Rev. E. Stat. Phys. Plasmas. Fluids. Relat. Interdiscip. Topics* 60.1 (1999), R1–R4. DOI: 10.1103/PhysRevE.60.R1.

Chapter 3

Control of membrane mechanics by light-induced lipid oxidation[†]

Biological systems exhibit a variety of different lipid mixes. Locally, patches of lipids can aggregate and form patches on the membrane which have distinct properties from the rest of the membrane. We investigated the change in membrane properties during the formation of these patches by employing a novel system employing light to induce phase separation in giant unilamellar vesicles. In this process spatial and temporal fluctuations in the membrane are apparent. We show that the speed of patch generation is dependent on the amount of light. Furthermore, we show that the membrane tension drops following a power law as can be expected from a phase transition. However, it does not exhibit universal behavior.

[†]This chapter is based on: W. Pomp, M. Rinaldin and T. Schmidt "Inducing phase separation in GUV's". *In preparation.*

3.1   Introduction

Oxidation of biomolecules, and in particular lipids, plays an important role in physiology and in health. Processes associated with aging [1, 2] are largely governed by the oxidation of molecules in the cell, there is clearly documented evidence for a strong correlation between oxidation and cancer progression [3–6], and it is known that excessive oxidation will lead to cell death [7]. These correlations have also been utilized in medical therapy. Spatially controlled oxidation is used in photodynamic therapy (PDT) [8] to treat e.g. tumors of the skin. In PDT tumor tissue is covered with light-sensitive molecules, which on excitation by light produce local reactive oxygen species that oxidize molecules in their surrounding, finally leading to cell death in the tumor tissue. The molecular origin of oxidation is related to various reactive oxygen species, among which singlet oxygen ($^1O_2$) is the most prominent. The processes that drive cell death by oxidative stress are very diverse and still not conclusively understood [9, 10]. Yet, it is believed that a change of the cell membrane by reactive oxygen species is one of the aspects that will lead to cell death [11].

The membrane of a cell is a two-dimensional fluid comprised of a bilayer of a vast mixture of lipids and proteins [12–14]. Lately, it has become clear that the function of proteins is strongly modulated by their lipid environment [15, 16]. This modulation can be of pure chemical nature due to a direct interaction of the protein with a lipid or be based on the physical and mechanical properties of the cell membrane. The latter effects are associated to the rich phase-state a lipid membrane can undergo. Although still fluid, characterized by the unrestricted mobility of components, lipid membranes can assume ordering in their tail region known as liquid-ordered and liquid-disordered, two states that have very different mechanical properties. The transition temperature between states strongly depends on the lipid type and in particular on any double bonds in the acyl chains of the lipid tail. Given that the cell membrane is composed of a large variety of different lipids it is not too surprising that fluid membranes of more components display even richer behavior, including phase-separated regions and phase-boundaries with spatially inhomogeneous physical and mechanical properties [17, 18], all modulating cell behavior [19]. Diffusion of proteins might be impaired by phase borders, or some patches of lipid might have a different curvature, controlling the binding of curvature sensing proteins [20], whose affinity depends on the local curvature of the membrane. Hence, the understanding of the influence of lipid oxidation on the physical and mechanical properties of mixed membranes is important for its implication in cells, health, and disease.

To investigate the change in physical and mechanical properties of mixed membranes on controlled oxidation we imaged giant unilamellar vesicles (GUVs). For controlled oxidation, we used a molecular system in which reactive oxygen species were generated by light [1, 2, 21]. Rhodamine-labeled lipids were introduced at low concentration into the membrane of GUVs. On excitation by light, the rhodamine fluorophores generated singlet oxygen in their direct vicinity. Singlet oxygen, in turn, reacted with lipid molecules leading to local oxidation and local change in lipid and membrane properties. The latter included the formation and growth of phase-separated regions, a change in membrane surface area, and a change in membrane tension. Change in these led to dramatic shape fluctuations, the properties of which we qualitatively describe here for the first time.

3.2 Results

3.2.1 Light-induced phase separation

We prepared giant unilamellar vesicles (GUVs) from a mixture of the lipids (1-palmitoyl-2-oleoyl-*sn*-glycero-3-phosphocholine (POPC), 1,2-dioleoyl-*sn*-glycero-3-phosphoethanolamine-N-(lissamine rhodamine B sulfonyl) (DOPE-rhodamine)), sphingomyelin (SM) together with cholesterol (Chol). The mixture was chosen such that it formed a homogeneous phase within the ternary phase diagram at room temperature (figure 3.1). A low amount (5%) of rhodamine-DOPE was added to allow for observation of the GUV membrane in a fluorescence microscope. At low-light observation conditions (561 nm, $100\,W/cm^2$) the fluorescence was homogeneously distributed on the GUV membrane, the shape of which was spherical.

In order to induce reactive oxygen species, the excitation intensity was increased to $1.4\,kW/cm^2$ at activation conditions. Excitation of the rhodamine dye, transferred the dye into its excited triplet-state at small probability (1-3%) which, in sequence, leads in part to a spin exchange with a nearby oxygen molecule, and the creation of a highly reactive singlet-oxygen species ($^1O_2$). The singlet-oxygen will react with high efficiency with nearby molecules, among which lipids that contain double-bonds in their aliphatic chains [21]. Such reaction will result in a shift of the lipid shape (figure 3.2) and melting temperature, essentially moving the lipid mixture in the ternary phase diagram of the GUV to the right into the unmixing region (see arrow in figure 3.1) .
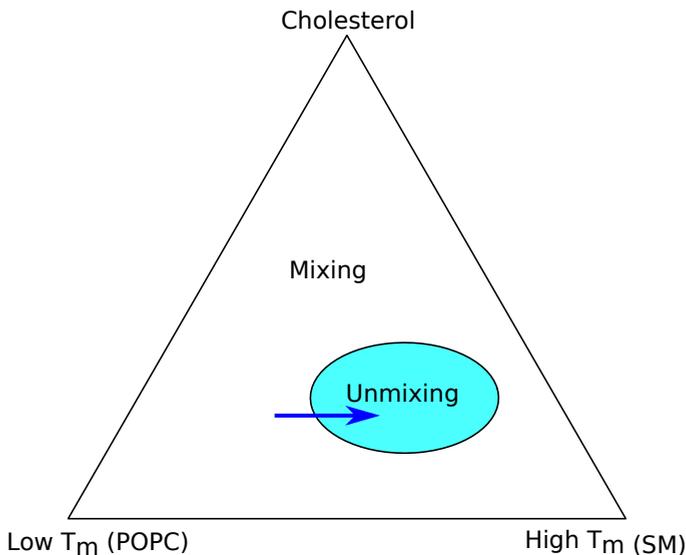
Figure 3.1: **Ternary phase diagram of a three lipid mixture.** Cholesterol and lipids of high (DOPC) and of low melting-temperature (DOPE) were mixed at a ratio that the initial composition was outside the unmixing region. On activation by light, lipids were oxidized and the mixture moved into the unmixing region.

We added a low amount ($\approx 1\%$) of rhodamine-conjugated lipids to visualize the GUV membrane in a wide-field fluorescence microscope (figure 3.3). It has been shown that rhodamine-DOPE preferentially resides in the liquid-ordered part of the membrane [17, 18], making it ideal for following phase separation to occur. We focused the microscope into the equatorial plane of the GUV. The depth-of-focus of our optical system was $\approx 1\,\mu m$, much smaller than the typical vesicle size of 20 to $50\,\mu m$. In this imaging setting, the GUV's perimeter was visible at high contrast. At the beginning of the experiment ($t = 0\,s$), the fluorescence was homogeneously distributed along the perimeter (figure 3.3 top-left), a signature of the lipid mixture to assume a single homogeneous phase. The small top-bottom gradient in fluorescence seen in figure 3.3 was due to an inhomogeneous illumination for the GUV shown. Where the fluorescence was homogeneous for the initial condition (figure 3.3 top-left) the distribution of the rhodamine-DOPE turned increasingly inhomogeneous during the experiment. This became most obvious after many (figure 3.3 bottom;
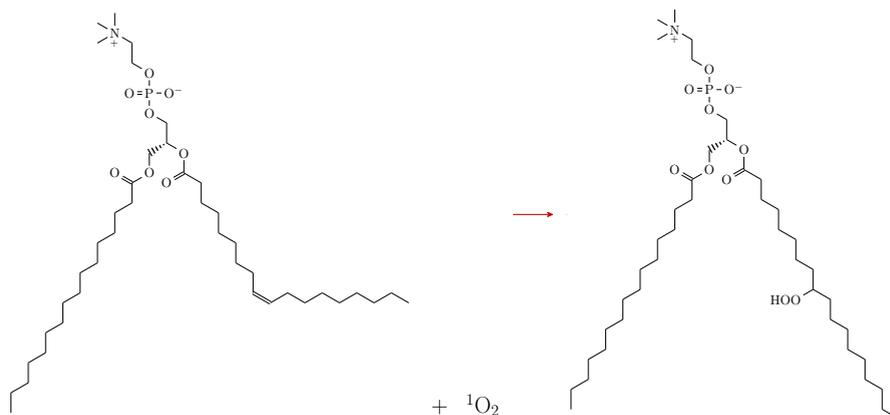
Figure 3.2: **Oxidation reaction in (1,2)-dioleoyl-*sn*-glycero-3-phosphocholine (DOPC).** Oxidation of the double-bond will lead to a change in the shape of DOPC and a larger surface area of the lipid [21].

$> 70\,\text{s}$) activation/observation cycles. Apparently, lipid oxidation drove the lipid system from the fully mixed into the unmixed region in figure 3.1, as has been reported previously [21]. Given that the rhodamine-DOPE preferentially partitions into the liquid-ordered phase [17, 18] the fluorescence on the GUV membrane became patchy.

3.2.2 Lipid oxidation and phase separation depends on fluorophore concentration and illumination intensity

The observed patchiness was further used to quantify the rate of photoconversion and for the characterization of its molecular origin. Phase separation into liquid-ordered and liquid-disordered membrane domains became visible when the fluorescent lipids started to be confined in liquid-ordered patches of a size larger than the diffraction limit ($\approx 300\,\text{nm}$). For quantification, we analyzed the fluorophore distribution along the perimeter of the GUV by means of the pixel brightness. This analysis allowed us to obtain the line profile which, when phase separation occurred, showed defined maxima at the locations where liquid-ordered patches appeared. For the vesicle shown in figure 3.3, after a lag-time of $20s$, the number of patches steadily grew at a rate of $(0.116 \pm 0.005)/\text{s}$
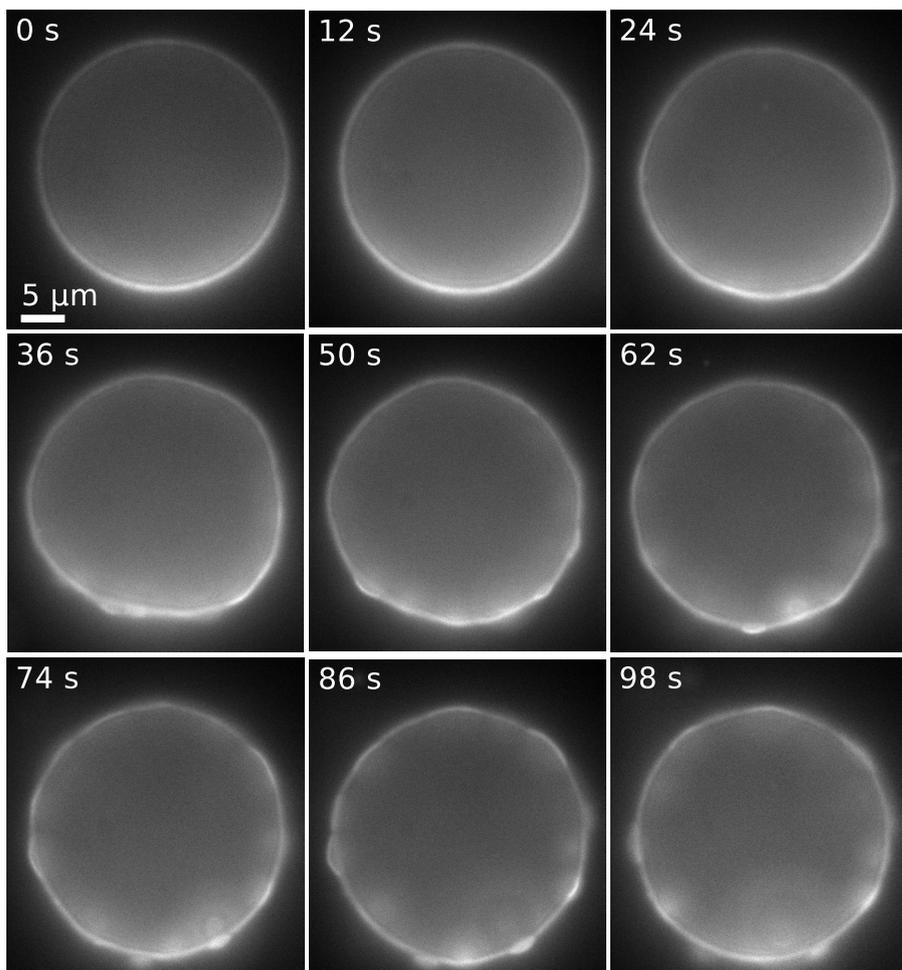
Figure 3.3: **Phase separation in a GUV followed by fluorescence microscopy.** At $t = 0\,$s, the fluorescence was homogeneouly distributed along the GUV perimeter. After a few seconds the GUV membrane started to deform. After about $20\,$s lipids started to segregate into patches. After about $40\,$s the patches formed buds.

(figure 3.4). It should be noted that the initial lag-time was not controlled, given that it was impossible to prepare all vesicles at the exact same location in the ternary phase diagram. Hence, for every vesicle, the distance to the unmixing region varied, and with that, the time at which phase separation started in our experiments. Analogous to the number of patches, the fraction of the perimeter that was covered by the liquid-disordered domain increased with time. Between 20 and 100s it increased towards 40%. In this range the conversion followed a linear relation at a constant rate of $(5.4 \pm 0.2) \cdot 10^{-3}/$s (figure 3.5). Because only part of the time the GUV is illuminated, these numbers in terms of illumination time are $(11.6 \pm 0.5)/$s and $(5.4 \pm 0.2) \cdot 10^{-1}/$s respectively.
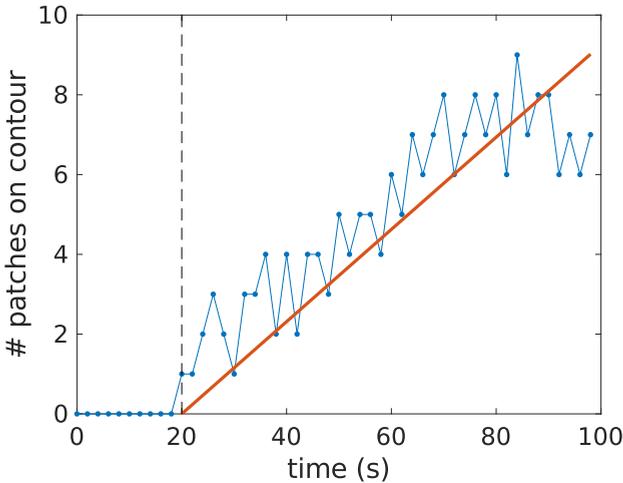
Figure 3.4: **Number of patches visible on the perimeter of a GUV.** The number grows after an initial lag-phase (black, dashed line) at constant rate of $(0.116 \pm 0.005)/$s.

The rate of lipid oxidation could be predicted, provided one knew all photophysical and photochemical rate constants [22]. Following the reaction scheme described in section 3.2.1, the rate R, at which the liquid-orderd phase will grow is expressed by:

$$R(c, I, \lambda) = c \times \alpha(\lambda) \times I(\lambda) \ \times \ \eta_{\text{ST}} \times \eta_{\text{TT}} \times \eta_{\text{chem}} \tag{3.1}$$
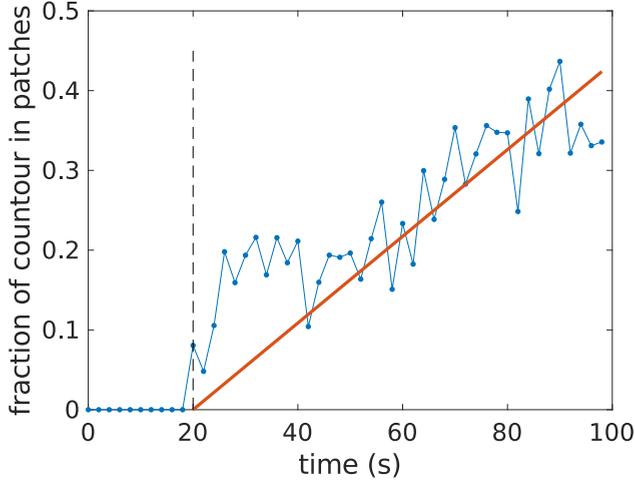
Figure 3.5: **Fraction of the contour which is in the liquid-ordered patch.** After an initial lag-phase (black, dashed line), the total area fraction grows at a constant rate of $(5.4 \pm 0.2) \cdot 10^{-3}/\text{s}$.

This rate depends on the concentration of the rhodamine dye (c), the absorption cross section of the dye at the excitation wavelength ($\alpha(561\,\text{nm}) = 2.9 \cdot 10^{-7}/\text{cm}^2$), the illumination intensity ($I(561\,\text{nm}) = 100\,\text{W}/\text{cm}^2$), the intersystem crossing yield of rhodamine ($\eta_{\text{ST}} = 1\text{--}2\%$), and the two largely unknown parameters for the triplet-triplet transfer towards oxygen (η_{TT}) and the chemical reaction efficiency of acyl-chain oxidation (η_{chem}). Yet it is obvious from equation (3.1) that $R(c, I, \lambda)$ is proportional to $c \times \alpha(\lambda) \times I(\lambda)$, which is proportional to the detected brightness in the image. Our prediction was confirmed in experiments. Various vesicle preparations were made in which the dye concentration and the illumination intensity was varied. The average brightness was compared to the rates of the fractional domain growth as displayed for one GUV in figure 3.5. The data are shown in figure 3.6 for a range in brightness between $1\text{--}9 \cdot 10^5$ counts per pixel. The behavior was linear, characterized by a slope of $(4.00 \pm 0.35) \cdot 10^{-6}$.
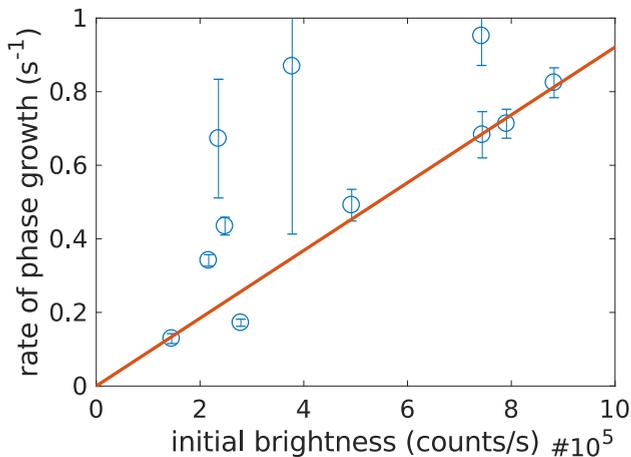
Figure 3.6: **Rate of phase growth,** expressed as a fraction of the visible contour, plotted versus the average brightness (counts/s) of the edge of the GUV in the first recorded frame. A good linear correlation through the origin exists, and the slope of the line is $(9 \pm 4) \cdot 10^{-7}$.

3.2.3 Light-induced shape fluctuations

A further, so far unnoticed observation we made in our experiments was the development of dramatic shape fluctuation that occurred before membrane domains became visible (see figure 3.3). At the beginning of the experiment ($t = 0s$) shown in figure 3.3 the GUV assumed a perfect circular shape. As the vesicle was illuminated, spatial and temporal fluctuations started to appear already after $12\,\text{s}$ which further evolved until at $74\,\text{s}$ a steady shape was obtained in which stable liquid-ordered domains are clearly visible that bulge out from the vesicle.

Those membrane fluctuations we in part attribute to an increase in surface area of the GUV membrane due to the different molecular shape of the converted lipids (figure 3.2). However, lipid conversion might further lead to a change in the mechanical properties of the membrane, and to a change in the spontaneous curvature [1, 2], both of which might contribute to the observed fluctuations. A general mechanical description of the mechanical properties of vesicles is obtained by the Helfrich Hamiltonian [23]:

$$H_{\text{shape}} = \int_A \mathrm{d}A \; \frac{\kappa_{\text{b}}}{2} \left(C_1 + C_2 - C_0\right)^2 \; + \; \int_A \mathrm{d}A \; \sigma \qquad (3.2)$$

The stored mechanical energy in the vesicle depends on its local bending rigidity, κ_{b}, its local curvatures, C_1 and C_2, on the spontaneous curvature due to the shape of the lipids C_0, and on the membrane tension σ. Additional terms in this Hamiltonian like the Gaussian curvature, an area-difference term, and the osmotic pressure were neglected in eq. 3.2 as they were constant in our experiments. At equilibrium, the vesicle will assume a shape of minimal energy [23]. Creation of excess membrane area will hence lead to a change in vesicle shape and to fluctuations around its equilibrium configuration.

3.2.4   Sub-diffraction tracking of the GUV perimeter

To quantify our observations we set out to precisely determine the position of the GUV membrane to sub-diffraction accuracy (see also section 3.4). We first determined the GUV center and its mean radius R (green circle in figure 3.7). Subsequently, closely-spaced radial sections were calculated from which the position of the membrane was extrapolated by Gaussian fitting (inset to figure 3.7). The large signal of the rhodamine-dye ($S = 1000$ counts) allowed us to determine the position of the GUV membrane to about $20\,\text{nm}$. This precision was predicted using arguments from super-resolution microscopy [24], from which the accuracy was estimated to be $\Delta x = \Gamma_{\text{PSF}}/\sqrt{s}$ ($\Gamma_{\text{PSF}} \approx 300\,\text{nm}$, width of the point-spread function). The red line in fig. 3.7 shows the location of the GUV membrane as determined in this way.

In figure 3.8 the deviation u of the GUV membrane from an ideal circle is shown as it varies along the perimeter. Just before phase separation occurred, these fluctuations were easily identified. u fluctuates on the length scale of $30\,\mu\text{m}$ for up to almost one μm from the ideal circle describing the GUV. Over the time-course of the experiment, we quantified the size of these fluctuations by calculating the standard deviation of u averaged over the whole GUV perimeter. Figure 3.9 shows how $\text{STD}(u)$ changes with time between start
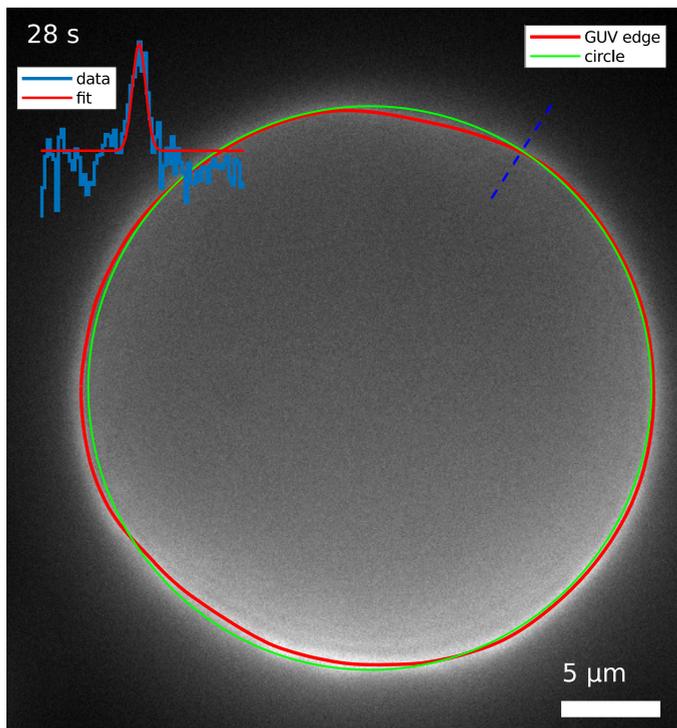
Figure 3.7: **Image of a GUV exhibiting membrane fluctuations.** The image was taken close to the time when phase separation occurred. The green circle is an ideal circle coinciding with the edge of the GUV. The red line shows the real position of the GUV membrane as determined by fitting Gaussian profiles to radial profiles. The inset in the top-left shows a Gaussian fit for one profile. Pixel values are shown in blue, the Gaussian fit is shown in red.

of the experiment and up to $100\,\mathrm{s}$ later. Before phase separation becomes visible ($t < 20\,\mathrm{s}$), $\mathrm{STD}(u) = 0.3\,\mu\mathrm{m}$, which in turn doubled to $0.6\,\mu\mathrm{m}$ at $60\,\mathrm{s}$. After phase separation was stable, the fluctuations dropped at $70\,\mathrm{s}$ to less than $0.2\,\mu\mathrm{m}$. For even longer timescales, the membrane formed buds to which our analysis did not apply, and results were not further followed.
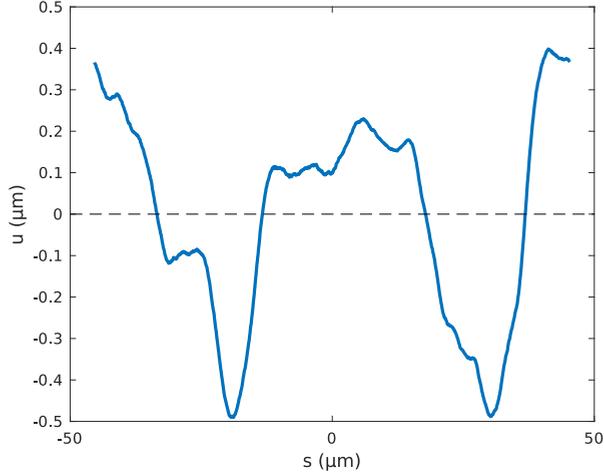
Figure 3.8: **Deviation u of the GUV membrane position from an ideal circle** at positions $s = \theta R$. In this example the difference between biggest and smallest radius is almost 1 μm.

3.2.5   Mechanical properties of the membrane througout phase separation

Fluctuations are closely related to the mechanical properties of membranes [23, 25, 26]. The mechanical properties are characterized by the bending modulus κ_{b}, and the membrane tension σ (see equation (3.2)). Both we extracted from the fluctuation spectrum [26, 27] determined from the real-space fluctuations along the vesicle perimeter (figure 3.8). The fluctuation spectral density for the data in figure 3.7 is shown in figure 3.10. Following the description developed by Pecreaux, the power spectral density is given by [26, 27]:

$$\langle |u_{\mathrm{k}}|^2 \rangle = \frac{1}{2\pi R} \; \frac{k_{\mathrm{B}}T}{\sigma q^2 + \kappa_{\mathrm{b}}q^4} \tag{3.3}$$

A fit of the spectral data to equation (3.3) is shown in figure 3.10 (red line). The fit yielded values for the bending modulus $\kappa_{\mathrm{b}} = (1.0 \pm 0.7) \cdot 10^{-19}$ J and for the membrane tension $\sigma = (2.5 \pm 0.3) \cdot 10^{-5}$ N/m^2. Both values corroborate values reported earlier [26, 27].
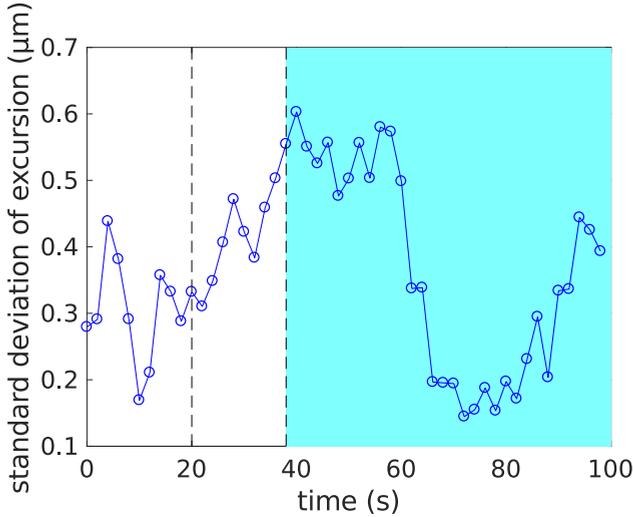
Figure 3.9: **Membrane fluctuations as a function of time.** The size of the fluctuations we characterized for each frame by calculating the standard deviation of u as shown in figure 3.8. The region before the first dashed line indicates the lag-phase. The blue region after the second dashed line indicates the time when budded patches appear in stead of pure fluctuations.

We anticipated that the bending modulus would not change when phase separation was induced, given that the bending modulus is a material property, depending on the composition of the membrane which only marginally changed throughout the experiment. This hypothesis was confirmed, within experimental uncertainty, by our experiments (figure 3.11). This finding was further confirmed by the analysis of all GUVs. The probability density function for the bending modulus for an ensemble of all data is shown in figure 3.12. The distribution was narrowly peaked at a most probable value of $\langle \kappa_{\mathrm{b}} \rangle = (1.0 \pm 0.3) \cdot 10^{-19}$ J.

From our chemical model described earlier, which assumed that photo-oxidation leads to a change in lipid structure and a concurrent increase in membrane area, we predicted that surface tension, in contrast to bending modulus, would change during the observation time. For a perfectly spherical GUV, the volume-to-surface ratio is $R/3$. On the appearance of membrane fluctuations, this ratio becomes smaller and consequently membrane tension will decrease. This prediction was confirmed by our experiments (figure 3.13).
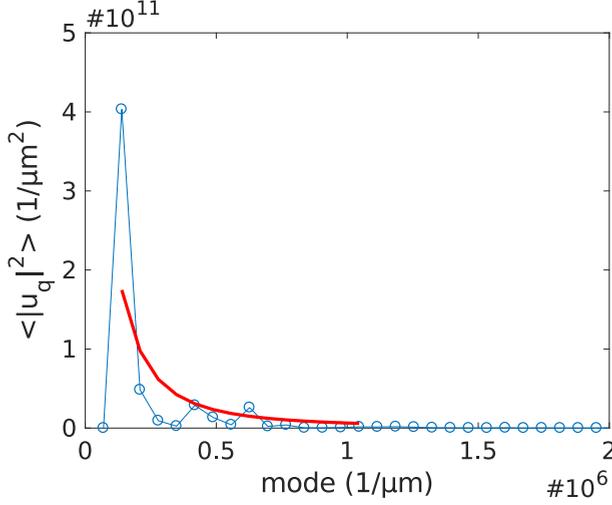
Figure 3.10: **Power spectral density of membrane fluctuations as a function of the mode** q**.** The spectrum is fitted to equation (3.3) as described in [26, 27], yielding the bending modulus $\kappa_b = (1.0 \pm 0.7) \cdot 10^{-19}$ J and membrane tension $\sigma = (2.50 \pm 0.28) \cdot 10^{-5}$ N/m^2.

Before the phase separation was visible ($t < 20$ s), σ was constant with $\sigma = \sigma_0 = (3.0 \pm 0.8) \cdot 10^{-5}$ N/m. On emergence of the phase transition the surface tension dropped to $\sigma = 1.3 \cdot 10^{-6}$ N/m. After that, phase separation was stable and clear bulged-out domains were visible ($t > 70$ s), the simple description for a vesicle as a homogeneous spherical object (equation (3.2)) clearly failed. Hence data beyond that time were further neglected. From all our measurements the distribution in initial surface tension σ_0 is shown in figure 3.14. The distribution is narrowly peaked at the most probable value of $\langle \sigma_0 \rangle = (3.3 \pm 0.3) \cdot 10^{-5}$ N/m^2.
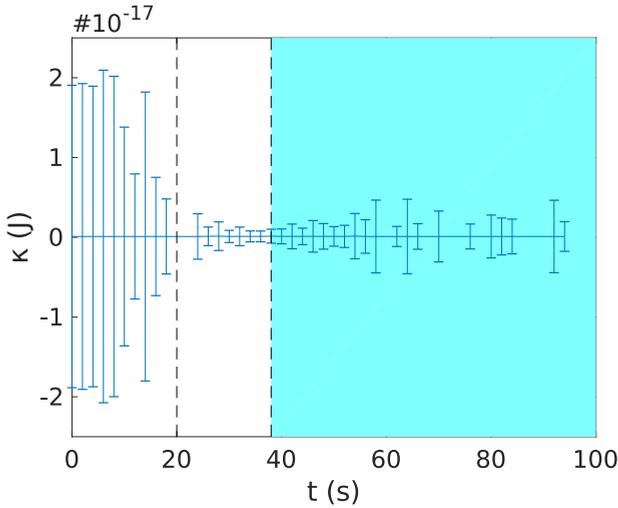
Figure 3.11: **Bending rigidity as a function of time.** During the experiment the bending rigidity did not change within experimental accuracy, and is constant around $\kappa_b = (1.1 \pm 0.1) \cdot 10^{-19}$ J.

3.3   Discussion & Conclusion

Here we investigated the physical and mechanical characteristics of phospholipid membranes when driven into a state where phase-separation occurred. Photooxidation helped us to modify the lipid composition in a gentle and controlled way. Our data on the process of photooxidation are commensurate with earlier results [1, 2, 21]: the process is based on the presence of a photosensitizer and is likely governed by the creation of a reactive oxygen species, which in turn leads to an oxidation of lipid molecules. As reported in those earlier studies, photooxidation results in an increase of surface area which has implications on vesicle stability [2] and vesicle mechanics.

While the change in lipid composition did not change the rigidity of the membrane towards bending, the membrane tension became significantly reduced. Concurrent with the reduction in membrane tension, large shape fluctuations and a separation into liquid-ordered and liquid-disordered domains occurred. We questioned whether such behavior would resemble signatures of a phase transition. With the time of experimentation, the density of high-T_m components increase, i.e. their average distance would decrease quadratically. In
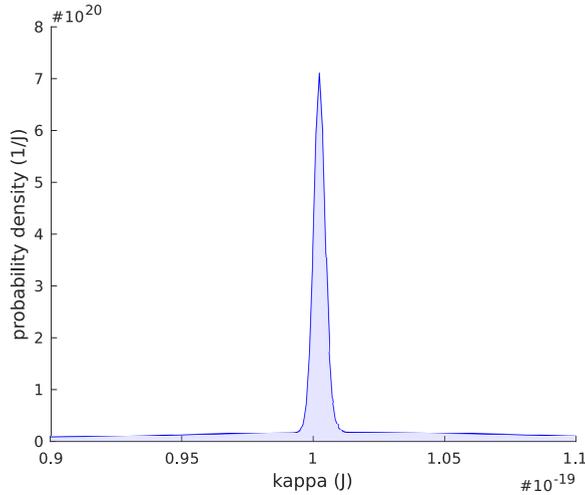
Figure 3.12: **Ensemble probability-density of membrane bending modulus.** The most probable modulus for all experiments was $\langle \kappa_b \rangle = (1.0 \pm 0.3) \cdot 10^{-19}$ J.

terms of an Ising model, this could be interpreted as a slow increase in average interaction between the high-T_m components. Concurrent with this hypothesis would be the observation of a power-law dependence of the membrane tension with time, equivalent to the interaction strength. Indeed we confirmed that hypothesis in our experiments. After the initial part in experimentation displayed in figure 3.13, the membrane tension followed a power-law dependence with an exponent of 0.99 ± 0.04. A further signature for the process being governed by a phase transition would be a universal, i.e. narrow-peaked distribution in the exponent for an ensemble of realizations. In figure 3.15, the probability density distribution of the measured exponents is shown. Although, the number of realizations was fairly small (N=9), the wide spread of the power-law dependence did not support the initial hypothesis of the observed process being covered by a phase transition of a given universality class.
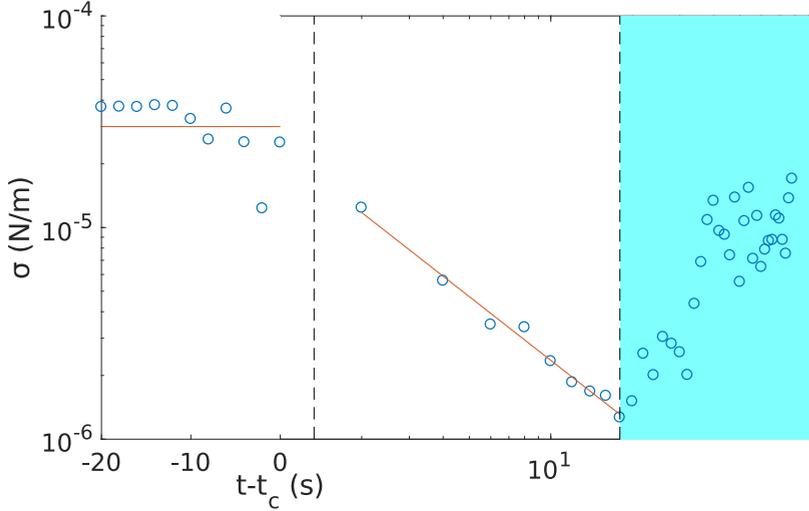
Figure 3.13: **Membrane tension σ as function of time.** An onset of fluctuations was observed at $t_c = 20\,\mathrm{s}$ (first dashed vertical line). Before that time, the membrane tension was constant. After the onset of fluctuations, the membrane tension dropped, following a power-law behavior characterized by an exponent of -0.99 ± 0.04). When membrane patches start to evolve (second vertical line), further analysis by the simple model breaks down.

In our hypothesis, we assumed that the change in lipid composition is very slow, such that the lipid system is at equilibrium any time. In case this assumption fails, a dynamic model would apply that involves the transfer of components as well as processes for nucleation and domain growth. Which of the different models appropriately could explain our observations, hence cannot be discerned so far, and will need additional experimental evidence.

Nonetheless, we clearly demonstrated the effects of lipid oxidation on the phase behavior and the mechanical characteristics of biological membranes. Undisputedly lipid oxidation will also occur in cells, hence all the described processes will play a role. A decrease in membrane tension means that it is easier to bend the membrane. Thereby, the affinity of curvature sensing proteins can change and trigger a biological function. Cells will react on those challenges with an active exchange of lipids but also by active modulation of
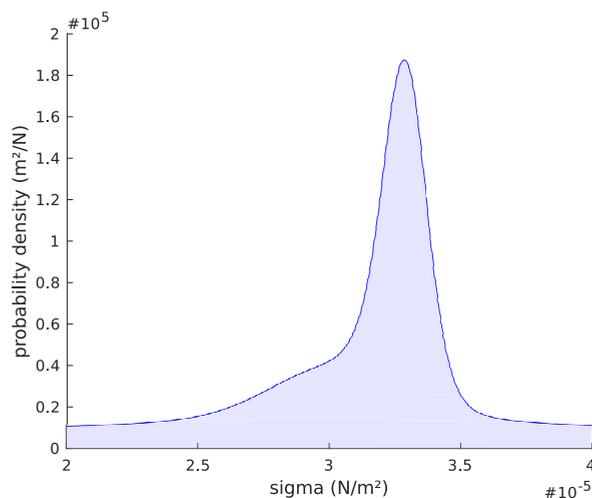
Figure 3.14: **Distribution of the initial membrane tension in all experiments.** The distribution is peaked at its most probable value of $\langle \sigma_0 \rangle = (3.3 \pm 0.3) \cdot 10^{-5} \, \mathrm{N/m^2}$.

membrane area by endo- and exocytosis. Given that those reaction mechanisms fail, cells would be driven into apoptosis, a program one tries to locally initialize in photodynamic therapy. A more dramatic effect of the enhanced membrane fluctuations would be direct cell rupture, a process which so-far has been discussed to describe the effect of photodynamic therapy, but which probably is too easy to explain the therapeutic outcome. Yet, it is interesting to note that membrane fluctuations and the parallel dramatic decrease in membrane tension might be an interesting route to follow in the current strive to built up artificial cell-like systems to mimic cell division.
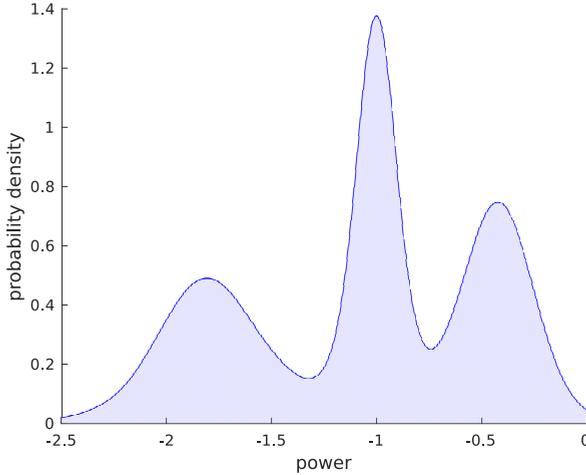
Figure 3.15: **Distribution of powers measured from the drop in membrane tension during the time of fluctuations.** While the drop shows powerlaw behavior, the powers are not unversal.

3.4 Materials and Methods

3.4.1 GUV preparation

Giant unilamellar vesicles (GUVs) were prepared using electroswelling [28]. 20 µl lipids (1-palmitoyl-2-oleoyl-*sn*-glycero-3-phosphocholine (Avanti Polar Lipids 850457C, POPC), 1,2-dioleoyl-*sn*-glycero-3-phosphoethanolamine-N-(lissamine rhodamine B sulfonyl) (Avanti Polar Lipids 810150C, DOPE-rhodamine)), sphingomyelin (Avanti Polar Lipids 860062C, Brain SM) together with cholesterol (Avanti Polar Lipids 700100P, cholesterol (plant)) dissolved in chloroform (2 g/L) were deposited on top of two indium tin oxide (ITO) coated glasses (total covered area about 10 cm^2). The chloroform was evaporated for two hours using a desiccator. Subsequently the coated glasses were placed parallel, coated sides facing each other in a teflon enclosure with about 3 mm separation between them. The space between the glasses was filled with 230 mOsmol/kg sucrose. Swelling was done for two hours at 10 Hz, 4 V$_{pp}$ sinusoidal excitation. After that the sucrose solution containing the GUVs was extracted from the chamber.

3.4.2 Imaging

Imaging was performed on an epi-fluorescence microscope. Illumination was performed using a 488 nm, 100 mW laser (Coherent Sapphire 488-100 CW CDRH). The laser beam was modulated by an acousto-optical tunable filter (AA-OptoElectronic, AOTFnC-VIS) to illuminate the sample only when the camera was in exposure mode. Via a tube-lens, the laser beam was coupled into a Zeiss Axiovert 100 microscope fitted with a Zeiss 100× NA 1.4 oil immersion objective resulting in Köhler illumination of the sample. The excitation and emission paths were split using a dichroic mirror (Semrock Di01-R405/488/561/635) and an emission filter (Chroma ZET405/488/561/640m). Detection was done using a CCD camera (Roper Scientific/Princeton Instruments 1340B combined with an ST133 controller and WinView32 software), cooled to $-90\,°C$ using liquid nitrogen.

3.4.3 Image Analysis

To quantify our observations we set out to precisely determine the position of the membrane of the GUV to sub-diffraction accuracy. To do this, we first determined the center position and the mean radius R of the GUV (green circle in figure 3.7). After subtraction of background by means of a spatial lowpass filter, the image of the GUV was thresholded such that pixels on the edge of the GUV were separated from the pixels outside. The locations of these pixels were subsequently used to determine the radius and center coordinates of the GUV. The GUV is then sliced into slices with an angle $\Delta\theta = 1/2R_{px}$ with R_{px} the radius of the GUV measured in pixels. Now, under every radial, starting from $0.8R$ and extending to $1.25R$, one of which is shown as a blue dashed line in figure 3.7, the pixel values are fitted to a Gaussian profile. The inset in figure 3.7 shows this, with, in blue the pixel values measured, and in red the fit to them. This allows us to determine the location of the edge of the GUV with subpixel accuracy (down to about 20 nm). The red line in figure 3.7 shows the location of the edge of the GUV in the image, determined in this way. In figure 3.8 the deviation u of the edge of the GUV from the mean is shown. Just before phase separation occurs, these fluctuations can be seen visually, and the membrane can deviate up to a µm from the mean radius of the GUV. Over the course of the experiment, we quantified the size of these fluctuations by taking the standard deviation of u. Figure 3.9 shows that before phase separation happens, the GUV already exhibits fluctuations for some time. After phase separation, the fluctuations diminish and only express the height of the phase separated buds budding out from the surface.

References

[1] J. Heuvingh and S. S. Bonneau. "Asymmetric oxidation of giant vesicles triggers curvature-associated shape transition and permeabilization". In: *Biophys. J.* 97.11 (2009), pp. 2904–2912. DOI: 10.1016/j.bpj.2009.08.056.

[2] K. A. Riske et al. "Giant vesicles under oxidative stress induced by a membrane-anchored photosensitizer". In: *Biophys. J.* 97.5 (2009), pp. 1362–1370. DOI: 10.1016/j.bpj.2009.06.023.

[3] S. Reuter et al. "Oxidative stress, inflammation, and cancer: How are they linked?" In: *Free Radic. Biol. Med.* 49.11 (2010), pp. 1603–1616. DOI: 10.1016/j.freeradbiomed.2010.09.006.

[4] G. Waris and H. Ahsan. "Reactive oxygen species: role in the development of cancer and various chronic conditions". In: *J. Carcinog.* 5.14 (2006), pp. 1–8. DOI: 10.1186/1477-3163-5-14.

[5] A. Jezierska-Drutel, S. A. Rosenzweig, and C. A. Neumann. "Role of oxidative stress and the microenvironment in breast cancer development and progression". In: *Adv. Cancer Res.* Vol. 119. 2013, pp. 107–125. DOI: 10.1016/B978-0-12-407190-2.00003-4.

[6] T. D. Oberley. "Oxidative damage and cancer". In: *Am. J. Pathol.* 160.2 (2002), pp. 403–408. DOI: 10.1016/S0002-9440(10)64857-2.

[7] G. Filomeni et al. "Oxidative stress and autophagy: the clash between damage and metabolic needs". In: *Cell Death Differ.* 22.3 (2015), pp. 377–388. DOI: 10.1038/cdd.2014.150.

[8] D. E. Dolmans, D. Fukumura, and R. K. Jain. "Timeline: Photodynamic therapy for cancer". In: *Nat. Rev. Cancer* 3.5 (2003), pp. 380–387. DOI: 10.1038/nrc1071.

[9] W. Fiers et al. "More than one way to die: apoptosis, necrosis and reactive oxygen damage". In: *Oncogene* 18 (1999), pp. 7719–7730. DOI: 10.1038/sj.onc.1203249.

[10] R. C. Taylor, S. P. Cullen, and S. J. Martin. "Apoptosis: controlled demolition at the cellular level". In: *Nat. Rev. Mol. Cell Biol.* 9.3 (2008), pp. 231–241. DOI: 10.1038/nrm2312.

[11] A. Easterling et al. "A scanning electron microscopic study of the chick chorioallantoic membrane: cell death and the involvement of oxygen free radicals". In: *Scanning Microsc.* 7.1 (1993), pp. 87–96.

[12]   S. J. Singer and G. L. Nicolson. "The fluid mosaic model of the structure of cell membranes". In: *Science* 175.4023 (1972), pp. 720–731. DOI: `10.1126/science.175.4023.720`.

[13]   D. G. Ackerman and G. W. Feigenson. "Lipid bilayers: clusters, domains and phases". In: *Essays Biochem.* 57 (2015), pp. 33–42. DOI: `10.1042/bse0570033`.

[14]   E. Sezgin et al. "The mystery of membrane organization: composition, regulation and roles of lipid rafts". In: *Nat. Rev. Mol. Cell Biol.* 18.6 (2017), pp. 361–374. DOI: `10.1038/nrm.2017.16`.

[15]   F. X. Contreras, A. M. Ernst, and F. Wieland. "Specificity of intramembrane protein – lipid Interactions". In: *Cold Spring Harb. Perspect. Biol.* 3.6 (2011), pp. 1–19. DOI: `10.1101/cshperspect.a004705`.

[16]   A. W. Smith. "Lipid-protein interactions in biological membranes: A dynamic perspective". In: *Biochim. Biophys. Acta - Biomembr.* 1818.2 (2012), pp. 172–177. DOI: `10.1016/j.bbamem.2011.06.015`.

[17]   J. Korlach et al. "Characterization of lipid bilayer phases by confocal microscopy and fluorescence correlation spectroscopy". In: *Proc. Natl. Acad. Sci.* 96.15 (1999), pp. 8461–8466. DOI: `10.1073/pnas.96.15.8461`.

[18]   T. Baumgart, S. T. Hess, and W. W. Webb. "Imaging coexisting fluid domains in biomembrane models coupling curvature and line tension". In: *Nature* 425.October (2003), pp. 821–824. DOI: `10.1038/nature02013`.

[19]   K. Simons and E. Ikonen. "Functional rafts in cell membranes". In: *Nature* 387.6633 (1997), pp. 569–72. DOI: `10.1038/42408`.

[20]   C. Prévost et al. "IRSp53 senses negative membrane curvature and phase separates along membrane tubules". In: *Nat. Commun.* 6 (2015), p. 8529. DOI: `10.1038/ncomms9529`.

[21]   C. K. Haluska et al. "Photo-activated phase separation in giant vesicles made from different lipid mixtures". In: *Biochim. Biophys. Acta - Biomembr.* 1818.3 (2012), pp. 666–672. DOI: `10.1016/j.bbamem.2011.11.025`.

[22]   N. Busch, M. Yarmush, and M. Toner. "A theoretical formalism for aggregation of peroxidized lipids and plasma membrane stability during photolysis". In: *Biophys. J.* 75.6 (1998), pp. 2956–2970. DOI: `10.1016/S0006-3495(98)77737-9`.

[23]   W. Helfrich. "Lipid bilayer spheres: Deformation and birefringence in magnetic fields". In: *Phys. Lett. A* 43.5 (1973), pp. 409–410. DOI: `10.1016/0375-9601(73)90396-4`.

[24]   N. Bobroff. "Position measurement with a resolution and noise-limited instrument". In: *Rev. Sci. Instrum.* 57.6 (1986), pp. 1152–1157. DOI: 10.1063/1.1138619.

[25]   U. Seifert. "Configurations of fluid membranes and vesicles". In: *Adv. Phys.* 46.1 (1997), pp. 13–137. DOI: 10.1080/00018739700101488.

[26]   J. Pécréaux et al. "Refined contour analysis of giant unilamellar vesicles". In: *Eur. Phys. J. E - Soft Matter* 13.3 (2004), pp. 277–290. DOI: 10.1140/epje/i2004-10001-9.

[27]   S. Semrau et al. "Accurate determination of elastic parameters for multicomponent membranes". In: *Phys. Rev. Lett.* 100.8 (2008), p. 088101. DOI: 10.1103/PhysRevLett.100.088101.

[28]   M. I. Angelova and D. S. Dimitrov. "Liposome electroformation". In: *Faraday Discuss. Chem. Soc.* 81 (1986), pp. 303–311. DOI: 10.1039/dc9868100303.

Chapter 4

Cytoskeletal anisotropy controls geometry and forces of adherent cells[†]

We introduce a simple mechanical model for adherent cells that quantitatively relates cell shape, internal cell stresses and traction forces as generated by an anisotropic cytoskeleton. Using a combination of analytic work and experiments on micropillar arrays, we demonstrate that the shape of the cell edge is accurately described by elliptical arcs, whose eccentricity expresses the degree of anisotropy of the internal cell stresses. Our work highlights the strong interplay between cell mechanics and geometry and paves the way towards the reconstruction of cellular forces from geometrical data.

4.1   Introduction

Cell behavior and fate crucially depend on mechanical cues from outside the cell [1–5]. Examples include rigidity-dependent stem cell differentiation [6, 7], protein expression regulated by internal stresses [8], and durotaxis [9, 10]. Whether at rest on a substrate [11] or migrating [12, 13], cells rely on their shape to gauge the mechanical properties of their microenvironment [14] and control the traction force exerted on their surroundings. The physical mechanisms behind these spectacular forms of bio-mechanical adaptation are, however, poorly understood.

Many animal cells spread and develop transmembrane adhesion receptors when coming into contact with an adhesive substrate. This induces the actin cytoskeleton to reorganize into cross-linked networks and bundles (i.e. stress fibers), whereas adhesion becomes limited to a number of sites, distributed mainly along the cell contour (i.e. focal adhesions). At this stage, cells are essentially flat and assume a typical shape characterized by arcs which span between the sites of adhesion, while forces are mainly contractile [15]. On timescales much shorter than those required by a cell to change its shape (i.e. minutes), the cell is in mechanical equilibrium at any point of its interface.

4.2   Model

We model adherent cells as two-dimensional contractile films [16], and we focus on the shape of the cell edge connecting two consecutive adhesion sites. Mechanical equilibrium requires the difference between the internal and external stresses acting on the cell edge to balance the contractile forces arising in the cortex:

$$\frac{\mathrm{d}\boldsymbol{F_{\mathbf{cortex}}}}{\mathrm{d}s} + (\hat{\boldsymbol{\Sigma}}_{\mathrm{out}} - \hat{\boldsymbol{\Sigma}}_{\mathrm{in}}) \cdot \boldsymbol{N} = \boldsymbol{0} \; . \tag{4.1}$$

Here $\hat{\boldsymbol{\Sigma}}_{\mathrm{out}}$ and $\hat{\boldsymbol{\Sigma}}_{\mathrm{in}}$ are the stress tensors outside and inside the cell and $\boldsymbol{F}_{\mathrm{cortex}}$ is the stress resultant along the cell cortex. The latter is parametrized as a one-dimensional curve spanned by the arc-length s and oriented along the inward pointing normal vector $\boldsymbol{N}$. A successful approach, initially proposed by Bar-Ziv *et al.* in the context of cell pearling [17] and later expanded by Bischofs *et al.* [11, 18], consists of modelling bulk contractility in terms of an isotropic pressure $\hat{\boldsymbol{\Sigma}}_{\mathrm{out}} - \hat{\boldsymbol{\Sigma}}_{\mathrm{in}} = \sigma\hat{\boldsymbol{I}}$, with $\hat{\boldsymbol{I}}$ the identity matrix, and peripheral contractility as an interfacial tension of the form $\boldsymbol{F}_{\mathrm{cortex}} = \lambda\boldsymbol{T}$, with $\boldsymbol{T}$ a unit vector tangent to the cell edge. The quantities σ and λ are material constants that embody the biomechanical activity of myosin motors in the

actin cytoskeleton. This competition between bulk and peripheral contractility along the cell boundary results in the formation of arcs of constant curvature $1/R = \sigma/\lambda$, through a mechanism analogous to the Young-Laplace law for fluid interfaces. The shape of the cell boundary is then approximated by a sequence of circular arcs, whose radius R might or might not be uniform across the cell, depending on how the cortical tension λ varies from arc to arc. The case of shape-dependent λ values was elaborated by Bischofs *et al* [11, 18] to account for an apparent correlation between the curvature and length of the cellular arcs. Both models successfully describe the geometry of adherent cells in the presence of strictly isotropic forces.
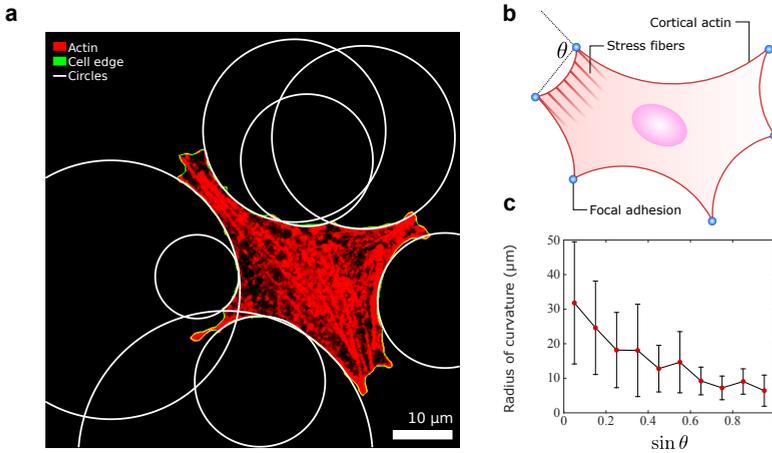
Figure 4.1: **Relation between stress fibres and curvature of the cell edge. a** A cell with an anisotropic actin cytoskeleton (epithelioid GEβ3) with circles (white) fitted to its edges (green). The actin cytoskeleton is visualised with TRITC-Phalloidin (red). Scalebar is 10 μm. **b** The cell cortex (red line) is spanned in segments between fixed adhesion sites (blue). The line through two adhesion sites makes an angle θ with the stress fibres inside the cell. **c** Arc radius as a function of $\sin\theta$ (data show the mean $\pm$ standard deviation).

4.3   The actin cytoskeleton is anisotropic

Yet many cells, including the fibroblastoids (GDβ1, GDβ3) and epithelioids (GEβ1, GEβ3) studied here (figure 4.1a) [19], develop directed forces by virtue of the strong anisotropic cytoskeleton originating from the actin stress fibers [20, 21]. This scenario is, evidently, beyond the scope of models based on isotropic contractility. Indeed, while the shape of the cell edges in Fig. 1a can still be approximated by circular arcs, the large variance in the distribution of R appears unjustified, as it would imply large variations in the cortical tension λ. Furthermore, a survey of a sample of 285 cells did not reveal a correlation between the length and the radius of the circular arcs, as predicted by the tension-elasticity model discussed by Bischofs et al [11, 18]. On the other hand, our data show a prominent correlation between the radius of curvature of the cellular arcs and their angle θ with respect to the local orientation of stress fibers (figure 4.1b). In particular, the radius of curvature decreases as the stress fibers become more perpendicular to the cell cortex (figure 4.1c). This correlation is intuitive as the bulk contractile stress focusses in the direction of the stress fibers.

The anisotropy of the actin cytoskeleton can be incorporated into the mechanical framework summarised by equation (4.1), by modelling the stress fibres as contractile force-dipoles. This collectively gives rise to a directed contractile bulk stress, namely $\hat{\boldsymbol{\Sigma}}_{\text{out}} - \hat{\boldsymbol{\Sigma}}_{\text{in}} = \sigma\hat{\boldsymbol{I}} + \alpha\boldsymbol{nn}$ [22, 23], with $\alpha > 0$ the magnitude of the directed contractile stress and $\boldsymbol{n}$ the average direction of the stress fibres. The ratio between isotropic contractility σ and directed contractility α measures the degree of anisotropy of the bulk stress. With this stress tensor the force balance equation (4.1) becomes:

$$\frac{\mathrm{d}\lambda}{\mathrm{d}s}\,\boldsymbol{T} + (\lambda\kappa + \sigma)\boldsymbol{N} + \alpha(\boldsymbol{n}\cdot\boldsymbol{N})\boldsymbol{n} = \boldsymbol{0}\ , \tag{4.2}$$

where we used $\mathrm{d}\boldsymbol{T}/\mathrm{d}s = \kappa\boldsymbol{N}$, with κ the curvature of the cell edge. This implies that, in the presence of an anisotropic cytoskeleton, the cortical tension λ is no longer constant along the cell cortex, as long as the directed stress has a non-vanishing tangential component (i.e. $\boldsymbol{n}\cdot\boldsymbol{T} \neq 0$).

When the orientation of the stress fibres is approximately constant along a single cellular arc (figure 4.2a), a general solution of equation (4.2) is straight-forwardly obtained. Taking without loss of generality $\boldsymbol{n} = \hat{\boldsymbol{y}}$, yields the shape of a cellular arc in implicit form:

$$\frac{\sigma^2}{\gamma\lambda_-^2}\,x^2 + \frac{\sigma^2}{\lambda_-^2}\,y^2 = 1\ , \tag{4.3}$$
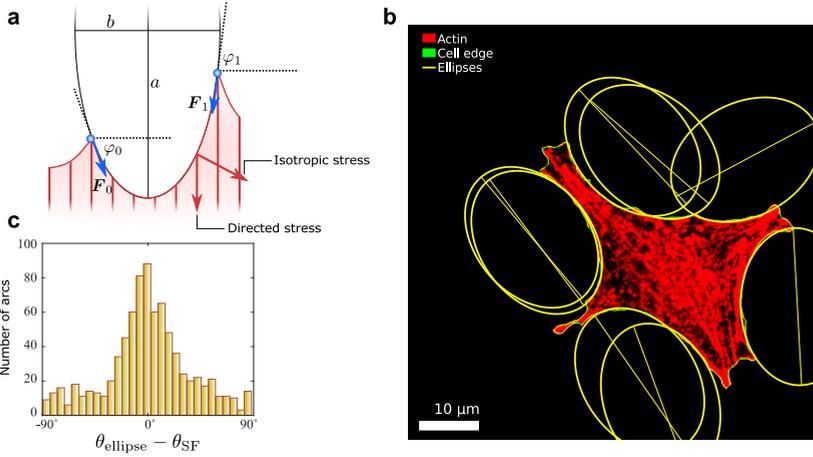
Figure 4.2: **The anisotropic cytoskeleton is reflected in the elliptical shape of the cell edge.** (a) Schematic representation of our model. A force balance between isotropic stress, directed stress and line tension results in the description of each cell edge segment (red curve) as part of an ellipse of aspect ratio $b/a = \sqrt{\gamma}$, unique to each cell. The cell exerts forces $\boldsymbol{F}_0$ and $\boldsymbol{F}_1$ on the adhesion sites (blue) with magnitude $\lambda(\varphi_0)$ and $\lambda(\varphi_1)$. (b) An epithelioid cell (same cell as in Fig. 1a) with a unique ellipse (yellow) fitted to its edges (green). The orientations of the major axes (yellow lines) are parallel to the local orientations of the stress fibers. Scalebar is 10 μm. (c) Histogram of $\theta_{\text{ellipse}} - \theta_{\text{SF}}$, with θ_{ellipse} the orientation of the fitted ellipse and θ_{SF} the measured orientation of the stress fibres. The mean of this distribution is 0° and the standard deviation is 36°.

where $\gamma = \sigma/(\sigma + \alpha)$ and λ_- is a constant that characterises the cortical tension and will be discussed in more detail later. Equation (4.3) describes an ellipse of aspect ratio $\sqrt{\gamma}$ and major semi-axis λ_-/σ, as illustrated in figure 4.2a. The dimensionless quantity γ highlights the interplay between the forces experienced by the cell edge and its shape: on the one hand, γ characterises the anisotropy of the bulk stress, while on the other hand it determines the anisotropy of the cell shape. Furthermore, as $0 \leq \gamma \leq 1$, it follows from equation (4.3) that the major axis of the ellipse is oriented parallel to the stress fibres (figure 4.2a).

The key prediction of our model is illustrated in figure 4.2b and in figure 4.4, where we have fitted the contour of the same cell shown in figure 4.1a with ellipses. Whereas large variations in the circles' radii were required in figure 4.1a, a unique ellipse ($\gamma = 0.52$, $\lambda_-/\sigma = 13.4\,\mu\mathrm{m}$) faithfully describes all the arcs in the cell. While fitting, the directions of the major axes were fixed to be parallel to the local orientations of the stress fibers. To test the accuracy of this latter choice, we fitted unconstrained and independent ellipses to all cellular arcs in our database. The distribution of the difference between the orientation $\theta_{\mathrm{ellipse}}$ of the fitted ellipse and the measured orientation θ_{SF} of the stress fibers is shown in Fig. 2c. The distribution peaks at $0°$ and has a width of $36°$, demonstrating that the orientation of the ellipses is parallel, on average, to the local orientation of the stress fibers as predicted by our model.
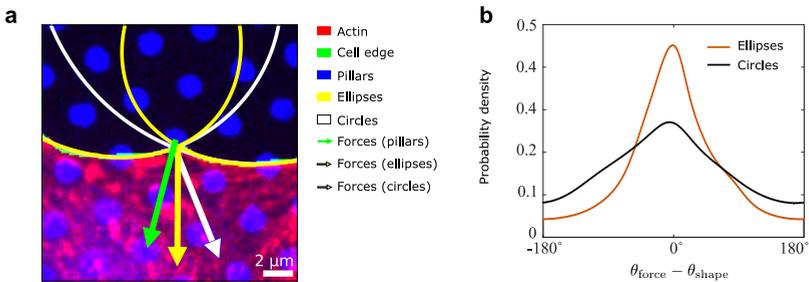
Figure 4.3: **Analysis of the shape of a cell allows to predict the orientations of traction forces. a** Zoom-in on one adhesion site of the cell in the previous figures. Actin is shown in red, the cell edge in green and the tops of the micropillars in blue. Additionally, the fitted ellipses (yellow) and circles (white) and the measured force (green) on the adhesion site, as well as the orientations of the forces calculated using the tension-elasticity model (white) [11], and the model presented in this chapter (yellow) are shown. Scalebar is 2 μm. **b** Histogram (shown as a probability density) of $\theta_{\mathrm{force}} - \theta_{\mathrm{shape}}$ for our anisotropic model (red) and the isotropic tension-elasticity model (black). Both the distributions are centered around $0°$, the standard deviations are $60°$ and $40°$ for the isotropic and anisotropic models respectively.

Equation (4.2) further allows to analytically calculate the cortical tension λ. Namely,

$$\lambda(\varphi) = \lambda_- \sqrt{\frac{1 + \tan^2(\varphi)}{1 + \gamma \tan^2(\varphi)}} \ , \tag{4.4}$$

where φ is the orientation of the tangent vector $\boldsymbol{T}$ with respect to an axis perpendicular to the stress fibres (Fig. 2a). The function λ attains its minimum value at the point along the cellular arc where $\varphi = 0$ and $\lambda(0) = \lambda_-$. Here, the cortical tension has no contribution from the directed stress (i.e. $\boldsymbol{n} \cdot \boldsymbol{T} = 0$), thus λ_- can be interpreted as the intrinsic tension along the cell cortex and, together with σ and α, represents a material parameter of our model.

Equation (4.3) and equation (4.4) are used to predict the traction force exerted by the cell at a specific adhesion site by adding the cortical tension $\lambda\boldsymbol{T}$ along the two cellular arcs joining at the adhesion site. We emphasize that this analysis yields information on cellular forces solely based on the analysis of cell shape. For example, the direction of the traction forces is calculated without additional fitting parameters. We compare the result with the direction of the traction force measured with a micropillar array technology [24–26]. An example is shown in figure 4.3a for one of the adhesion points of the cell in figure 4.2b, more examples are shown in figure 4.4 and figure 4.5. The arrows mark the direction of the measured traction force (green) and that calculated by approximating the cell shape with ellipses (yellow). As a comparison figure 4.3a also shows a prediction based on circles from the isotropic tension-elasticity model (white) [11, 18].

Data for all 285 cells are summarised in figure 4.3b, where we show the distribution of the orientation difference between the force direction predicted by our model θ_{shape} and its experimentally obtained value θ_{force}. Across the cell types used, the predicted distribution is centered at $0°$ and has a width of $40°$. As a comparison, we plot also the result for the earlier isotropic model which displays a significantly larger width of the distribution of $60°$. This significant improvement shows that not only cell shape, but also adhesion forces are profoundly affected by the anisotropy of the cytoskeleton.

γ	λ_- (nN)	σ (nN/µm)	α (nN/µm)
0.33 ± 0.20	7.6 ± 5.6	0.87 ± 0.70	1.7 ± 1.7

Table 4.1: Survey of the average material parameters in a sample of 285 fibroblastoid and epithelioid cells.

Finally, our model permits to obtain quantitative information on the value and importance of the isotropic and anisotropic stresses generated by the cells. We combine the shape parameters γ and λ_-/σ with the value of λ_- that we obtain from the magnitudes of the measured forces. In table 4.1 and table 4.2 we report a survey of the parameter values over a sample of 285 cells. Despite the large variability among the cell population, the directed stress α is consistently larger than the isotropic stress σ, reflecting the high anisotropy of the adherent cell types used here.

4.4   Discussion & Conclusion

In conclusion, we have investigated the geometrical and mechanical properties of adherent cells characterized by an anisotropic actin cytoskeleton, by combining experiments on micropillar arrays with simple mechanical modeling. We have predicted and verified that the shape of the cell edge consists of arcs that are described by a unique ellipse, whose major axis is parallel to the orientation of the stress fibers. The model allowed us to obtain quantitative information on the values of the isotropic and anisotropic contractility of cells.

Our work highlights the strong interplay between cell mechanics and geometry. Our model represents a step toward estimating cellular forces from simple imaging data without the need for sophisticated direct force readout. Furthermore, it provides a starting point to study dynamics and explore the role of anisotropy in multicellular environments like tissues [27–30].

4.5   Materials & Methods

4.5.1   Cell culture and fluorescent labeling

Epithelioid GE11 and fibroblastoid GD25 cells [19] expressing either $\alpha5\beta1$ or $\alpha v\beta3$ (GDβ1, GDβ3, GEβ1 and GEβ3) have been cultured as described before [14]. GDβ1, GDβ3, GEβ1 and GEβ3 are approximately equally represented among the 285 cells in the data presented here. Cells have cultured in medium (DMEM; Dulbecco's Modified Eagle's Medium, Invitrogen/Fisher Scientific) supplemented with 10% fetal bovine serum (HyClone, Etten-Leur, The Netherlands), 25 U/ml penicillin and 25 µg/ml streptomycin (Invitrogen/Fisher Scientific cat. # 15070-063). Cells were fixed in 4% formaldehyde and then permeabilized with 0.1% Triton-X and 0.5% BSA in PBS. Tetramethylrhodamine (TRITC)-Phalloidin (Fisher Emergo B.V. cat. # A12380, Thermo Fisher) was subsequently used to stain F-actin [14].

4.5.2 Micropillar arrays

Micropillar arrays were made out of a soft elastomeric material (PDMS) using a negative silicon wafer as a mask as described before [25, 26]. Briefly, the 2 μm diameter micropillars are arranged in a hexagonal pattern with a 4 μm centre-to-centre distance. The micropillars have a height of 6.9 μm, resulting in a stiffness of 16.2 nN/μm. The pillar tops were fluorescently labeled using an Alexa 405-fibronectin conjugate (Alexa Fluor®, Invitrogen/Fisher Scientific, Breda, The Netherlands; Fibronectin cat. #1141, Sigma Aldrich, Zwijndrecht, The Netherlands). Pillar deflections were determined with ∼30 nm precision using a specifically designed Matlab script resulting in a ∼0.5 nN precision in force [26].

4.5.3 Imaging

High-resolution imaging was performed on an in-house constructed spinning disk confocal microscope based on an Axiovert200 microscope body with a Zeiss Plan-Apochromat 100× 1.4NA objective (Zeiss, Sliedrecht, The Netherlands) and a CSU-X1 spinning disk unit (CSU-X1, Yokogawa, Amersfoort, The Netherlands). Imaging was done using an emCCD camera (iXon 897, Andor, Belfast, UK). Alexa405 and TRITC were exited using 405 nm (Crystalaser, Reno, NV) and 561 nm (Cobolt, Stockholm, Sweden) lasers, respectively.

4.5.4 Image analysis

All image analysis and ellipse fitting are performed using Matlab®, except the determination of the stress fiber orientation for which ImageJ with the OrientationJ plugin (`http://bigwww.epfl.ch/demo/orientation/`) was used. The micropillar array allows measuring forces that the cell exerts on the substrate. The forces used in calculations were selected manually when sufficiently large and close to the cell edge. The cell edge is found using a custom script that filters background using a lowpass filter and selects the cell based on a threshold. Then the contour of the cell is divided into parts at the locations of the selected forces. Segments whose straight end-to-end distance is less than 50 pixels (6.9 μm) are discarded, the rest of the segments is used for fitting ellipses.

The orientation of cell edge segments as used in figure 4.1c was calculated by measuring the angle of a line through the two adhesions at either end of the segment. We then defined θ as the angle between this line and the stress fibers.

4.5.5   Ellipse fitting

Ellipses are defined in our experiments with five parameters each: the coordinates of the center of the ellipse, the lengths of the short and long axes, and the angle that the long axis of the ellipse makes with the x-axis of the coordinate system of the image. We use fixed lengths for long and short axes for the N ellipses in the same cell. The optimal ellipse size per cell and positions for each ellipse are found using a $2(N+1)$ parameter fit which minimises the distance between fitted ellipses and cell edge by calculating χ^2. Initial parameters for this fit are obtained from fitting each ellipse separately and averaging the lengths of the axes of the ellipses. Ellipses whose χ^2 is greater than 10 are discarded, which occurs in case of membrane ruffling and other out-of-equilibrium events.

In the global fit, the orientations of the ellipses are fixed to the local orientations of stress fibers. Orientations are measured from the channel with TRITC-Phalloidin (Actin) using the OrientationJ plugin for ImageJ. The average orientation per cell edge segment is calculated over all pixels between 15 and 50 pixels ($2.07\,\mu\text{m}$ and $6.9\,\mu\text{m}$) away from the cell edge whose coherency is greater than 0.15.

4.5.6   Force analysis

For both the circle and ellipse models, forces on the intersections of circles or ellipses are calculated. For circles, these forces are the vector sum of two forces whose direction is on the tangent to the circle and whose relative magnitude is the radius of the circle. For the ellipse case, the position of the single force on the intersection of two ellipses is first mapped to two forces on a single ellipse. While doing this the short and long axes of the ellipse are rotated and translated such that they coincide with the x and y-axes of the coordinate system. Then two forces $\boldsymbol{F}_1$ and $\boldsymbol{F}_0$ are calculated by combining equation (4.3) and equation (4.4), and defined in such a way that they are pointing clockwise

and counter-clockwise around the ellipse:

$$
\begin{aligned}
\frac{\boldsymbol{F}_0}{\lambda_-} &= (\beta \sin \phi + \zeta \cos \phi)\,\hat{\boldsymbol{x}} + \left(-\frac{\beta}{\gamma}\cos \phi + \zeta \sin \phi\right)\hat{\boldsymbol{y}} \\
\frac{\boldsymbol{F}_1}{\lambda_-} &= (\beta \sin \phi - \zeta \cos \phi)\,\hat{\boldsymbol{x}} + \left(-\frac{\beta}{\gamma}\cos \phi - \zeta \sin \phi\right)\hat{\boldsymbol{y}} \\
\beta &= \frac{d}{2a} \\
\zeta &= \sqrt{\frac{1+\tan^2 \phi}{1+\gamma \tan^2 \phi} - \frac{\beta^2}{\gamma}}\;.
\end{aligned}
\tag{4.5}
$$

Here d is the distance between the positions of both forces on the ellipse, a is the length of the long axis of the ellipse and ϕ is the angle that the line through both points makes with the x-axis. After this $\boldsymbol{F}_0$ and $\boldsymbol{F}_1$ are rotated back to the coordinate system of the image and summed to give the force, scaled by λ_-, acting on the cell edge on the location of a particular intersection of two ellipses.

The magnitude of the traction forces is required for the calculation of the minimal line tension λ_- and the isotropic and directed stresses σ and α. We get this from the micropillar array. A measured force usually is the sum of two forces exerted by two different cell edge segments. Therefore, we first decompose the traction force into two forces pointing along tangents to the two cell edge segments adjacent to the position of the force. Then, per cell, we take any combination of two clockwise and counter-clockwise forces and calculate:

$$
\begin{aligned}
\lambda_- &= \sqrt{\frac{F_{1x}^2 F_{0y}^2 - F_{0x}^2 F_{1y}^2}{F_{0y}^2 - F_{1y}^2}} \\
\sigma &= \frac{|\boldsymbol{F}_0 - \boldsymbol{F}_1|}{d}\frac{F_{0x}+F_{1x}}{F_{0y}-F_{1y}} \\
\alpha &= \sigma\left(\frac{1}{\gamma}-1\right)\;.
\end{aligned}
\tag{4.6}
$$

Here $\boldsymbol{F}_0$ and $\boldsymbol{F}_1$ are defined in the coordinate system where the x and y-axes are the short and long axes of the ellipse. Furthermore, F_{nx} and F_{ny} are the components of $\boldsymbol{F}_n$ in the x and y-directions respectively. To calculate values for these quantities, we average all the different tensions and stresses we get for all possible combinations in all cells, taking the errors on these values into account as weights while averaging.

4.6 Supplementary data

Table 4.1 gives the material parameters γ, λ_-, σ and α for a set of 285 cells. These cells, in fact, come from a pool of two different cell types [14, 19]. The GE11 cells used, exhibit an epithelioid morphology whereas the GD25 cells exhibit a fibroblastoid morphology. Both cell types are deficient of the fibronectin receptor integrin β1. In both cell types, then either α5β1 was reexpressed, or αvβ3 was expressed. These cells are designated GEβ1, GEβ3, GDβ1 and GDβ3. The differing cell and integrin types result in a different cell-substrate coupling leading to different material parameters for each cell and integrin expression type. It is outside the scope of this chapter to examine these differences in detail, therefore initially only the average of each parameter over all 285 cells are given. For completeness, we give the same parameters per cell type in table 4.2. As can be expected [14], cells expressing β1 exert higher traction forces than cells expressing β3, which is reflected in a lower λ_- for the latter.

Cell type	number of cells	γ	λ_- (nN)	σ (nN/μm)	α (nN/μm)
GEβ1	59	0.32 ± 0.14	9.8 ± 6.9	1.4 ± 1.0	2.6 ± 2.2
GEβ3	112	0.31 ± 0.19	5.5 ± 3.4	0.62 ± 0.41	1.3 ± 1.1
GDβ1	56	0.38 ± 0.26	10.6 ± 9.4	0.92 ± 0.78	1.5 ± 1.7
GDβ3	58	0.34 ± 0.25	7.9 ± 6.0	1.0 ± 0.8	2.0 ± 2.2
All	285	0.33 ± 0.20	7.6 ± 5.6	0.87 ± 0.70	1.7 ± 1.7

Table 4.2: Survey of the average material parameters per cell type in a sample of 285 fibroblastoid and epithelioid cells. Shown are the mean and standard deviation. Whereas γ does not vary significantly, there is some variance observed in especially λ_-, which appears larger for cells expressing β-integrin.
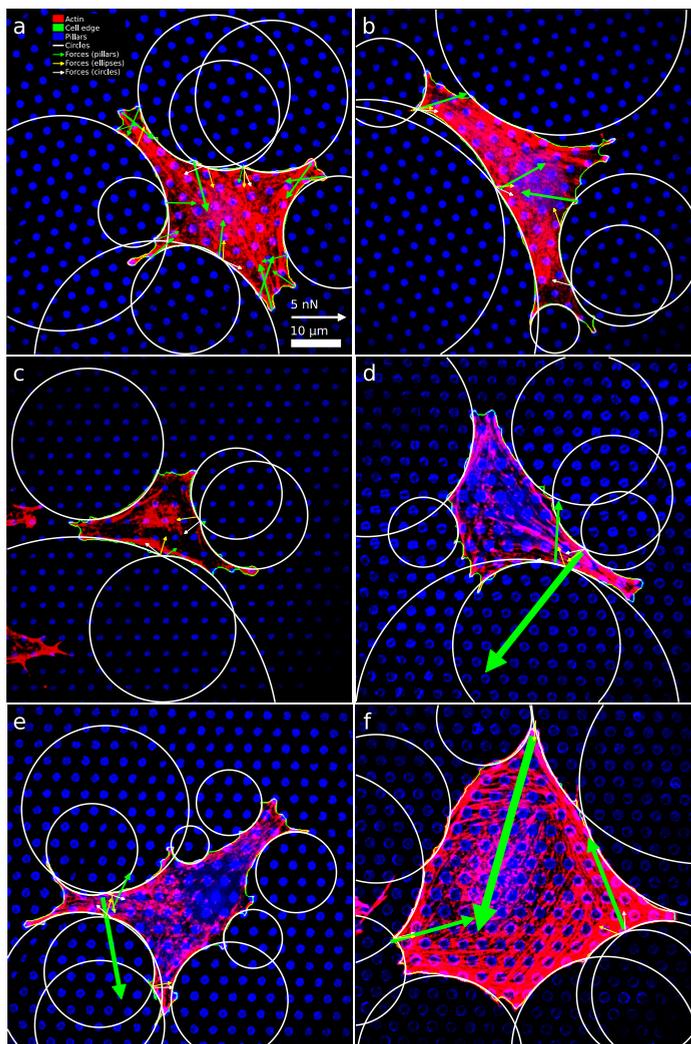
Figure 4.4: **Six examples of cells with circles fitted to the cell edges.**
The actin, cell edge, and micropillar tops are in the red, green and blue channels
respectively. Circles (white) are fitted to the edge of the cells. Orientations
of forces calculated on intersections of either circle from the tension-elasticity
model [11, 18] (white arrows) and the model presented in this chapter (yellow
arrows) are shown as well as the forces measured with the micropillar array
(green arrows). Panels (a) to (c) show epithelioid cells and (d) to (f) show
fibroblastoid cells.
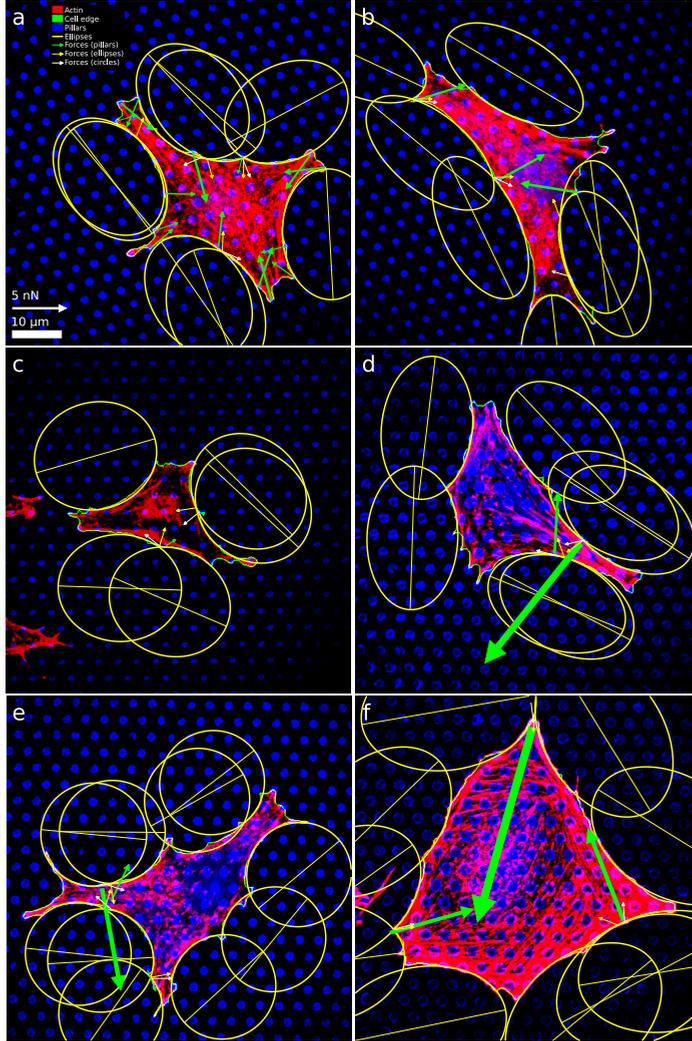
Figure 4.5: **Six examples of cells (same as in Fig. 4) with ellipses fitted to the cell edges.** The actin, cell edge and micropillar tops are in the red, green and blue channels respectively. Ellipses (yellow, including the long axis) are fitted to the edge of the cells. Orientations of forces calculated on intersections of either circles form the tension-elasticity model [11, 18] (white arrows) and the model presented in this chapter (yellow arrows) are shown as wel as the forces measured with the micropillar array (green arrows). Panels (a) to (c) show epithelioid cells and (d) to (f) show fibroblastoid cells. Fit values for the ellipses in panels (a) to (f) respectively: γ: 0.52; 0.25; 0.75; 0.40; 0.95; 0.46, λ_-/σ (μm): 13.4; 15.7; 12.6; 14.7; 10.8; 18.0.

References

[1] B. Geiger, J. P. Spatz, and A. D. Bershadsky. "Environmental sensing through focal adhesions". In: *Nat. Rev. Mol. Cell Biol.* 10.1 (2009), pp. 21–33. DOI: 10.1038/nrm2593.

[2] D. E. Discher, P. Janmey, and Y. L. L. Wang. "Tissue cells feel and respond to the stiffness of their substrate". In: *Science* 310.5751 (2005), pp. 1139–1143. DOI: 10.1126/science.1116995.

[3] F. Jülicher et al. "Active behavior of the Cytoskeleton". In: *Phys. Rep.* 449.1-3 (2007), pp. 3–28. DOI: 10.1016/j.physrep.2007.02.018.

[4] B. D. Hoffman, C. Grashoff, and M. a. Schwartz. "Dynamic molecular processes mediate cellular mechanotransduction". In: *Nature* 475.7356 (2011), pp. 316–323. DOI: 10.1038/nature10316.

[5] M. G. Mendez and P. A. Janmey. "Transcription factor regulation by mechanical stress". In: *Int. J. Biochem. Cell Biol.* 44.5 (2012), pp. 728–732. DOI: 10.1016/j.biocel.2012.02.003.

[6] A. J. Engler et al. "Matrix elasticity directs stem cell lineage specification". In: *Cell* 126.4 (2006), pp. 677–89. DOI: 10.1016/j.cell.2006.06.044.

[7] B. Trappmann et al. "Extracellular-matrix tethering regulates stem-cell fate". In: *Nat. Mater.* 11.7 (2012), pp. 642–9. DOI: 10.1038/nmat3339.

[8] Y. Sawada et al. "Force sensing by mechanical extension of the Src family kinase substrate p130Cas". In: *Cell* 127.5 (2006), pp. 1015–1026. DOI: 10.1016/j.cell.2006.09.044.

[9] C. M. Lo et al. "Cell movement is guided by the rigidity of the substrate". In: *Biophys. J.* 79.1 (2000), pp. 144–152. DOI: 10.1016/S0006-3495(00)76279-5.

[10] R. D. Sochol et al. "Unidirectional mechanical cellular stimuli via micro-post array gradients". In: *Soft Matter* 7.10 (2011), pp. 4606–4609. DOI: 10.1039/c1sm05163f.

[11] I. B. Bischofs, S. S. Schmidt, and U. S. Schwarz. "Effect of adhesion geometry and rigidity on cellular force distributions". In: *Phys. Rev. Lett.* 103.4 (2009), p. 048101. DOI: 10.1103/PhysRevLett.103.048101.

[12] M. Ghibaudo et al. "Substrate topography induces a crossover from 2D to 3D behavior in fibroblast migration". In: *Biophys. J.* 97.1 (2009), pp. 357–368. DOI: 10.1016/j.bpj.2009.04.024.

[13]   D. A. Fletcher and R. D. Mullins. "Cell mechanics and the cytoskeleton".
        In: *Nature* 463.7280 (2010), pp. 485–92. DOI: 10.1038/nature08908.

[14]   H. E. Balcioglu et al. "The integrin expression profile modulates orienta-
        tion and dynamics of force transmission at cell-matrix adhesions". In: *J.
        Cell Sci.* 128.7 (2015), pp. 1316–1326. DOI: 10.1242/jcs.156950.

[15]   U. S. Schwarz and S. A. Safran. "Physics of adherent cells". In: *Rev. Mod.
        Phys.* 85.3 (2013), pp. 1327–1381. DOI: 10.1103/RevModPhys.85.1327.

[16]   L. Giomi. "Softly constrained films". In: *Soft Matter* 9.34 (2013), pp. 8121–
        8139. DOI: 10.1039/c3sm50484k.

[17]   R. Bar-Ziv et al. "Pearling in cells: A clue to understanding cell shape".
        In: *Proc. Natl. Acad. Sci.* 96.18 (1999), pp. 10140–10145. DOI: 10.1073/
        pnas.96.18.10140.

[18]   I. B. Bischofs et al. "Filamentous network mechanics and active con-
        tractility determine cell and tissue shape". In: *Biophys. J.* 95.7 (2008),
        pp. 3488–3496. DOI: 10.1529/biophysj.108.134296.

[19]   E. H. J. Danen et al. "The fibronectin-binding integrins $\alpha5\beta1$ and $\alpha v\beta3$
        differentially modulate RhoA–GTP loading, organization of cell matrix
        adhesions, and fibronectin fibrillogenesis". In: *J. Cell Biol.* 159.6 (2002),
        pp. 1071–1086. DOI: 10.1083/jcb.200205014.

[20]   S. Pellegrin and H. Mellor. "Actin stress fibres". In: *J. Cell Sci.* 120.20
        (2007), pp. 3491–3499. DOI: 10.1242/jcs.018473.

[21]   K. Burridge and E. S. Wittchen. "The tension mounts: Stress fibers
        as force-generating mechanotransducers". In: *J. Cell Biol.* 200.1 (2013),
        pp. 9–19. DOI: 10.1083/jcb.201210090.

[22]   T. J. Pedley and J. O. Kessler. "Hydrodynamic phenomena in suspensions
        of swimming microorganisms". In: *Annu. Rev. Fluid Mech.* 24.1 (1992),
        pp. 313–358. DOI: 10.1146/annurev.fl.24.010192.001525.

[23]   R. Aditi Simha and S. Ramaswamy. "Hydrodynamic fluctuations and
        instabilities in ordered suspensions of self-propelled particles". In: *Phys.
        Rev. Lett.* 89.5 (2002), p. 058101. DOI: 10.1103/PhysRevLett.89.
        058101.

[24]   J. L. Tan et al. "Cells lying on a bed of microneedles: An approach to
        isolate mechanical force". In: *Proc. Natl. Acad. Sci. U. S. A.* 100.4 (2003),
        pp. 1484–1489. DOI: 10.1073/pnas.0235407100.

[25]   L. Trichet et al. "Evidence of a large-scale mechanosensing mechanism
        for cellular adaptation to substrate stiffness". In: *Proc. Natl. Acad. Sci.
        U. S. A.* 109.18 (2012), pp. 6933–6938. DOI: 10.1073/pnas.1117810109.

[26] H. Van Hoorn et al. "The nanoscale architecture of force-bearing focal adhesions". In: *Nano Lett.* 14.8 (2014), pp. 4257–4262. DOI: `10.1021/nl5008773`.

[27] M. Eastwood et al. "Effect of precise mechanical loading on fibroblast populated collagen lattices: Morphological changes". In: *Cell Motil. Cytoskeleton* 40.1 (1998), pp. 13–21. DOI: `10.1002/(SICI)1097-0169(1998)40:1<13::AID-CM2>3.0.CO;2-G`.

[28] D. W. van der Schaft et al. "Mechanoregulation of vascularization in aligned tissue-engineered muscle: A role for vascular endothelial growth factor". In: *Tissue Eng. Part A* 17.21-22 (2011), pp. 2857–2865. DOI: `10.1089/ten.tea.2011.0214`.

[29] R. F. M. van Oers et al. "Mechanical cell-matrix feedback explains pairwise and collective endothelial cell behavior in vitro". In: *PLoS Comput. Biol.* 10.8 (2014), e1003774. DOI: `10.1371/journal.pcbi.1003774`.

[30] D. S. Vijayraghavan and L. A. Davidson. "Mechanics of neurulation: From classical to current perspectives on the physical mechanics that shape, fold, and form the neural tube". In: *Birth Defects Res.* 109.2 (2017), pp. 153–168. DOI: `10.1002/bdra.23557`.

Chapter 5

Reconstruction of an $\alpha_v\beta_3$ phenotype in $\alpha_5\beta_1$ expressing cells on Rho-kinase down regulation[†]

The mechanical model introduced in the previous chapter is used to look at a changing cytoskeleton. We administered ROCK inhibitor, which effectively weakens the cytoskeleton. This weakening we quantified by the use of micropillar arrays and our mechanical model. We see that ROCK inhibitor mainly weakens the contractility of stress fibers. This makes the cytoskeleton more isotropic, which is reflected in the shape of the cell.

[†]This chapter is based on: W. Pomp, K.K. Schakenraad et al. "Reconstruction of an $\alpha_v\beta_3$ phenotype in $\alpha_5\beta_1$ expressing cells on Rho-kinase down regulation". In preparation.

5.1   Introduction

With the current demonstration of cellular response on external mechanical stimuli [1, 2] it has become clear that cells together with their direct environment form an intertwined system in which mechanical cues from the extracellular matrix (ECM) lead to change in cellular response, the so-called 'outside-in coupling', and likewise cells restructure the ECM through the forces they develop, the so-called 'inside-out coupling'. It has been found that coupling occurs at specific sites at the periphery of the cell, termed focal adhesions (FAs) [3–6]. At FAs ECM-proteins are recognized by transmembrane integrin receptors which are specific for the type of ECM. On the intracellular side, integrins are mechanically coupled through a yet unknown arrangement of intermediate adaptor proteins to the force-generating actin skeleton of the cell.

The specificity of the integrins has been thoroughly investigated [7–9]. During development, angiogenesis and wound healing, the stoichiometry of the fibronectin receptors, integrin $\alpha_5\beta_1$ and integrin $\alpha_v\beta_3$, change leading to differential response on matrix stiffness [10, 11]. Likewise, such change in stoichiometry has been reported in cancer progression [12, 13]. In an earlier study, it was shown that enhanced $\alpha_v\beta_3$ expression could fully compensate for the loss of $\alpha_5\beta_1$ in knock-out cells in terms of cell spreading and migratory behavior [11]. Yet we further observed, that the structure of the internal actomyosin network significantly changed. Whereas in $\alpha_5\beta_1$ expressing cells the cytoskeleton was largely ordered in long fibers, $\alpha_v\beta_3$ expressing cells were characterized by significantly shortened, non-directional fibers [11]. This differential organization of the cytoskeleton resulted in a highly organized central force generation in $\alpha_5\beta_1$ expressing cells, whereas directionality of force generation in $\alpha_v\beta_3$ expressing cells was largely isotropic.

Those earlier findings spurred the hypothesis, that a reduction of intracellular contractility in $\alpha_5\beta_1$ expressing cells, would lead to a major redistribution between isotropic and anisotropic contractility. In chapter 4 we developed an imaging-based methodology that allowed us to quantitively determine the isotropic and anisotropic contractility of cells. Here, we utilized this new methodology to analyze how specific inhibition of the actin-myosin contractility leads to a redistribution between isotropic and directional stresses in $\alpha_5\beta_1$-dominated cells.

5.2 Results

5.2.1 Force Analysis

In chapter 4 we have developed a mechanical model that quantitatively relates cellular forces to the elliptical shape of the cell's outline (figure 5.1). The cell's outline between two focal adhesions (blue dots in figure 5.1) is faithfully described by an elliptical arc, the shape of which is dictated by the mechanical force balance on the cell edge. The resulting forces, as schematically shown in figure 5.1 (blue arrows), are labeled 0 and 1, respectively, clockwise around the ellipse. The magnitude and direction of the forces are given by:
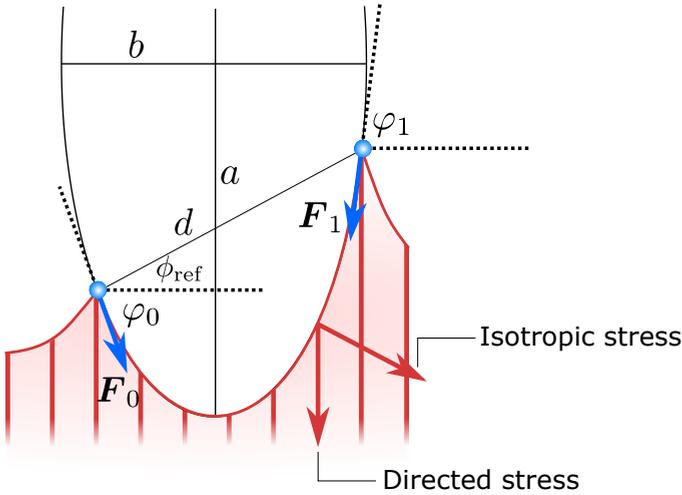

Figure 5.1: **Schematic depiction of a part of a cell.** The cell edge (curved red line) is fixed in adhesions (blue points) to the membrane. In between these points, the membrane assumes the shape of part of an ellipse (black). The long axis a of the ellipse is aligned with the stress fibers (red) inside the cell. The forces $\vec{F}_0$ and $\vec{F}_1$ (blue arrows) are ordered counter-clockwise on the edge and are angent to the ellipse. Angles between the tangents at the locations of the forces and the ellipse are labeled ϕ_0 and ϕ_1. The angle between the line (length d) connecting the forces and the short axis b of the ellipse is ϕ_{ref}.

$$\vec{F}_0 = \lambda_- \left[\frac{d}{2a\gamma} \begin{pmatrix} \gamma \sin \phi_{\text{ref}} \\ -\cos \phi_{\text{ref}} \end{pmatrix} + A \begin{pmatrix} \cos \phi_{\text{ref}} \\ \sin \phi_{\text{ref}} \end{pmatrix} \right] \tag{5.1}$$

$$\vec{F}_1 = \lambda_- \left[\frac{d}{2a\gamma} \begin{pmatrix} \gamma \sin \phi_{\text{ref}} \\ -\cos \phi_{\text{ref}} \end{pmatrix} - A \begin{pmatrix} \cos \phi_{\text{ref}} \\ \sin \phi_{\text{ref}} \end{pmatrix} \right] \tag{5.2}$$

Here d is the cartesian distance between the adhesion points, λ_- is a scaling factor that characterizes the lowest attainable line tension in the ellipse, and ϕ_{ref} is the angle between the line connecting the two endpoints and the short axis of the ellipse. γ is the shape factor of the ellipse relating the isotropic contractility σ and the directed contractility α:

$$\gamma = \frac{\sigma}{\sigma + \alpha} \tag{5.3}$$

It should be stressed that there is a unique ellipse that describes the contractility of a cell, and hence all forces observed (chapter 4). Furthermore,

$$A = \sqrt{\frac{1 + \tan^2 \phi_{\text{ref}}}{1 + \gamma \tan^2 \phi_{\text{ref}}} - \frac{\sigma^2 d^2}{4\gamma \lambda_-^2}} \tag{5.4}$$

Combination of the cartesian components of the F_i's (equations (5.1) and (5.2)), together with the distance d allowes one to calculate γ, σ, α and λ_- for a given cell just by analysis of the cell's shape:

$$\gamma = -\frac{F_{0x}^2 - F_{1x}^2}{F_{0y}^2 - F_{1y}^2} \tag{5.5}$$

$$\sigma = \frac{|\vec{F}_0 - \vec{F}_1|}{d} \frac{F_{0x} + F_{1x}}{F_{0y} - F_{1y}} \tag{5.6}$$

$$\alpha = \sigma \left(\frac{1}{\gamma} - 1 \right) \tag{5.7}$$

$$\lambda_- = \sqrt{\frac{F_{1x}^2 F_{0y}^2 - F_{0x}^2 F_{1y}^2}{F_{0y}^2 - F_{1y}^2}} \tag{5.8}$$

This strategy, as validated in chapter 4, has been used here to determine the cellular force-generation in a series of experiments in which the actin-myosin contractility was pharmacologically disturbed.
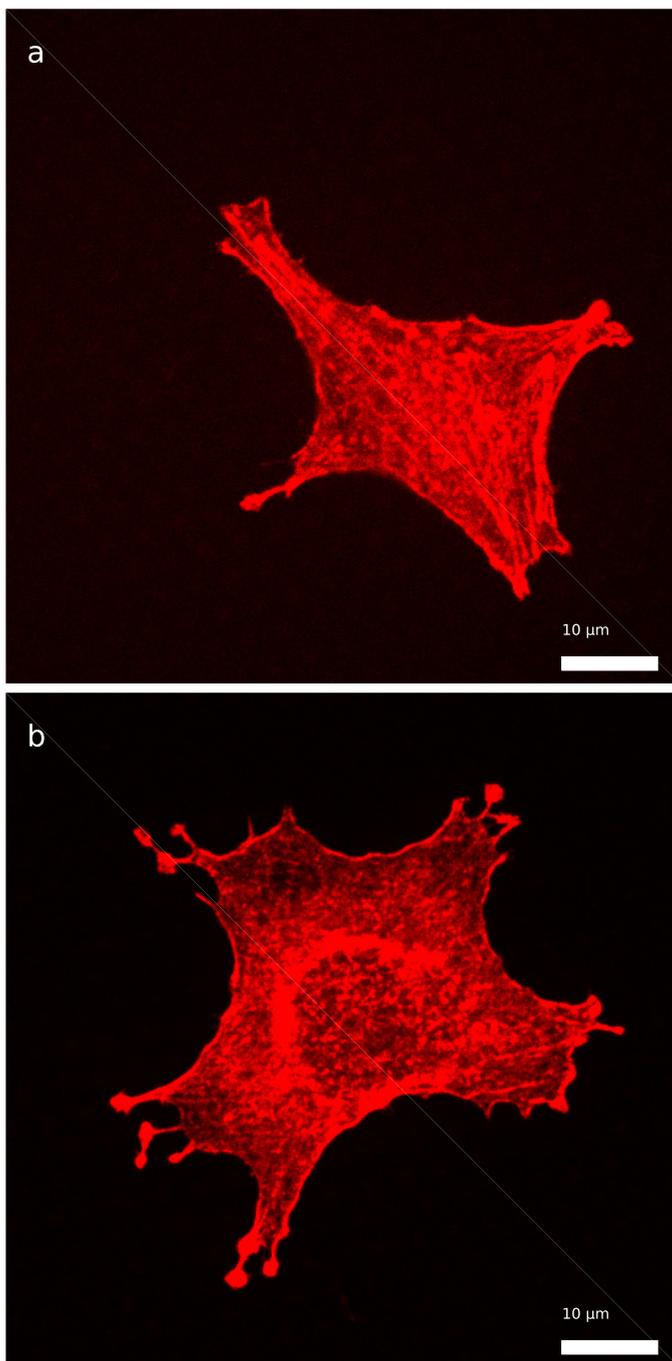
Figure 5.2: **Two cells, with actin visible in red, one with and one without ROCK inhibitor. The difference in spreading area is visible. a** No ROCK inhibitor. Area=619 μm^2. **b** 1 μM ROCK inhibitor. Area=1024 μm^2.

5.2.2   Change in cell spreading on inhibition of the actin-myosin contractility

Mouse-embryo-derived neuroepithelial cells (GE11) lacking the β_1 subunit after re-expression of β_1 (GEβ1) were found to regain contractility mediated by RhoA and Rho-kinase ROCK. Cells displayed enhanced random migration in two-dimensional motility assays [11, 14, 15]. The Rho-kinase ROCK promotes in mammalian cells phosphorylation of the myosin light chain, increasing the activity of myosin II. Inhibition of ROCK hence reduces the activity of myosin II and concomitantly the contractility of actin stress fibers. The latter largely determine the isotropic contractility α of the cell.
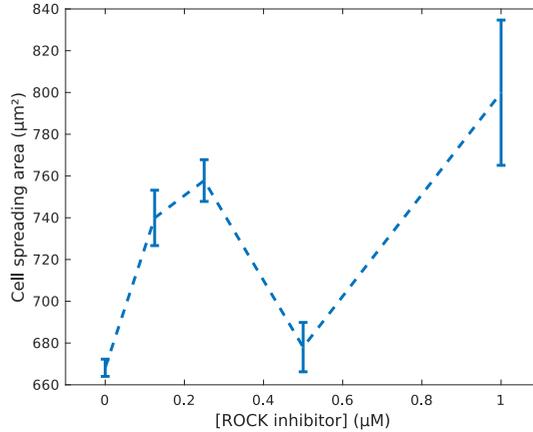

Figure 5.3: **Increase of cell spreading-area versus on application of ROCK inhibitor.** Except for $0.5\,\mu$M, the cell spreading area increases with increasing concentrations of ROCK inhibitor.

Here we analysed GEβ1 cells under influence of three different concentrations of the specific ROCK inhibitor Y27632: 0, 0.125, 0.25, 0.5 and $1\,\mu$M. As of the reduced contractility, it has been reported that cells exhibit an increase in spreading area on the application of ROCK-inhibitor [11, 16]. Our data followed this expectation. In figure 5.2 the effect is illustrated on two cells.

Before treatment cells had a smaller, compact shape ($619\,\mu\text{m}^2$ for the cell shown) with pronounced long stress fibers (figure 5.2a). After incubation of cells with $1\,\mu\text{M}$ for an hour with the ROCK-inhibitor cells are more spread ($1024\,\mu\text{m}^2$ for the cell shown), the long stress fibers were largely shortened, and actin fibers localized to the peri-nuclear region (figure 5.2b).

In figure 5.3 we summarize results from ensemble data which show that the cell spreading area increases from $(670 \pm 4)\,\mu\text{m}^2$ for cells without ROCK inhibitor to $(800 \pm 35)\,\mu\text{m}^2$ for cells to which $1\,\mu\text{M}$ of ROCK-inhibitor was added.
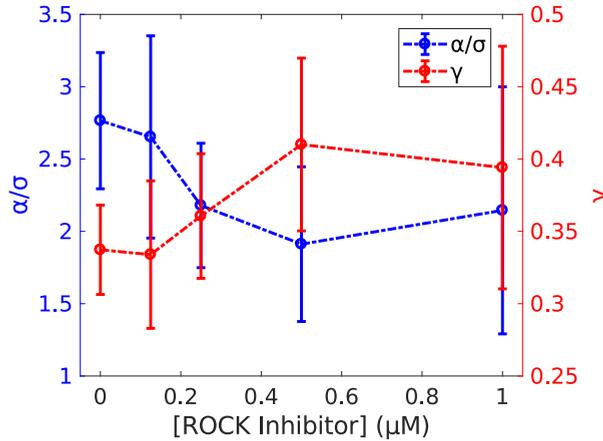

Figure 5.4: **The shape factor γ and the ratio of directed contractilty α and isotropic contractilitie σ as a function of the concentration of ROCK inhibitor.** The shape factor γ is calculated from the lengths of the major axis a and the minor axis b from ellipses fitted to cells by $\gamma = b^2/a^2$. The ratio α/σ is calculated from γ: $\alpha/\sigma = (1/\gamma - 1)^{-1}$.

5.2.3 Change in cell shape on inhibition of actin-myosin contractility

ROCK is a known factor in the regulation of the shape of cells by changing the organization of the actin cytoskeleton and of spreading behavior. By gradual inhibition of the actin-myosin contractility, we predicted that the directional component of cellular stress (α) will be influenced. Reduction in α will lead to a reduction in the ellipticity γ of arcs following the cell's outline; the unique ellipse will transform into a unique circle. Our data agree with this hypothesis. Figure 5.4 shows the change in the shape factor γ when the concentration of the ROCK-inhibitor Y27632 was increased up to $1\,\mu$M (red). Notably, the shape-factor of the cell decreased at constant isotropic contractility σ, while the directed contractility α, which is generated by myosin in stress fibers, decreased. The ratio α/σ is shown in blue. In the given concentration range α/σ changes from 3 to 1.5: all arcs assumed a more circular shape ($[\alpha/\sigma]_{\text{circle}} = 0$).

5.2.4 Change in traction forces on inhibition of the actin-myosin contractility

We further investigated, which of the cell's material parameters σ, α and λ_- were influenced by the change in actin-myosin contractility on ROCK-inhibitor application. For this analysis, the methodology developed in equations (5.6) to (5.8) was used, where these material parameters are expressed as a function of force on, and the distance between the adhesion points. The results are summarized in figures 5.6, 5.7 and 5.8. The material parameters were measured for cells incubated with different concentrations of ROCK inhibitor, namely: 0, 0.125, 0.25, 0.5 and $1\,\mu$M. The resulting histograms display a broad range of values, reflecting the diversity found in biological systems. By following the mean of the distributions as the concentration of ROCK inhibitor increases, we see that the directed contractility α (figure 5.6) decreases with increasing concentration of ROCK inhibitor. The isotropic contractility σ (figure 5.7) however, does not change discernably.

Figure 5.5 summarizes figures 5.6 and 5.7 by showing the means of α and σ. The influence of the ROCK inhibitor on the isotropic stress σ is clear. Throughout the concentration range used, the mean value of $\sigma = 0.9\,\text{nN}/\mu\text{m}$ was found to be independent of the concentration of ROCK inhibitor. That finding contrasts with the results for the isotropic stress α. α decreased by a factor of 3 after cells were treated with $1\,\mu$M Y27632 from 2 to $0.7\,\text{nN}/\mu\text{m}$.
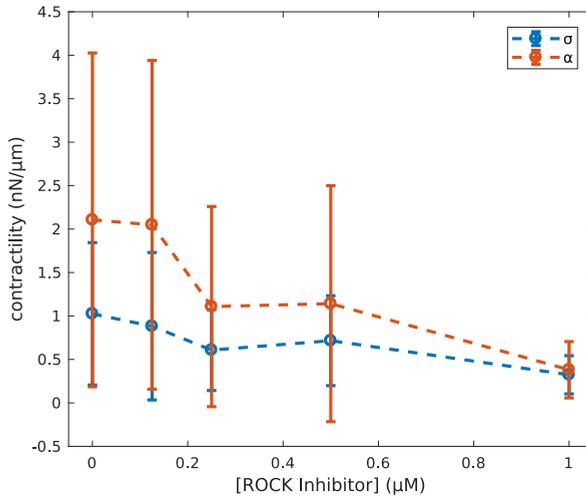
Figure 5.5: **The directed contractility α (blue) and the isotropic contractilty σ (red),** as calculated using equations (5.6) and (5.7).

The associated results for the other parameters are shown in figures 5.8 to 5.10. Whereas the scaling factor λ_- (figure 5.8) was independent on application of the ROCK-inhibitor ($\lambda_- = (5.5 \pm 3.4)\,\text{nN/µm}$), the ellipticity γ (figure 5.9) and asymmetry of the ellipse $\alpha/\sigma = 1/\gamma - 1$ (figure 5.10), clearly change, again showing the result of ROCK inhibitor on the shape of cells. The ellipticity and asymmetry reflect more circular ellipses with increasing ROCK inhibitor concentrations, which points to a cytoskeleton which becomes more isotropic, presumably by affecting the contractility of stress fibers in the cell.
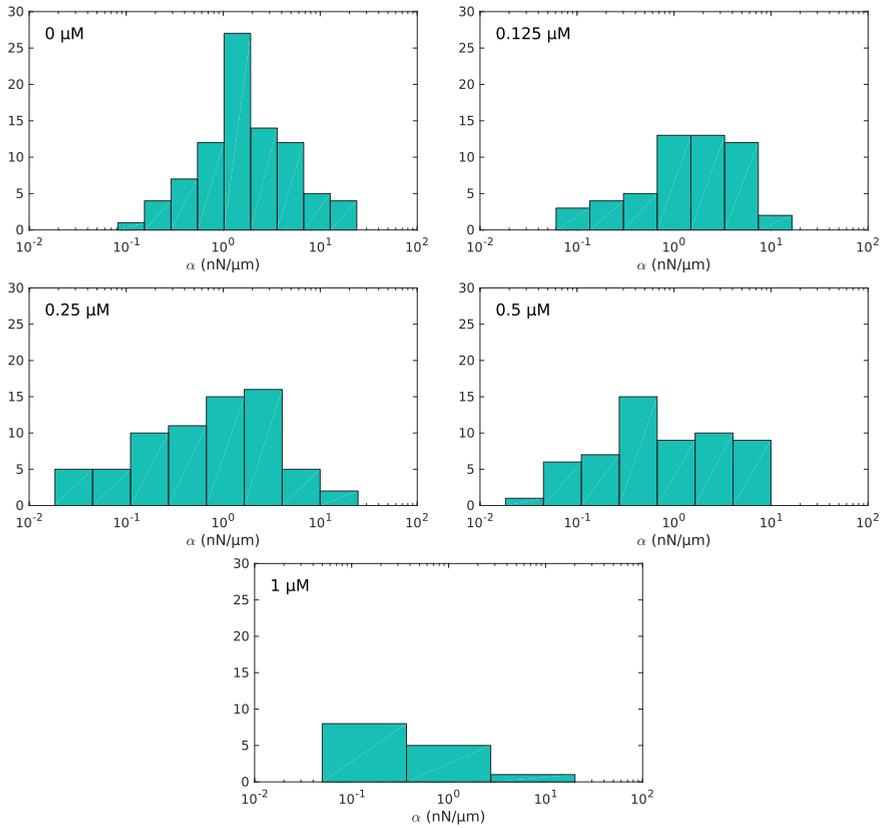
Figure 5.6: **Distributions of the measured directed contractility α for five different concentrations of ROCK inhibitor** (0, 0.125, 0.25, 0.5 and 1 µM).
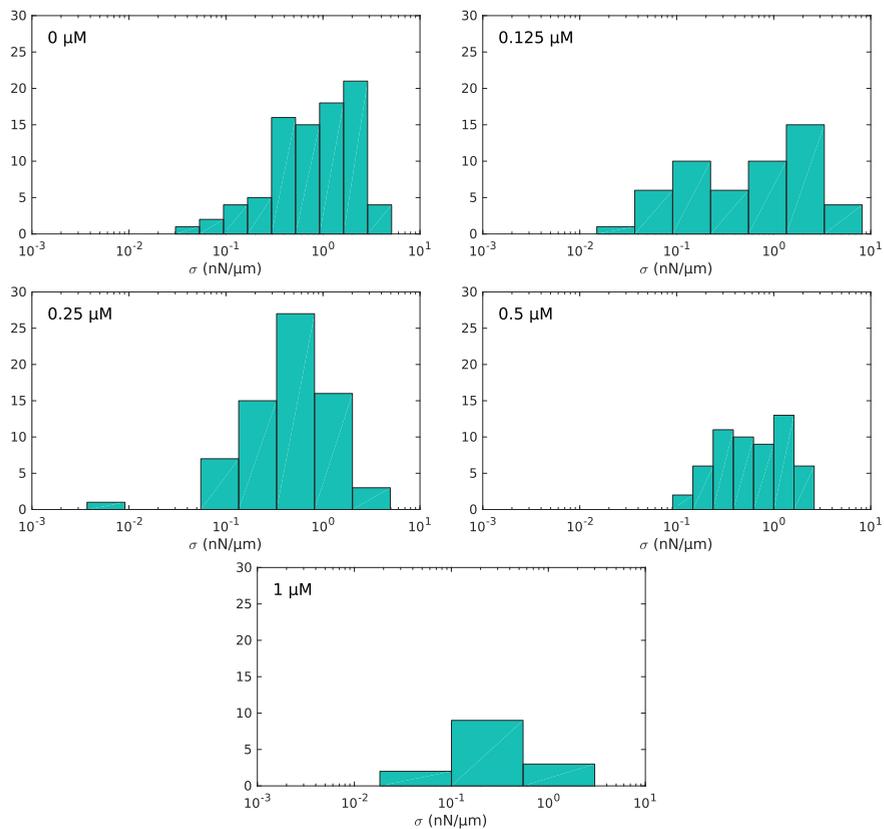
Figure 5.7: **Distributions of the measured isotropic contractility σ for five different concentrations of ROCK inhibitor** (0, 0.125, 0.25, 0.5 and 1 µM), as calculated using equation (5.6).
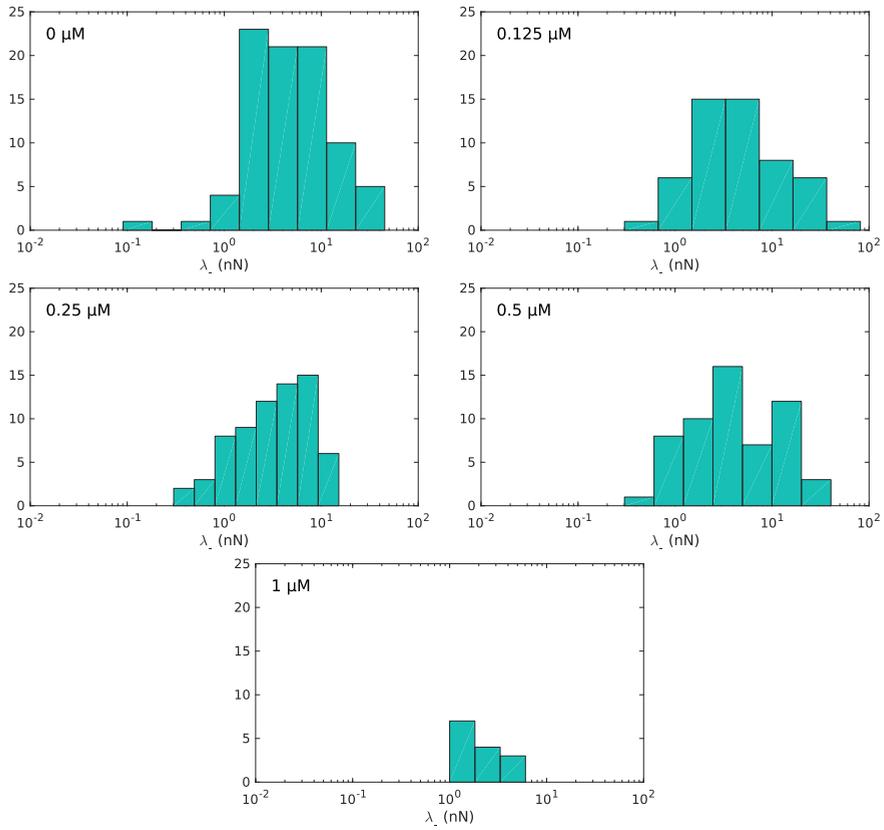
Figure 5.8: **Distributions of the measured membrane tension λ_- for five different concentrations of ROCK inhibitor** (0, 0.125, 0.25, 0.5 and 1 µM), as calculated using equation (5.8).
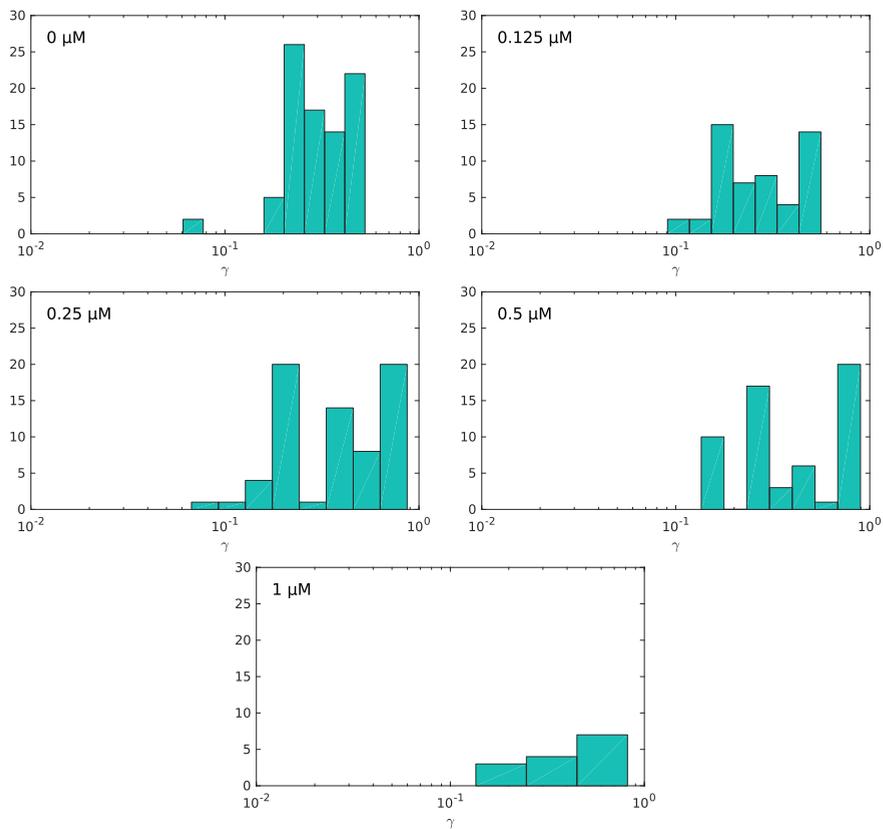
Figure 5.9: **Distributions of the measured shape factor γ for five different concentrations of ROCK inhibitor** (0, 0.125, 0.25, 0.5 and 1 µM), as calculated using equation (5.5).
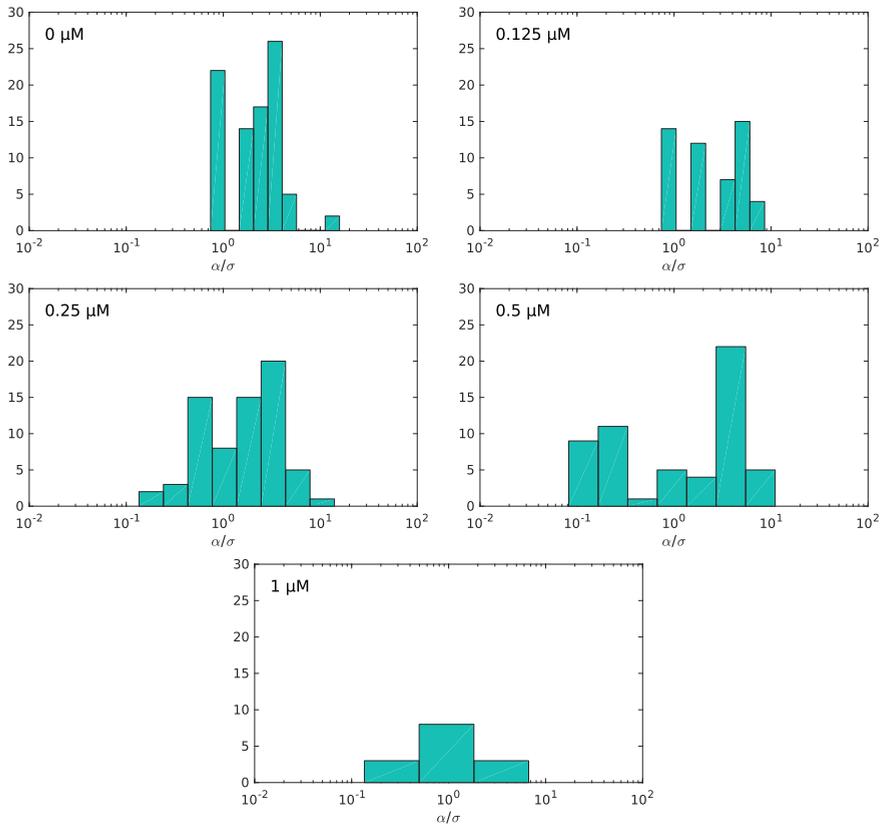
Figure 5.10: **Distributions of the ratio of directed contractilty α and isotropic contractilitie σ for five different concentrations of ROCK inhibitor** (0, 0.125, 0.25, 0.5 and 1 µM), as calculated using equations (5.6) and (5.7).

5.3 Discussion & Conclusion

In a preceding study it has been shown that extracellular-matrix recognition by either integrin $\alpha_5\beta_1$ or integrin $\alpha_v\beta_3$ does lead to differential cellular response [11]. Whereas $\alpha_5\beta_1$ expressing cells were characterized by extended intracellular actin structures, which potentially led to a more polar cellular contractility, $\alpha_v\beta_3$ expressing cells were characterized by shorter actin bundles and isotropic cellular contractility. Here, we confirmed in experiments that $\alpha_5\beta_1$ expressing cells could mimic $\alpha_v\beta_3$-phenotype by specific down-regulation of the actin-myosin system using a Rho-kinase inhibitor.

We presented data on the effect of the ROCK Rho-kinase inhibitor Y27632 on the cytoskeletal organization and the cellular contractility in GEβ1 cells. To modulate the actin-myosin network we utilized an inhibitor which specifically down-regulates the function of myosin, but also shortens actin stress fibers. Hence, the drug transforms, in a reversible manner, the cell phenotype from the $\alpha_5\beta_1$ expressing cells to $\alpha_v\beta_3$ expressing cells. To our surprise, we found that even a major inhibition by the drug the isotropic contractility, characterized by σ was unchanged. The effect of the Rho-kinase inhibitor mainly resulted in a loss of the polar contractility α. Our finding that the isotropic contractility was unchanged, reconciles results in which the directionality of cellular forces has been analyzed [11]. Our interpretation of both observations relies on the effects that the Rho-kinase inhibitor has on the organization of the actin cytoskeleton. The inhibitor not only decreases the function of myosin but also shortens stress fibers. Shorter stress-fibers, though being able to generate a comparable contractility, will form an isotropic medium mainly characterized by σ. Only long stress fibers will be able to organize cellular contractility on a spatial scale that can lead to the development of cellular polarity.

In conclusion, here we showed how the organization of intracellular actin structures is a prerequisite for cellular force polarity and how, by pharmacological interference with the actin organization, the cellular phenotype can be changed. It is interesting to follow, how insights gained by our study could be utilized in a search for novel approaches in Rho-kinase targeting for cancer therapy.

5.4 Materials & Methods

Cell culture and fluorescent labelling

Epithelioid GE11 cells [14] expressing αvβ1 (GEβ1) have been cultured as described before [11]. Cells have cultured in medium (DMEM; Dulbecco's Modified Eagle's Medium, Invitrogen/Fisher Scientific) supplemented with 10% fetal bovine serum (HyClone, Etten-Leur, The Netherlands), 25 U/ml penicillin and 25 U/ml µg/ml streptomycin (Invitrogen/Fisher Scientific cat. # 15070-063). The medium was exchanged for medium containing 0, 0.125, 0.25, 0.5 or 1 µM Y27632 ROCK inhibitor (Tocris cat. number 1254, Bristol, UK), and subsequently incubated for an hour. Cells were fixed in 4% formaldehyde and then permeabilised with 0.1% Triton-X and 0.5% BSA in PBS. Tetramethylrhodamine (TRITC)-Phalloidin (Fisher Emergo B.V. cat. # A12380, Thermo Fisher) was subsequently used to stain F-actin [11].

Micropillar arrays

Micropillar arrays were made out of a soft elastomeric material (PDMS) using a negative silicon wafer as a mask as described before [17, 18]. Briefly, the 2 µm diameter micropillars are arranged in a hexagonal pattern with a 4 µm centre-to-centre distance. The micropillars have a height of 6.9 µm, resulting in a stiffness of 16.2 nN/µm. The pillar tops were fluorescently labeled using an Alexa 405-fibronectin conjugate (Alexa Fluor®, Invitrogen/Fisher Scientific, Breda, The Netherlands; Fibronectin cat. #1141, Sigma Aldrich, Zwijndrecht, The Netherlands). Pillar deflections were determined with ∼30 nm precision using a specifically designed Matlab script resulting in a ∼0.5 nN precision in force [18].

Imaging

High-resolution imaging was performed on an in-house constructed spinning disk confocal microscope based on an Axiovert200 microscope body with a Zeiss Plan-Apochromat 100× 1.4NA objective (Zeiss, Sliedrecht, The Netherlands) and a CSU-X1 spinning disk unit (CSU-X1, Yokogawa, Amersfoort, The Netherlands). Imaging was done using an emCCD camera (iXon 897, Andor, Belfast, UK). Alexa405 and TRITC were exited using 405 nm (Crystalaser, Reno, NV) and 561 nm (Cobolt, Stockholm, Sweden) lasers, respectively.

Image analysis

All image analysis and ellipse fitting are performed using Matlab$^{\circledR}$, except the determination of the stress fiber orientation for which ImageJ with the OrientationJ plugin (`http://bigwww.epfl.ch/demo/orientation/`) was used. The micropillar array allows measuring forces that the cell exerts on the substrate. The forces used in calculations were selected manually when sufficiently large and close to the cell edge. The cell edge is found using a custom script that filters background using a lowpass filter and selects the cell based on a threshold. Then the contour of the cell is divided into parts at the locations of the selected forces. Segments whose straight end-to-end distance is less than 50 pixels (6.9 μm) are discarded, the rest of the segments is used for fitting ellipses.

The orientation of cell edge segments as used in figure 4.1c was calculated by measuring the angle of a line through the two adhesions at either end of the segment. We then defined θ as the angle between this line and the stress fibers.

Ellipse fitting

Ellipses are defined in our experiments with five parameters each: the coordinates of the center of the ellipse, the lengths of the short and long axes, and the angle that the long axis of the ellipse makes with the x-axis of the coordinate system of the image. We use fixed lengths for long and short axes for the N ellipses in the same cell. The optimal ellipse size per cell and positions for each ellipse are found using a $2(N + 1)$ parameter fit which minimises the distance between fitted ellipses and cell edge by calculating χ^2. Initial parameters for this fit are obtained from fitting each ellipse separately and averaging the lengths of the axes of the ellipses. Ellipses whose χ^2 is greater than 10 are discarded, which occurs in case of membrane ruffling and other out-of-equilibrium events.

In the global fit, the orientations of the ellipses are fixed to the local orientations of stress fibers. Orientations are measured from the channel with TRITC-Phalloidin (Actin) using the OrientationJ plugin for ImageJ. The average orientation per cell edge segment is calculated over all pixels between 15 and 50 pixels (2.07 μm and 6.9 μm) away from the cell edge whose coherency is greater than 0.15.

Force analysis

For both the circle and ellipse models, forces on the intersections of circles or ellipses are calculated. For circles, these forces are the vector sum of two forces whose direction is on the tangent to the circle and whose relative magnitude is the radius of the circle. For the ellipse case, the position of the single force on the intersection of two ellipses is first mapped to two forces on a single ellipse. While doing this the short and long axes of the ellipse are rotated and translated such that they coincide with the x and y-axes of the coordinate system. Then two forces $\boldsymbol{F}_1$ and $\boldsymbol{F}_0$ are calculated by combining equation (4.3) and equation (4.4), and defined in such a way that they are pointing clockwise and counter-clockwise around the ellipse:

$$
\begin{aligned}
\frac{\boldsymbol{F}_0}{\lambda_-} &= (\beta \sin\phi + \zeta\cos\phi)\,\hat{\boldsymbol{x}} + \left(-\frac{\beta}{\gamma}\cos\phi + \zeta\sin\phi\right)\hat{\boldsymbol{y}} \\
\frac{\boldsymbol{F}_1}{\lambda_-} &= (\beta \sin\phi - \zeta\cos\phi)\,\hat{\boldsymbol{x}} + \left(-\frac{\beta}{\gamma}\cos\phi - \zeta\sin\phi\right)\hat{\boldsymbol{y}} \\
\beta &= \frac{d}{2a} \\
\zeta &= \sqrt{\frac{1 + \tan^2\phi}{1 + \gamma\tan^2\phi} - \frac{\beta^2}{\gamma}}\;.
\end{aligned}
\tag{5.9}
$$

Here d is the distance between the positions of both forces on the ellipse, a is the length of the long axis of the ellipse and ϕ is the angle that the line through both points makes with the x-axis. After this $\boldsymbol{F}_0$ and $\boldsymbol{F}_1$ are rotated back to the coordinate system of the image and summed to give the force, scaled by λ_-, acting on the cell edge on the location of a particular intersection of two ellipses.

The magnitude of the traction forces is required for the calculation of the minimal line tension λ_- and the isotropic and directed stresses σ and α. We get this from the micropillar array. A measured force usually is the sum of two forces exerted by two different cell edge segments. Therefore, we first decompose the traction force into two forces pointing along tangents to the two cell edge segments adjacent to the position of the force. Then, per cell, we take

any combination of two clockwise and counter-clockwise forces and calculate:

$$\lambda_- = \sqrt{\frac{F_{1x}^2 F_{0y}^2 - F_{0x}^2 F_{1y}^2}{F_{0y}^2 - F_{1y}^2}}$$

$$\sigma = \frac{|\boldsymbol{F}_0 - \boldsymbol{F}_1|}{d} \frac{F_{0x} + F_{1x}}{F_{0y} - F_{1y}} \tag{5.10}$$

$$\alpha = \sigma \left(\frac{1}{\gamma} - 1 \right) .$$

Here $\boldsymbol{F}_0$ and $\boldsymbol{F}_1$ are defined in the coordinate system where the x and y-axes are the short and long axes of the ellipse. Furthermore, F_{nx} and F_{ny} are the components of $\boldsymbol{F}_n$ in the x and y-directions respectively. To calculate values for these quantities, we average all the different tensions and stresses we get for all possible combinations in all cells, taking the errors on these values into account as weights while averaging.

References

[1] M. J. Paszek et al. "Tensional homeostasis and the malignant phenotype". In: *Cancer Cell* 8.3 (2005), pp. 241–254. DOI: 10.1016/j.ccr.2005.08.010.

[2] D. E. Discher, P. Janmey, and Y. L. L. Wang. "Tissue cells feel and respond to the stiffness of their substrate". In: *Science* 310.5751 (2005), pp. 1139–1143. DOI: 10.1126/science.1116995.

[3] E. Zamir and B. Geiger. "Molecular complexity and dynamics of cell-matrix adhesions". In: *J. Cell Sci.* 114.20 (2001), pp. 3583–3590.

[4] R. Zaidel-Bar et al. "Hierarchical assembly of cell–matrix adhesion complexes". In: *Biochem. Soc. Trans.* 32.3 (2004), pp. 416–420. DOI: 10.1042/bst0320416.

[5] B. Geiger, J. P. Spatz, and A. D. Bershadsky. "Environmental sensing through focal adhesions". In: *Nat. Rev. Mol. Cell Biol.* 10.1 (2009), pp. 21–33. DOI: 10.1038/nrm2593.

[6] T. Iskratsch, H. Wolfenson, and M. P. Sheetz. "Appreciating force and shape — the rise of mechanotransduction in cell biology". In: *Nat. Rev. Mol. Cell Biol.* 15.12 (2014), pp. 825–833. DOI: 10.1038/nrm3903.

[7]   B. E. Vogel et al. "A novel integrin specificity exemplified by binding of the alpha v beta 5 integrin to the basic domain of the HIV Tat protein and vitronectin". In: *J. Cell Biol.* 121.2 (1993), pp. 461–468. DOI: `10.1083/jcb.121.2.461`.

[8]   R. O. Hynes. "Targeted mutations in cell adhesion genes: what have we learned from them?" In: *Dev. Biol.* 180.2 (1996), pp. 402–412. DOI: `10.1006/dbio.1996.0314`.

[9]   A. P. Mould, J. A. Askari, and M. J. Humphries. "Molecular basis of ligand recognition by integrin $\alpha5\beta1$. I. Specificity of ligand binding is determined by amino acid sequences in the second and third NH2-terminal repeats of the α subunit". In: *J. Biol. Chem.* 275.27 (2000), pp. 20324–20336. DOI: `10.1074/jbc.M000572200`.

[10]   K. A. Jansen et al. "A guide to mechanobiology: Where biology and physics meet". In: *Biochim. Biophys. Acta - Mol. Cell Res.* 1853.11 (2015), pp. 3043–3052. DOI: `10.1016/j.bbamcr.2015.05.007`.

[11]   H. E. Balcioglu et al. "The integrin expression profile modulates orientation and dynamics of force transmission at cell-matrix adhesions". In: *J. Cell Sci.* 128.7 (2015), pp. 1316–1326. DOI: `10.1242/jcs.156950`.

[12]   J. D. Hood and D. A. Cheresh. "Role of integrins in cell invasion and migration". In: *Nat. Rev. Cancer* 2.2 (2002), pp. 91–100. DOI: `10.1038/nrc727`.

[13]   E. H. J. Danen. "Integrins: regulators of tissue function and cancer progression". In: *Curr. Pharm. Des.* 11.7 (2005), pp. 881–891. DOI: `10.2174/1381612053381756`.

[14]   E. H. J. Danen et al. "The fibronectin-binding integrins $\alpha5\beta1$ and $\alpha v\beta3$ differentially modulate RhoA–GTP loading, organization of cell matrix adhesions, and fibronectin fibrillogenesis". In: *J. Cell Biol.* 159.6 (2002), pp. 1071–1086. DOI: `10.1083/jcb.200205014`.

[15]   E. H. J. Danen et al. "Integrins control motile strategy through a Rho-cofilin pathway". In: *J. Cell Biol.* 169.3 (2005), pp. 515–526. DOI: `10.1083/jcb.200412081`.

[16]   J. D. Mih et al. "Matrix stiffness reverses the effect of actomyosin tension on cell proliferation". In: *J. Cell Sci.* 125.24 (2012), pp. 5974–5983. DOI: `10.1242/jcs.108886`.

[17]   L. Trichet et al. "Evidence of a large-scale mechanosensing mechanism for cellular adaptation to substrate stiffness". In: *Proc. Natl. Acad. Sci. U. S. A.* 109.18 (2012), pp. 6933–6938. DOI: `10.1073/pnas.1117810109`.

[18] H. Van Hoorn et al. "The nanoscale architecture of force-bearing focal adhesions". In: *Nano Lett.* 14.8 (2014), pp. 4257–4262. DOI: 10.1021/nl5008773.

Summary

Schrödingers book 'What is life', which he wrote in 1944, is often considered to be the start of the field of biological physics. Yet the term and the research field of biophysics existed already before, probably starting with the experiments of Luigi Galvani on the electrical stimulation of frog-muscle already in 1780. Physics and biology were established research fields with extensive history at that time. It is the confluence of those two fields, that has lead to unforeseen discoveries in the last century, such as the identification of DNA as the origin of heredity (discussed in Schrödingers book), the map of the human genome in the 1990's, our current knowledge of the structure of a large part of the proteome, and our emergent understanding of cellular control and self-organization by chemical and physical cues. Many of those successes were tied to technical developments in microscopy, one of the main tools of biophysicists. Advances in microscopy were awarded three Nobel prizes. The scanning electron microscope developed by Ernst Ruska was awarded the Nobel prize in physics in 1986, the 2014 Nobel prize in chemistry was awarded to biophysicists for the development of optical super-resolved fluorescence microscopy. And recently, in 2017, the Nobel prize in chemistry was awarded to biophysicists that dramatically pushed the capabilities of the electron-microscope for determination of life protein structures.

The work described in this thesis makes heavy use of high-resolution, ultrasensitive fluorescent microscopy, mostly for observation of dead or living samples. Yet in chapter 3 the microscope is also used for the locally controlled initiation of a biology-inspired process itself. Similarly, in chapter 2, the microscope is used in building the structure needed for the experiment at hand. In chapters 4 and 5, at which three-dimensional objects are investigated, a special form of microscopy called confocal microscopy is used to form extra clear images.

The field of biological physics studies biological phenomena at a vast range of length-scales. From the individual water molecule that permeates through a lipid membrane, to processes that occur on read-out of the genetic information from DNA, to mechanical squeezing of a cell through narrow pores in tissue, to flight navigation of a fly in a very agile manner, to even the effect of the global environment on organisms and populations. Overarching in all those studies from the smallest molecule to the biggest organism is that shape plays an immense role in defining the function. In this thesis, I touch upon the topic of shape and function in biology, selecting a few exciting examples around cellular scale and below.

In **chapter 2** I explored the influence of shape and morphology on the function of dendritic spines. Dendritic spines are important structures of the brain involved in memory and learning. On the dendritic spine, one neuron connects to another. The connection is called the 'synapse', forming the contact to transfer signals between the two. The axon terminal of the neuron on the sending side is opposite to the dendritic spine, usually a mushroom-shaped protrusion, of the other neuron on the receiving end. The signal is transmitted by the release of small molecules, the neurotransmitters, by the axon terminal. These neurotransmitters are sensed by specialized receptors on the membrane of the dendritic spine. The number of receptors on the dendritic spine thereby determines the strength of the signal.

The experiment described in chapter 2 involves mimicking the dendritic spine. The artificial dendritic spine I constructed consists of a giant unilamellar vesicle, from which I pulled a few-hundred-nanometer-thin membrane tube. In this way, the mushroom shape is mimicked. The role of receptors in my mimetic system is played by quantum dots attached to lipids in the membrane. The quant-dot labeled lipids were able to move freely within the membrane. Using this system I was able to underline the influence of the shape of the dendritic spine on the retainment of receptors in the dendritic spine.

In **chapter 3** I investigated a system on a smaller scale, where I show the influence of local differences in mechanics in the membrane of a cell. The plasma membrane defines a cell by separating the inside of a cell from the outside. Other membranes are used inside the cell to form compartments with different functions. The largest of which, in eukaryotic cells, is the nucleus. Just like any material, lipids, of which membranes are made, can be in different states of matter. For most substances, those are the solid, fluid and gaseous phases. Lipid membranes exhibit a richer phase-space. There is a gel phase in which lipids are locked in place, like in a solid. There are two liquid phases, commonly labeled 'liquid-ordered' and 'liquid-disordered' in which lipids are free to move

within the membrane, yet the tail-regions are oriented in a preferred direction. The temperature at which lipids will undergo a phase-change depends on the lipid type. Hence, at a given temperature different lipids have preferences for different phases. Because of that they can separate and form homogeneous areas, much like the separation of oil from water.

This process called phase separation, I induced in giant unilamellar vesicles, using light. During this process the membrane changes significantly, more surface area becomes available and, as a result, the membrane tension drops. In this way, the shape of a membrane is affected on a small scale. It has been suggested that such separation of lipid phases influences the binding of proteins and leads to structural organization of the cell membrane.

I changed gears a bit in **chapter 4**. In this chapter, I looked at the shape of cells as a whole. The shape of a cell is largely determined by its cytoskeleton. I used a confocal microscope to image actin, a major component of the cytoskeleton. Actin, together with bundles of motor proteins in muscle cells, is the basis of the contractility of the muscle. In general, actin is ubiquitous to any cells and is a major structural component. I looked at the organization of actin inside the cell and correlated its organization with the shape of the cell.

Cells on a flat substrate usually attach at discrete points along the edge of the cell. In between these points, the edge of a cell is smooth and curved in a characteristic way. It turns out that the particular shape of these edges tells about the anisotropy of the cytoskeleton inside the cell. The anisotropy in the cell is due to aligned actin stress fibers, long strands of bundled actin spanning the whole cell. I discovered that the edge of a cell follows an elliptical curve, which is characteristic for each cell. I developed a model that predicted that all ellipses fitted to a single cell have the same size and aspect ratio. Moreover, the long axis of these ellipses pointed in the direction in which the stress fibers were pointing.

I continued this story in **chapter 5**. In this chapter, I actively influenced the shape of cells by adding a drug (ROCK-inhibitor). The protein ROCK normally promotes the activity of myosin motors, which leads to the contraction of actin fibers. Further, it promotes the formation of long strands of actin, resulting in so-called stress fibers. The ROCK-inhibitor blocks this activity, hence makes the stress fibers shorter and less contractile. As a result, the actin cytoskeleton became isotropic. I discovered, as predicted by the model developed in chapter 4, that the shape of the cell edges assumed a circular shape after addition of the drug.

In summary, this thesis applied physical principles to biology, by considering the influence of the shape of structures on biological systems. Ideas have been applied at the cellular level and below. By developing physical models, I was able to quantify important parameters of the systems I was looking at. This enabled me to qualitatively assert that cell shape is an important parameter for the biological function.

Samenvatting

Schrödingers boek 'What is life', geschreven in 1944 wordt vaak gezien als de start van het veld biofysica. Echter, de term en het onderzoeksveld bestonden al lang voor dat, de experimenten van Luigi Galvani, die al in 1780 kikkerspieren elektrisch stimuleerde waren waarschijnlijk het begin. Natuurkunde en biologie waren toen al gevestigde velden met een lange geschiedenis. Het is de samenvloeiing van deze twee velden wat geleid heeft tot onverwachte ontdekkingen in de afgelopen eeuw, zoals de identificatie van DNA als de oorzaak van erfelijkheid (besproken in Schrödingers boek), de kaart van het menselijk genoom in de 1990's, onze huidige kennis van de structuur van een groot deel van het proteoom en ons opkomende begrip van cellulaire controle en zelf-organisatie door chemische en fysische aanwijzingen. Veel van deze successen waren verbonden met technische ontwikkelingen in microscopie, een van de voornaamste gereedschappen van de biofysica. De vooruitgang in de microscopie werd beloond met drie Nobelprijzen. De scanning elektron microscoop, ontwikkeld door Ernst Ruska, werd beloond met de Nobel prijs in natuurkunde in 1986, de Nobelprijs voor scheikunde in 2014 ging naar biofysici voor de ontwikkeling van optische super-opgeloste fluorescentie microscopie. En recent, in 2017, werd de Nobelprijs in scheikunde gegeven aan biofysici die de mogelijkheden van de elektron microscoop voor de vaststelling van eiwitstructuren dramatisch verbeterd hebben.

Het werk beschreven in dit proefschrift maakt veel gebruik van hoge-resolutie ultra-gevoelige fluorescentie microscopie, meestal voor de observatie van dood of levend materiaal. Bovendien, in hoofdstuk 3 wordt de microscoop ook gebruikt voor lokaal gecontroleerde initiatie van een door biologie geïnspireerd proces. Evenzo, in hoofdstuk 2 wordt de microscoop gebruikt voor het maken van benodigde structuur voor het experiment. In hoofdstukken 4 en 5, waar driedimensionale objecten worden onderzocht, is een speciale vorm van microscopie, confocale microscopie genaamd, gebruikt om extra duidelijke beelden te maken.

Het veld van biologische natuurkunde bestudeert biologische fenomenen over een groot bereik van lengte-schalen. Van het individuele watermolecuul dat door een lipide membraan dringt, processen die gebeuren bij het uitlezen van genetische informatie van DNA, het mechanische persen van cellen door nauwe poriën in een weefsel, lenige vluchtnavigatie van vliegen, tot zelfs aan het effect van het globale milieu op organismes en populaties. Overkoepelend over al deze studies van het kleinste molecuul tot aan het grootste organisme is de rol van vorm, die altijd een immense rol speelt in het bepalen van functie. In dit proefschrift raak ik dit onderwerp, over vorm en functie in biologie, aan door een paar opwindende voorbeelden rondom cellulaire schaal en kleiner.

In **hoofdstuk 2** verken ik de invloed van vorm en morfologie op die functie van dendritische spines. Dendritische spines zijn belangrijke structuren in het brein die betrokken zijn bij geheugen en leren. Op de dendritische spine verbindt een neuron zich aan een ander. Deze verbinding heet 'synaps', en vormt het contact om signalen tussen de twee neuronen te versturen. Het presynaptische eindknopje van de neuron aan de verzendende kant staat tegenover de dendritische spine, dat meestal een paddenstoelvormig uitsteeksel is aan de ontvangende kant van het volgende neuron. Het signaal wordt doorgegeven door het afstaan van kleine moleculen, neurotransmitters, door het eindknopje. Deze neurotransmitters worden waargenomen door receptoren op het membraan van de dendritische spine. Daardoor bepaalt het aantal receptoren op de dendritische spine de sterkte van het signaal.

Het experiment beschreven in hoofdstuk 2 bootst de dendritische spine na. De kunstmatige dendritische spine die ik geconstrueerd heb, bestaat uit een reusachtig unilamellair vesikel, waaruit ik een paar-honderd-nanometer-dun membraan buisje getrokken heb. Op deze manier wordt de paddenstoelvorm nagebootst. De rol van receptoren in mijn kunstmatig systeem wordt gespeeld door kwantum dots die zijn vastgemaakt aan lipiden in het membraan. Met dit systeem was ik in staat om de invloed van de vorm van de dendritische spine op het behoud van receptoren in de dendritische spine te onderstrepen.

In **hoofdstuk 3** onderzoek ik een systeem met een kleinere schaal. Ik laat de invloed van lokale verschillen in de mechanica in het membraan van een cel zien. Het plasmamembraan definieert een cel door binnen- en buitenkant uit elkaar te houden. Andere membranen worden in de cel gebruikt om verschillende compartimenten met verschillende functies te vormen. De grootste daarvan is in eukariotische cellen de celkern. Net zoals elke stof, kunnen lipiden, waarvan membranen gemaakt zijn, bestaan in verschillende toestanden. Voor de meeste substanties zijn dit de vaste, vloeibare en gasvormige toestanden. Lipiden laten een rijkere faseruimte zien. Er is een gelfase waarin lipiden vast zitten op hun plek, zoals in een vaste stof. Er zijn twee vloeibare toestanden, meestal

gelabeld als 'vloeibaar-geordend' en 'vloeibaar-ongeordend', waarin lipiden vrij kunnen bewegen in het membraan, tegelijk zijn al de staartdelen van de lipiden georiënteerd in een voorkeursrichting. De temperatuur waarbij lipiden een toestandsverandering ondergaan hangt af van het type lipide. Daardoor hebben op een gegeven temperatuur verschillende lipiden voorkeuren voor verschillende toestanden. Daarom kunnen ze van elkaar scheiden en homogene gebieden vormen, ongeveer zo als de scheiding van olie en water.

Dit proces, fasescheiding genoemd, zette ik in beweging in reusachtige unilamellaire vesikels door licht te gebruiken. Gedurende dit proces verandert het membraan significant, er komt meer oppervlak beschikbaar, en als resultaat vermindert de membraanspanning. Op deze manier wordt de vorm van het membraan beïnvloed op een kleine schaal. Er is voorgesteld dat zo een scheiding van lipide toestanden de binding van eiwitten beïnvloedt en leidt tot structurele organisatie van het celmembraan.

In **hoofdstuk 4** veranderde ik mijn aanpak een beetje. In dit hoofdstuk bekeek ik de vorm van cellen als geheel. De vorm van een cel wordt grotendeels bepaald door het cytoskelet. Ik maakte gebruik van een confocale microscoop om beelden te maken van actine, een belangrijk component van het cytoskelet. Actine staat samen met bundels motoreiwitten aan de basis van samentrekking van spieren. In het algemeen bevindt actine zich in alle cellen en is het een belangrijk structureel component. Ik heb gekeken naar de organisatie van actine in de cel en heb de organisatie gecorreleerd met de vorm van de cel.

Cellen hechten zich normaal gesproken via afzonderlijke punten aan een plat substraat. Tussen deze punten is de rand van de cel glad en op een karakteristieke manier gekromd. Het blijkt dat de bijzondere vorm van deze randen ons over de anisotropie van het cytoskelet in de cel vertelt. De anisotropie in de cel komt door lange uitgelijnde bundels van actine, gespannen door de hele cel. Ik ontdekte dat de rand van de cel een elliptische kromme volgt die karakteristiek is voor iedere cel. Ik ontwikkelde een model dat voorspelde dat alle ellipsen die aan een enkele cel passen allemaal dezelfde grootte en excentriciteit hebben. Bovendien wijzen de lange assen van de ellipsen in de richting in welke de actine bundels wijzen.

Ik vervolgde dit verhaal in **hoofdstuk 5**. In dit hoofdstuk beïnvloed ik de vorm van cellen actief door een stof toe te voegen (ROCK-remmer). Het eiwit ROCK promoot normaal gesproken de activiteit van myosine motoren, die zorgt van een samentrekking van actine bundels. Verder promoot het de formatie van lange bundels van actine, die ik genoemd heb in de vorige alinea.

De ROCK-remmer blokkeert deze activiteit en maakt daardoor deze bundels korter en minder samentrekkend. Als resultaat wordt het actine cytoskelet meer isotroop. Ik ontdekte, als voorspeld door het in hoofdstuk 4 ontwikkelde model, dat de vorm van de celranden een circulaire vorm aannam na toevoeging van de stof.

Samengevat, dit proefschrift past natuurkundige principes toe op biologie door het overwegen van de invloed van de vorm van structuren op biologische systemen. Ideeën zijn toegepast of cellulair en kleiner niveau. Door natuurkundige modellen te ontwikkelen was ik in staat belangrijke parameters van de systemen waarnaar ik gekeken heb te kwantificeren. Dit stelde me in staat om kwalitatief te beweren dat de vorm van een cel is een belangrijke parameter in biologische functie.

Publications

[1]   M. de Wild, **W. Pomp** and G. H. G. Koenderink. "Thermal memory in self-assembled collagen fibril networks". In: *Biophys. J.* 105.1 (2013), pp. 200-210. DOI: `10.1016/j.bpj.2013.05.035`

[2]   E. Beletkaia, S. F. Fenz, **W. Pomp**, B. E. Snaar-Jagalska, P. W. Hogendoorn and T. Schmidt. "CXCR4 signaling is controlled by immobilization at the plasma membrane". In: *Biochim. Biophys. Acta - Mol. Cell Res.* 1863.4 (2016), pp. 607-616. DOI: `10.1016/j.bbamcr.2015.12.020`

[3]   S. H. C. Askes, **W. Pomp**, S. L. Hopkins, A. Kros, S. Wu, T. Schmidt and S. Bonnet. "Imaging upconverting polymerosomes in cancer cells: Biocompatible antioxidants brighten triplet-triplet annihilation upconversion". In: *Small* 12.40 (2016), pp. 5579-5590. DOI: `10.1002/smll.201601708`

[4]   S. H. C. Askes, V. C. Leeuwenburgh, **W. Pomp**, H. Armandi-Tash, S. Tanase, T. Schmidt and S. Bonnet. "Water-dispersable silica-coated upconverting liposomes: Can a thin silica layer protect TTA-UC against oxygen quencing?". In: *ACS Biomater. Sci. Eng.* 3.3 (2017), pp. 322-334. DOI: `10.1021/acsbiomaterials.6b00678`

[5]   **W. Pomp**, K. K. Schakenraad, H. E. Balcıoğlu, H. Van Hoorn, E. H. J. Danen, R. M. H. Merks, T. Schmidt and L. Giomi. "Cytoskeletal anisotropy controls geometry and forces of adherent cells". In: *ArXiv.org* (2017), pp. 1-10. arXiv: `1702.03916`

[6] **W. Pomp**, M. Rinaldin and T. Schmidt. "Inducing phase-separation in GUV's by light". *In preparation.*

[7] **W. Pomp**, R. P. T. Kusters, C. C. Storm and T. Schmidt. "The narrow-escape problem revisited experimentally in an artificial system". *In preparation.*

[8] **W. Pomp**, K. K. Schakenraad, H. E. Balcıoğlu, H. Van Hoorn, E. H. J. Danen, R. M. H. Merks, L. Giomi and T. Schmidt. "Reconstruction of an $\alpha_v \beta_3$ phenotype in $\alpha_5 \beta_1$ expressing cells on Rho-kinase down regulation". *In preparation.*

Curriculum Vitae

Wim Pomp was born in Rotterdam, The Netherlands on the 7th of March 1988. He studied Physics from 2010 to 2013 at Leiden University. During the bachelor, he endeavored to advance the study of chromatin by building a novel total internal reflection (TIRF) microscope combining magnetic tweezers and fluorescence resonance energy transfer (FRET) with alternating laser excitation in John van Noort's group. Later, during the MSc. program, he worked in Gijsje Koenderink's group at the AMOLF Institute in Amsterdam, where he investigated the polymerization of collagen networks. This work resulted in his first paper. The end of his MSc. program brought him to Thomas Schmidt's group. Here, he worked for the first time on the shape of cells, and on how to look at actin dynamics using an array of micropillars.

After finishing the MSc. program, he continued as a PhD-student in Thomas Schmidt's group in the new FOM program *Barriers in the Brain*. Within the scope of this program, he worked on resolving the dynamics of one of the smallest structures in the brain: the dendritic spine. Additionally, he continued work started during his MSc. studies by studying the relation between forces in the cytoskeleton and the shape of cells. Besides this fundamental research, he was involved in maintaining and enhancing the capabilities of the advanced microscopes in Thomas Schmidt's laboratory.

During his Ph.D., he visited numerous national and international conferences, winter, summer and spring schools and meetings. During the Nanofront Winterschool of 2015, he won an award for the best collaboration proposal involving the advent of artificial life, resulting in a collaboration between Thomas Schmidt and Christophe Danelon from TU Delft. Wim furthermore collaborated with Dimitriou Stamou and Kadla Rosholm (University of Copenhagen), Kees Storm and Remy Kusters (TU Eindhoven), Luca Giomi, Roeland Merks and Koen Schakenraad (Leiden University), Erik Danen and Emrah Balcıoğlu (Leiden University), Sjaak Neefjes and Daphne van Elsland (Leiden University

Medical Center). He assisted in courses in Labview and Classical Mechanics and supervised Melissa Rinaldin who was an MSc student in Thomas Schmidt's group. In October 2017, Wim started a postdoctoral appointment in Tomas Kirchhausen's group at the Boston Children's Hospital and Harvard Medical School in Boston.

Acknowledgements

The four years one spends on the work to obtain a Ph.D. are regarded as so important in one's life, that when the Ph.D. is granted, the right is given to the graduate to extend his or her name with a title. However, the work needed to get a Ph.D. cannot be done alone. My life in the group of 'Physics of Life Processes' (FvL) was full of interactions with colleagues, supervisor, assisting staff and other people. I was so fortunate to know FvL already before I started my Ph.D., and expectations have not been disappointed. Always is there someone to extend a helping hand with work, but also outside work interactions were warm and plentiful. I will always remember my time in FvL as a wonderful time.

I would like to thank a great number of people in particular. There are so many people to thank, the chance that I might forget someone is substantial.

Thomas Schmidt; I would like to thank you, first for giving me a chance to do interesting science and secondly for guiding me through the process of obtaining my Ph.D. Sylvie Olthuis; thank you for the assistance in the laboratory, and many thanks for reminding me when lunchtime was approaching. Yvonne Kerkhof, thank you for your help with anything that requires dealing with things at the university which are not science. Raymond Koehler, Peter van Veldhuizen, you and other people from the electronics and fine mechanical departments were a great help during my work, thank you.

My colleagues from FvL, I had a great time with you. Hedde and Ruth, thank you for hauling me into this wonderful group. Rolf, you and I share a number of interests, it was great to work with you on our microscopes. I'm sure we will have quite some discussions on this topic in the future. Olga, Veer and Stefano, you were amazing office mates, thank you for the not-always-work-related interactions. Artur and Hendrik (Meng), thank you for willing to